Bernhard Müller, MSc.

Application of Luminescent Sensors – A Journey from Miniaturization to Imaging

Dissertation

Zur Erlangung des akademischen Grades

Doktor der technischen Wissenschaften

eingereicht an der

Technischen Universität Graz

Betreuer:

Assoc.Prof. Dipl.-Chem. Dr.rer.nat. Torsten Mayr

Institut für Analytische Chemie und Lebensmittelchemie

Graz, April, 2020

“It's not a silly question if you can't answer it.”

Jostein Gaarder

Statutory Declaration

I declare that I have authored this thesis independently, that I have not used other than the declared sources / resources, and that I have explicitly marked all material which has been quoted either literally or by content from the used sources.

Date

Signature

Acknowlegment

As always when projects come to an end and new challenges await on the horizon, it is worthwhile to sit back, take a deep breath and recap on the path which led to that moment.

First of all, I want to thank my supervisor Torsten Mayr. I am very greatfull for his support, the fruitful on- and off-topic discussions, as well as for the freedom he granted to develop my own scientific ideas. Moreover, I want to thank Torsten for enabling the financial support of my thesis.

In general, I want to thank the whole ACFC institute for their support. Especially Helmar Wiltsche and Lukas Troi, who helped a lot with their electronic engineering knowledge and craftsmanship. Moreover, special thanks to Eveline Maier, who is capable of organizing almost impossible things, and Anna Walcher for keeping the Labs running.

And of course, a big “THANK YOU” to all current and departed members of the sensors group. Thank you, for the fun work environment with destressing coffee breaks, sometimes disturbing lunch conversations and occasionally surprisingly productive after-work beers. It is an awesome situation to be able to call your colleges at work also your friends. I am very grateful to be part of this group!

At this point, I also want to thank everyone who contributed to the work which has been conducted for this thesis. Thanks to all the bachelor, project lab and master students I worked with. Moreover, I want to thank all my cooperation partners at TU Wien and TU Graz. Special thanks are due to Cyrill Grengg and Florian Mittermayr. Their uplifting spirits were inspiring, allowed for good laughs and provided the necessary stamina to start a new project.

Moreover, I want to thank all my study colleges (“08er-Jahrgang”), without whom I would not have reached the end of this path. And of course, thank you to all my friends who provided moral support and distraction in form of mountaineering adventures or other recreations.

At the end I want to thank my family for always being there for me. Eva, for her open ears and for reminding me, what is really important in life. My parents, for supporting me all these years (not only financially!) and for providing me with the possibility to chase my own goals. I am infinitely grateful! Ella, thank you for everything. For your support, your understanding, your love. I am looking forward to our future as a family!

Abstract

In this thesis different fields of applications for optical pH and oxygen sensors, based on their unmatched flexibility regarding possible sensor formats, are explored. Therefore, luminescent indicator dyes embedded in a suitable polymeric matrix are used.

In the first project, miniaturized pH and oxygen sensor spots were integrated in a microfluidic chip, allowing the measurement of respiration and acidification rates of mammalian cells. Microfluidic technology is an emerging research field, enabling the growth of organoid cell clusters (2D and 3D cell models) in polymer chips. These advanced organ-on-chip models severely lack sensor technology capable of on-line and in-line monitoring to assess the condition of the cells due to the confined space. This problem can be solved with optical sensors, since they are quite easy to miniaturize and can be read-out from the outside of the chip. One of the biggest challenges is the actual sensor integration into the chip. We developed a new sensor integration method based on microdispensing. With this technology, sensor spots as small as 500µm can be produced and precisely positioned on even structured surfaces. The utilized sensor material is based on a phosphorescent platinum benzophorphyrin dye for oxygen measurements and a fluorescent aza-BODIPY dye for pH measurements. Both indicators are excited with red light, which is less disruptive for cells than light with shorter wavelength, and emit in the NIR region, where there is no autofluorescence from biological material. For the pH sensor spots an inert phosphorescent reference compound (Egyptian Blue) with similar spectral properties is used to enable dual lifetime referencing. Both sensor spots can be read-out with a miniaturized phasefluorimeter utilizing the luminescence decay time as a measurement parameter. This led to the stable sensor signals needed for the acquisition of the flat slopes from which the corresponding rates were calculated.

In the second projected the feature of luminescent sensors to allow imaging was utilized. Degradation processes in concrete materials usually corelate with a decrease in pH and progress non-linearly due to their heterogenic structure. Therefore, an imaging method is needed for a precise assessment regarding the degree of corrosion. This is crucial for state-of-repair analysis and the development of sustainable concrete-based building materials. The introduction of fluorescent pH indicator dyes with a high apparent pKa value, enabled luminescent imaging as a viable method for this field of application. The combination of pH sensitive aza-BODIPY dyes with inert phosphorescent reference compounds yielded in a decay time-based measurement scheme. With the utilization of a fast-gate-able camera, time domain- dual lifetime referenced measurements were conducted. This stable referencing system eliminated most artifacts of the heterogenic background and a high spatial resolution of up to 35 µm per pixel was achieved. Therefore, this pH imaging method embodies a new valuable analytical tool for the whole concrete-based industry.

Kurzfassung

Der Inhalt dieser Doktorarbeit befasst sich mit den verschiedenen Einsatzmöglichkeiten von optischen pH- und Sauerstoffsensoren, welche sich durch die Flexibilität der ihnen zur Verfügung stehenden Sensorformate ergeben. Dabei kommen lumineszierende Indikatorfarbstoffe zum Einsatz, die in einer geeignete Polymerematrix immobilisiert sind.

Das erste Projekt beschäftigt sich mit der Integration von miniaturisierten pH- und Sauerstoffsensorspots in mikrofluidische Systeme um die Respiration- und Ansäuerungsraten von Säugetierzellkulturen zu messen. Mikrofluidische Zellkulturtechniken sind ein aufstrebender Forschungszweig, der es ermöglicht organartige Zellstrukturen (2D und 3D Zellmodelle) zu züchten. Für diese fortschrittlichen Organ-im-Chip Modelle stehen jedoch aufgrund ihrer geringen Größe nur selten geeignete Messmethoden für die Online- und Inline-Überwachung des Zellzustands zur Verfügung. Optische Sensoren bieten hierbei eine gute Möglichkeit dieses Problem zu lösen, da sie sehr einfach miniaturisiert und von Außerhalb des Chips ausgelesen werden können. Die vielleicht größte Herausforderung dabei ist die eigentliche Integration der Sensorspots in die mikrofluidischen Strukturen. Im Zuge dieser Arbeit wurde eine neue Methode zur Sensorintegration, basierend auf der Verwendung eines Mikro-Dispensers, entwickelt. Mit dieser Technologie können Sensorspots bis zu einer minimalen Größe von 500 µm hergestellt und präzise in mikrofluidische Strukturen eingebracht werden. Das für Sauerstoffsensoren verwendete Sensormaterial basiert auf phosphoreszierenden Platinum Benzophorphyrin Farbstoffen, das für pH Sensoren verwendete Material auf fluoreszierenden aza-BODIPY Farbstoffen. Beide Indikatorfarbstoffe können mit rotem Licht angeregt werden, was zu weniger Störungen im Zellwachstum führt, und emittieren im NIR Bereich indem keine Eigenfluoreszenz von biologischem Material stattfindet. Zusätzliche kommt in den pH Sensoren ein inerter, phosphoreszierender Referenzfarbstoffe (Ägyptisch Blau) mit ähnlichen spektralen Eigenschaften zum Einsatz um eine lebenszeitbasierende Referenzierung zu ermöglichen. Dadurch kann für beide Sensorspots die mittels Phasenfluorimetrie ausgelesene Lumineszenzabklingzeit als Messparameter herangezogen werden. Diese Methode führt zu stabilen Sensorsignalen, die für die Aufzeichnung der flachen Signalkurven aus denen die Raten berechnet werden nötig sind.

Im zweiten Projekt wurde die Fähigkeit optischer Sensoren zum Lumineszenz-Imaging genutzt. Korrosionsprozesse in Beton gehen üblicherweise mit einer Absenkung des pH-Wertes einher und schreiten aufgrund heterogener Strukturen nicht linear voran. Daher ist für die genaue Beurteilung des Korrosionsverlaufes ein bildgebendes Verfahren nötig. Dieses ist für aussagekräftige Erhebung des baulichen Zustands von Infrastrukturobjekten und die Entwicklung nachhaltiger Baumaterialien unerlässlich. Die Entwicklung von fluoreszierenden pH Indikatoren mit hohen pKs Werten ermöglichte es, dass Lumineszenz-Imaging auch in diesem Anwendungsfeld eine wertvolle Methode darstellt. In Kombination mit inerten, phosphoreszierenden Referenzfarbstoffen konnte eine Abklingzeit basierte Methodik entwickelt werden. Dabei kommt ein Kamerasystem mit der

Möglichkeit zur präzisen Aufzeichnung von Zeitfenstern zum Einsatz, welches eine Lebenszeitbasierte Referenzierung ermöglicht. Das stabile Referenzierungssystem eliminiert die meisten durch den heterogenen Hintergrund verursachten Artefakte und es kann damit eine hohe räumliche Auflösung von bis zu 35 µm pro Pixel erreicht werden. Dieses bildgebende pH Messverfahren stellt damit eine neue, wertvolle analytische Methode für die gesamte Betonindustrie dar.

Content

Part I

Introduction

1. Scope and Outline of the Thesis

Luminescent sensors are amongst the most versatile analytical instruments with regards to possible applications due to their flexible sensor formats. They can be easily miniaturized and externally read-out, which makes them powerful tools for microfluidic applications. Moreover, the constant progress made in the field of organ-on-chip systems demands new analytical methods for gathering information from inside these small and complex devices. Up to this date, mainly dissolved oxygen measurements were conducted with optical sensors in these systems. Therefore, miniaturized pH sensor spots were developed and integrated together with oxygen sensor spots into a microfluidic cell assay, which allowed to observe the metabolic activity of the cells via the measurement of their respiration and acidification rate.

Luminescent sensors can also be used for imaging purposes, leading to an unmatched spacial resolution. Since the pH value is the main parameter for the assessment of chemical concrete deterioration, the introduction of fluorescent pH indicators with a high apparent pKa, made the development of an imaging method for concrete analytics possible. The challenges of an inhomogeneous matrix can be met by superior referencing techniques like time-domain dual lifetime referencing. This method can be used by incorporation of an inert reference compound with similar spectral properties and utilization of a gate-able camera system.

This thesis is written in cumulative manner and the presented manuscripts are submitted or already accepted in peer reviewed journals. Each manuscript is accompanied by a preface, describing the framework of the project from which the publication resulted.

Chapter 2 introduces the necessary theoretical background for understanding the basic concept behind luminescent sensors and describes possible measurement parameters and referencing techniques. Further, a short introduction into the basics of microfluidic systems and concrete deterioration analysis is given.

Chapter 3 presents the development of miniaturized oxygen and pH sensor spots for the measurement of respiration and acidification rates of mammalian cells in a microfluidic system. Therefore, microdispensing was investigated as a method for integration of small sensor spots in microfluidic chambers. The microfluidic chips made from thermoplastic COC, were produced via a novel fast prototyping approach. Finally, the suitability of the presented stop/flow measurement method to assess metabolic parameters of mammalian cells was shown.

Chapter 4 describes the work that has been conducted to show the possibility to perform pH imagine on concrete surfaces with fluorescent indicator dyes. The utilized dyes exhibit a high apparent pKa value and are combined with a phosphorescent and inert reference dye. This allowed for the application of dual lifetime referencing in the time-domain as a measurement scheme for which a

fast gate-able camera system was used. The recorded pH distributions had a good spatial resolution and clearly visualized the progress of chemical concrete corrosion such as carbonation.

Chapter 5 contains the improvements which were made for the pH imaging method described in chapter 4. The system was reconfigured for the use of an alternative reference compound which better matches the spectral properties of the indicator dye, while providing a better optical insulation at the same time. Further, optodes were made which combined two similar pH indicators with different apparent pKa values, effectively widening the sensitive range to 3 pH units. Via the installation of a macro lens the resolution was improved to 35 µm per pixel and the suitability of the measurement method for different kinds of concrete material was investigated.

2. Theoretical Background

2.1. Chemical Sensors

According to IUPAC, a chemical sensor is a *"device that transforms chemical information, ranging from the concentration of a specific sample component to total composition analysis, into an analytically useful signal. The chemical information, mentioned above, may originate from a chemical reaction of the analyte or from a physical property of the system investigated."*[1] The commonly used Cambridge definition further clarifies that sensors are *"miniaturized devices that can deliver real time and on-line information on the presence of specific compounds or ions in even complex samples."*[2] Following these definitions a sensor typically consists of a receptor unit and a transducer unit. The receptor is the part of a sensor which responds to the presence of the analyte of interest or interacts with it, thereby converting the chemical information in a physical form of energy (e.g. light). The transducer on the other hand, transforms this physical quantity into a useful analytical signal. Due to a sensors ability for continuous monitoring of various analytes, there has been an increasing interest in academic research and a growing demand for industrial application.[3]

The main criteria of an ideal sensor can be summarized as following:

- Conversion of a chemical information (e.g. analyte concentration) into an analytical useful signal (e.g. electrical signal)
- Selective response towards the analyte of interest
- Sensitivity rage of the sensor matches the analyte level in the sample
- Reversible interaction of the receptor with the analyte
- Response time is in the same time frame as concentration changes happen
- Stability during measurements and long shelf life

Secondary criteria like the ease-of-use, their cost and the potential for miniaturization are further important parameter determining if a sensor is broadly applied.

Due to the above-mentioned properties of sensors, they have some major benefits when compared to classical analytical chemistry. Usually there is no manual sample collection, transport and preparation needed since sensors are developed as on-line or in- line measurement systems for the continuers monitoring over a longer period of time. They can be directly deployed on-site and due to a high degree in automation measurements are generally less labor intense. Nowadays a huge variety of different sensor concepts utilizing different mechanisms exist. This thesis will focus on luminescent sensors which the emission of light to pass on the chemical information.

2.2. Luminescent Chemical Sensors

A very powerful sensor concept is based on the utilization of luminescent dyes as recognition element. Upon interaction with a specific analyte their optical properties change, which can be detected as an optical signal. A luminescent sensors set-up typically consists of a light source (e.g. LED), a sensing material (often referred to as luminescent sensor) and a detector (e.g. photodiode), which collects and quantifies the received signal. Further optical elements like filters and light guides can be placed between these three main elements to provide specific light properties (e.g. wavelength selection or light focus point).[4,5]

The main component of the sensing material is the luminescent indicator dye. It interacts with the analyte of interest and thereby changes its optical properties. It is typically embedded in a suitable polymeric matrix shielding the dye form adverse influences, providing a stable environment. Depending on the measurement set-up, an additional inert reference component can additionally be immobilized in the matrix.

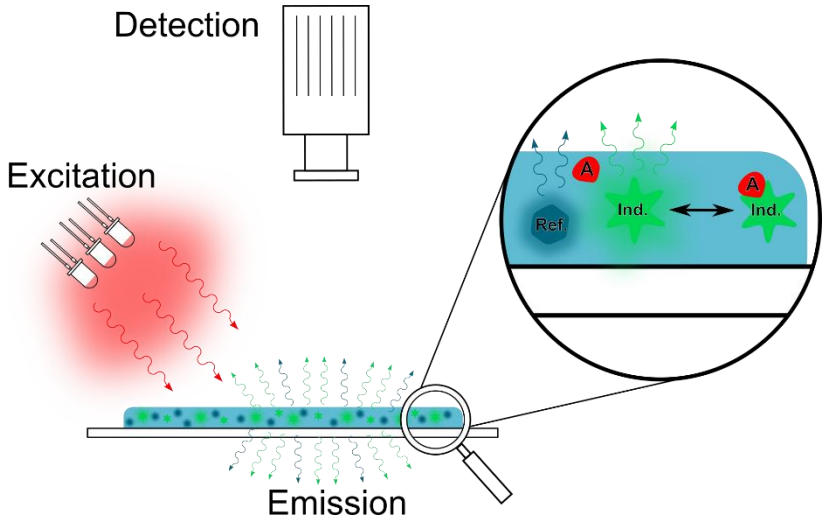

Figure 1: Basic scheme of a luminescent chemical sensor consisting of an analyte (A) sensitive indicator dye (Ind.) and an inert reference compound (Ref.). The luminescent sensor is excited with an appropriate light source and emits light depending on the analyte concentration. This light is captured with a detector and analyzed.

Luminescent sensors have several benefits, which make them attractive for industrial; biological or medical applications. The most evident one is, that they are not influenced by electrical or magnetic interferences. Moreover, they don't show a stirring speed dependency and the analyte of interest is usually not consumed by the sensors, since no chemical reaction occurs. The utilization of light to transport information results also in the possibility to separate the sensing material from the read-out unit and therefore the sensor does not need to be directly connected to the detector device. This physical separation enables to run luminescent sensors in otherwise challenging measurement set-ups like sterile environments or confined spaces. It also allows the production of quite cheap single-use measurement systems, where only the sensing material discharged. A further huge benefit is the possibility to deploy the sensor material in different sensor formats. Next to classical sensor spots, which can be cut in all sizes and shapes, the sensor material can be coated on micro tips, be

cast into nanoparticles or even be fabricated as big sensor foils for imaging purposes to cover the entire range from nano to macro scale. Last, but not least, the materials used for optical sensor are commonly non-poisonous and therefore their use is considered non-invasive. Especially when red light is used as an excitation source biological samples can be investigated without destroying or even harming it.

2.2.1. Fundamentals of Luminescence

Luminescence is the emission of photons from an electronically exited species and can be classified depending on the source of the energy for this activation. The work within this thesis mainly focuses on photoluminescence, where the energy originates from the absorption of a photon by said species. Generally speaking, luminescence describes radiative deactivation pathways which occur next to other, non-radiative, processes. In the Perrin-Jablonski diagram (Figure 2) these transition processes between different energy levels of a molecule are visualized. As mentioned above, photoluminescence can occur, when an electron is excited into a higher electronic energy level by absorption of a photon by a molecule. The energy added with this process to the electronic ground state $S_{0,}$ corresponds to the energy of the photon and respectively the wavelength of the absorbed light. After absorption the excited electron occupies a certain vibrational level in an excited singlet electronic state (S1, S2, …). From there various deactivation processes can happen at different rates, depending on the characteristic time for a certain transition (Table 1). Thereby the fastest process, after the absorption, is vibrational relaxation, where the energy is converted to thermal energy. This is the reason why other processes usually occur starting from the lowest vibrational level of a certain electronic state. The radiative deactivation process from the S_1 level to the ground state (S_0) is called fluorescence and relieves a photon with the according energy. The lifetime of this excited state S1 is in the same range as the time it takes for intersystem crossing (ISC) and internal conversion (IC) to happen. Both deexcitation processes compete therefore with fluorescence. Internal conversion describes the transition process between two electronic states with the same spin multiplicity (e.g. $S_0 \rightarrow S_1$), whereas intersystem crossing describes the transition between to electronic states with different multiplicity (e.g. $S_1 \rightarrow T_1$). This transition to the triplet state allows further de-excitation pathways like phosphorescence, the second possible radiative process. The transition between state with different multiplicity is generally forbidden and is made only possible due to spin-orbit coupling. This is the reason why the lifetime of the excited state T_1 is usually way longer than that of S_1. Consequently, phosphorescence lifetimes are longer than fluorescence lifetimes although the actual emission of a photon takes the same time than its absorption (~10^{-15} s). Phosphorescence is usually also hypsochromically shifted (to longer wavelength) compared to the absorption due to the lower energy level of T_1. However, in some cases it is still possible to observe a long fluorescent lifetime due to delayed fluorescence. This delayed emission from the S1 state can happen due to a transition back from T_1 to S_1, called reversed intersystem crossing (rISC).

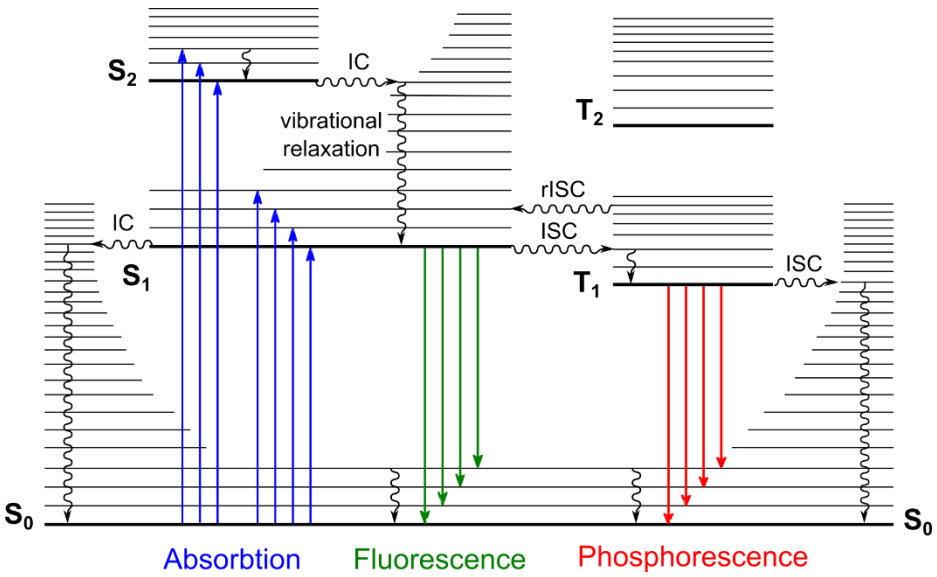

Figure 2: Perrin-Jablonski diagram for the visualization of radiative transition processes. S0 is the ground state in the thermodynamically equilibrium (singlet state), S1, S2,... are the excited singlet states and T1, T2,... represent the excited triplet states. Vibrational relaxation, internal conversion (IC), intersystem crossing (ISC) and reversed intersystem crossing (rISC) are competing non-radiative transitions.

Table 1: Characteristic times of luminescent processes.

process	time
absorption	10^{-15} s
vibrational relaxation	10^{-13} - 10^{-10} s
lifetime of excited state S_1	10^{-10} - 10^{-7} s → fluorescence
inter system crossing (ISC)	10^{-10} - 10^{-8} s
Internal conversion (IC)	10^{-11} - 10^{-9} s
lifetime of excited state T_1	10^{-6} - 1 s → phosphorescence

To characterize luminescence, with regards to sensor technology, on mayor parameter is the luminescence brightness. This term describes the ability of a molecule to convert excitation light into emission and thus combines a molecules ability to absorb light (molar absorption coefficient) with the likelihood for a radiative deactivation pathway (quantum yield). Another important parameter is the luminescence lifetime. It is defined as the time, in which 63% of the excited electrons from a certain excited state emit light to fall back to the ground state. Since energy of the emitted light is always lower than that of the absorbed due to vibrational relaxation, it is always shifted to a longer wavelength. This difference in the maxima of the absorption and the emission spectra is called Stockes shift. If one characteristic luminescence properties of a molecule changes upon interaction with a substance, this can be used for the development of an optical sensor since it generates a measurable signal.[6,7]

2.2.2. Platforms

As mentioned before, one major benefit of optical sensors is their flexibility when it comes to sensor design. Usually sensors are produced by bringing a sensor formulation, consisting of dissolved polymer and the sensor dye, in a certain shape. In the simplest case this can be via knife coating or spin coating into a uniform layer. From such a foil sensor tips can be fabricated or the whole foil can be used for imaging purposes. It is also possible to create patterned structures via inkjet printing, aerosol-jet printing or microdispensing where the sensor formulation is used as ink. Depending on the technique, structures as small as 100 µm can be reached. Another possibility is, to coat a thin layer of sensor film onto the tip of an optical fiber. With this technique probes with a tip size down to 50 µm can be produced. Moreover, the sensor formulation can also be precipitated into nanoparticles. These have the benefit of being easy to deploy and can also be used in closed systems like microfluidic chips or uneven surfaces. However, these particles are normally used as sensor probes, since a recovery is not possible and they cannot be reused.

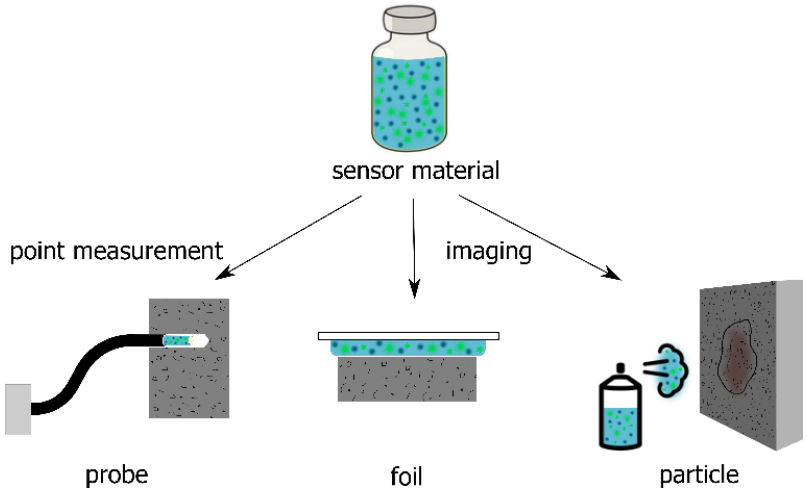

Figure 3: Illustration of possible sensor designs to visualize the flexibility of luminescent chemical sensors.

2.2.3. Measurement principles for luminescent chemical sensors

Generally speaking, there are three different luminescence parameter which are commonly utilized for optical sensors. There is (a) the overall intensity, (b) the wavelength λ and (c) the luminescence decay time τ. These parameters can be exploited by different measurement schemes and be even combined to allow advanced referencing.[8]

2.2.3.1. Intensity-based measurements

The simplest way to measure a sensor response is by detecting its luminescence intensity. This method is widely used for different analytes like pH, CO_2, oxygen or ionic species.[9–12] The analyte of interest causes a change in the intensity, which in turn correlates to a change in concentration.[13–15] The necessary instrumentation is quite simple and low cost compared to

other measurement schemes. It requires only a constant light source, an optical filter system to separate excitation and emission light and a detector (e.g. photoelectrode).

However, this method is also the most susceptible one, since the results are influenced by background light, unstable light sources (varying intensity and wavelength), absorption, refection and scattering effects of the sample and varying photodetector sensitivity, to name a few. Further factors, like the positioning of the components, inhomogeneous light fields and uneven sensor dye distribution, can be compensated via careful calibration, but still have to be kept in mind.

2.2.3.2. Ratiometric wavelength-based measurements

Wavelength ratiometric measurements can overcome some of the previous mentioned problems, by measuring the luminescence intensity of a sensor at least at two different emission wavelengths. Thereby the intensity of one of the wavelength bands has to be independent from the analyte concentration. Alternatively, two different excitation wavelengths can be utilized to achieve the same result of an intrinsic referencing. This is for example utilized for pH measurements, where the indicator is excited at the isospestic point (pH independent) additionally to one of the absorption maxima.[16,17] However, most of the time the easier approach is to introduce an inert reference compound with a similar excitation spectrum.[18,19] In this case it is crucial that the two dyes are located in close proximity to one another in order to experience the same light conditions. Moreover, the ratio between the two dyes has to be constant in order for this referencing technique to work.

This technique utilizes continuous excitation and therefore can be done with the same basic and simple instrumentation than the intensity-based measurement. It has to be only extended with additional optical filters to enable measurements or excitation at two different wavelengths. Another elegant possibility for imaging applications is to utilize the three channels of an RGB camera. In these cameras blue, green and red light is recorded separately at the same time. By carefully selecting the spectral properties of the indicator and the reference dye they can be collected independently from each other one in separate channels (e.g. the indicator in the green channel and the reference in the red channel). However the two separate intensity measurements are performed, by dividing the analyte dependent signal by the analyte independent signal inhomogeneous light fields and indicator distributions can be referenced out. In any case, this method does not compensate interferences caused by ambient light, intrinsic luminescence by the sample. Also, absorption, refraction or scattering effects are not referenced out since they are wavelength depended.

2.2.3.3. Luminescence lifetime-based measurements

Luminescence lifetime is the most attractive parameter to measure, since it overcomes several of the drawbacks of intensity-based measurements. It is a very robust parameter, which is independent from the overall intensity. This means that fluctuations in the opto-electronic system,

scattering, reflections, coloration, turbidity, inhomogeneous indicator distribution in the sensing layer, deviations in the placement of the sensor foil and low levels of ambient light do not affect the accuracy of the measurement.[20,21] However, the instrumentational afford is significantly higher due to the requirements on fast gate-able detectors and precisely timed emission sources. There are two methods to employ the luminescence lifetime as a measurement parameter. It can either be detected in the time-domain, where a pulsed excitation source is used, or in the frequency domain utilizing a sinusoidal modulated light source.[22–26] Figure 4 shows a schematic representation of the two different approaches. In any case, the delay in the luminescence of the sensor from the excitation source reflects the decay time.

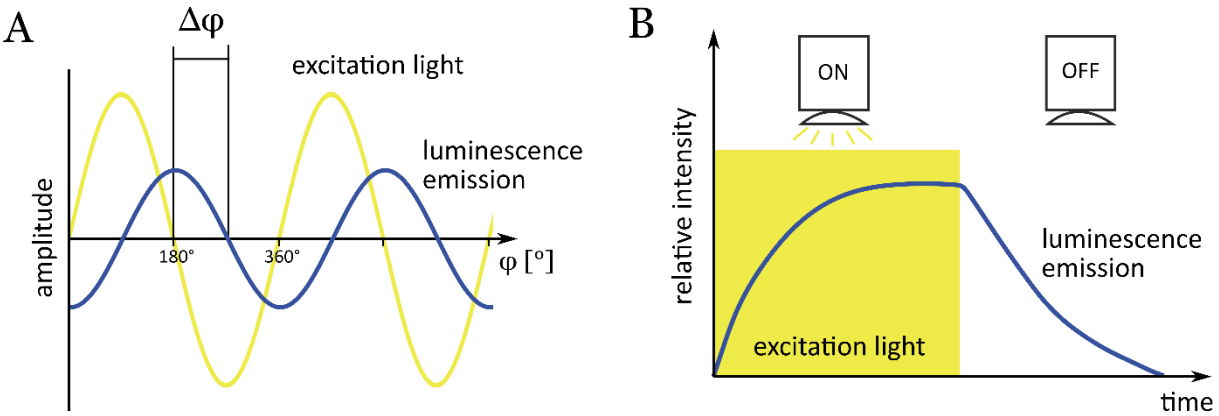

Figure 4: Schematic representation of the two different approaches for luminescence lifetime-based measurements. **A)** Frequency-domain approach. The indicator is excited with a sinusoidal modulation. The sensor response (luminescence emission) follows the excitation frequency with a decay time dependent delay resulting in $\Delta\phi$as measured parameter. **B)** Time-domain approach. The indicator is excited with a square shaped light pulse. The luminescent emission intensity rises and falls with a decay time dependent slope. By integration of the intensity over certain time gates the decay time can be measured.

For measurements performed in the time-domain there are two different methods to quantify the decay time-depended parameter (R), which is calibrated against the analyte concentration. In both methods the luminescence is measured in two defined time gates (Δt_i) after an excitation light pulse. Dividing these two intensities through each other gives rise to the intrinsically referenced ratio R. For rapid lifetime determination (RLD) both gates are localized after the end of the excitation light strictly measuring during the emission period. Phase delay rationing (PDR) on the other hand, sets one gate during the excitation period and only the second one in the emission period. Both schemes are depicted in figure 5. The major difference between the two methods is, that with PDR higher signal intensities due to longer time gates can be realized. Consequently, the signal-to-noise ratio is better. However, with RDL it is possible to get rid of short-lived background fluorescence from the sample without using optical filters when a phosphorescent indicator is used by setting the time gates appropriately. This generally leads to lower signal intensities and therefore to lower signal-to-noise ratios.

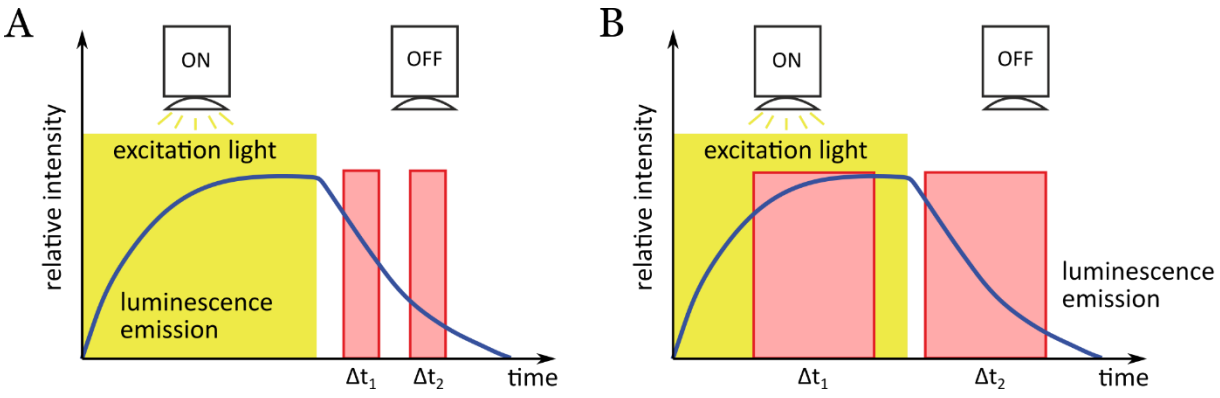

Figure 5: Illustration of the two different methods used for time-domain based measurement of the decay time dependent parameter R. **A)** Rapid Lifetime Determination (RLD) scheme. The intensities measured during the time gates Δt_1 and Δt_2 are recorded both within the emission period. **B)** Phase Delay Rationing (PDR) scheme. The first time gate for the measurement of the luminescence intensity is set during the excitation phase (Δt_1), while the second is recorded during the emission phase (Δt_2).

2.3. Methods utilized for pH measurements

Within the conducted work two different pH measurement methods have been used. Both of them utilize inert phosphorescent particles as a reference for fluorescent aza-BODIPY pH indicators to enable lifetime-based measurements although the lifetime of the indicator is analyte independent.[21] Measurements performed with a miniaturized phasefluorimeter use the frequency-domain based dual lifetime referencing (DLR) method. It is used for the read-out of miniaturized pH sensor spots integrated in microfluidic systems for the evaluation of metabolic parameters of mammal cell cultures (Chapter 3). For pH imaging of concrete surfaces (Chapter 4 and 5) a measurement method called time-domain dual lifetime referencing (t-DLR) was used to visualize different deterioration processes.

2.3.1. Frequency-domain Dual Lifetime Referencing (DLR)

Frequency-domain dual lifetime referencing is a well-established technique where the excitation source is sinusoidal modulated. Depending on the used frequency and the decay time of the luminescent signal, a shift in the phase angle ($\Delta\varphi$) is observed. When two luminophores with similar spectral properties are excited simultaneously, an overall luminescence signal is observed. It results from the superposition of the two single sine wave functions of the respective components. The phase angel of this signal is determined by the ratio of their luminescent intensities and decay times. The decay time of fluorescent indicators is magnitudes shorter than that of phosphorescent references, resulting in literally no phase shift when low modulation frequencies in the range of kHz are used. Therefore, the overall luminescent signal is only influenced by the intensity of the analyt sensitive fluorescent signal. However, due to this measurement scheme a change in analyte

concentration still results in a shift in the phase angle of the overall signal, therefor translating a analyte-dependent change in fluorescent intensity into lifetime-based measurement signal. In the case of pH sensitive aza-BODIPY dyes, the fluorescence is turned off under basic conditions and no actual change in fluorescent lifetime can be observed otherwise.[21]

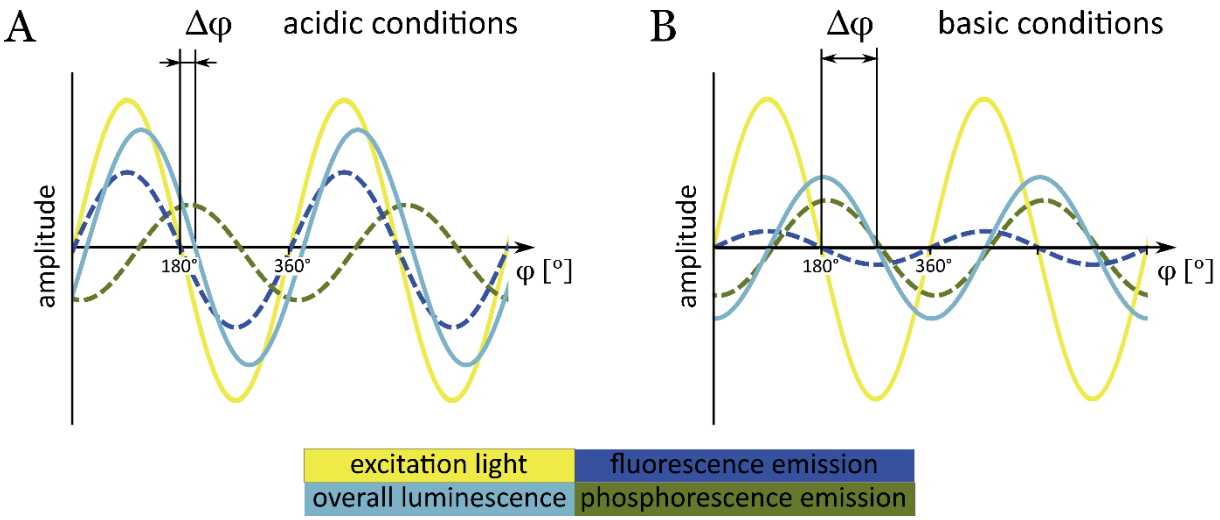

Figure 6: Illustration of DLR in the frequency-domain used for pH measurements conducted with miniaturized phasefluorimeters. The fluorescence of the pH indicator dye (short decay time) is collected together with the phosphorescence of an inert reference compound with similar spectral properties (long decay time). This leads to a pH dependent phase shift (Δφ) of the overall signal. **A)** Small phase shift under acidic conditions caused by a high contribution of the fluorescent indicator (bright state). **B)** Large phase shift under basic condition due to a small contribution of the florescent indicator (quenched state).

2.3.2. Time-domain Dual Lifetime Referencing (t-DLR)

The beneficial effect of adding a phosphorescent reference compound can also be utilized in a time-domain based measurement set-up. In this case both components are excited with a squared pulse of light. The overall luminescence intensity is captured during two time windows (Δt_1 & Δt_2) and subsequently result in the analyte dependent ratio R after division. The first luminescent intensity is measured during the light pulse where the fluorescence of the indicator and the phosphorescence of the reference contribute to the overall signal. Since the fluorescence intensity of the indicator changes with the analyte concentration, the overall luminescence signal from the first window does as well. The second measurement takes place shortly after the end of the light pulse. It only captures the emitted light of the reference compound, since the analyte dependent fluorescence signal is not captured due to its fast decay time. Therefore, the not analyte dependent second window can be used as a reference for the analyte dependent first window, hence transferring the intensity-based measurement into a time-resolved one. This method is preferred for imaging applications, since directly gateable cameras can be deployed.

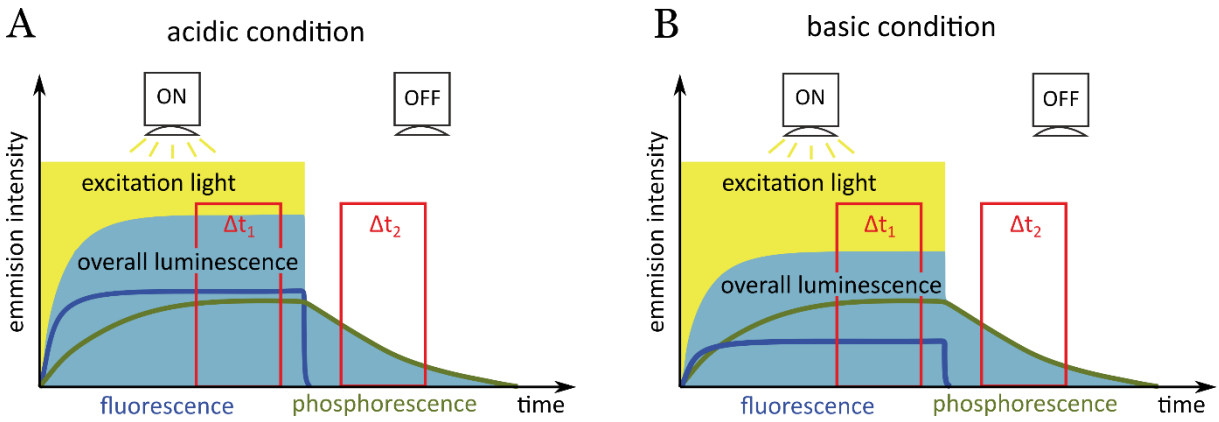

Figure 7: Illustration of DLR in the time-domain used for pH imaging of concrete samples affected by different degradation processes. The fluorescence of the pH indicator dye (short decay time) is collected together with the phosphorescence of an inert reference compound with similar spectral properties (long decay time). During the first time gate (Δt_1) both components contribute to the overall luminescence intensity, whereas during the second time gate (Δt_2) only the phosphorent reference dye emits light. The ratio R of the measured intensities represents the referenced sensor response. **A)** High R value under acidic conditions due to a high fluorescent contribution of the unquenched pH indicator. **B)** Low R value under basic conditions due to a small intensity contribution of partially quenched pH indicator.

2.4. Luminescent Chemical Sensors in Microfluidic Systems

Microfluidic systems are "*systems that process or manipulate small amounts of fluids (≤µL) using channels with dimensions in the micrometer range or below*".[27] This small feature size leads to several beneficial properties most notably the usage of very small sample volumes. Moreover, they make use of some interesting fluid physics like laminar flow and unusual phenomena occur due to huge surface-to-volume ratios as Squires and Quake explain.[28] The first microfluidic devices were design for analytical purposes with Manz et al.[29] proposing the firsts micro total analysis system (µTAS). These first lab-on-chip devices[30–32] have pathed the way for further applications of microfluidic devices in fields like microbiology[33,34], biomedical research[35] and 3D cell culturing[36] enabling organ-on-chip research. Nowadays the trend continues and whole body-on-chip systems are developed to model the interaction of multiple organs. The recent advances are summarized by Sung et al. in 2019.[37]

One of the main limitations of microfluidic systems is the difficulty to collect analytical information from these systems. Herein, luminescent chemical sensors are a powerful tool due to their easy miniaturization, the ability for external read-out and good biocompatibility].[38–43] However, integration of the sensors still remains a challenging task. The most common concepts are based around the use of sensor particles[44–47] or integration of sensor layers or spots.[42] The integration of sensor spots can be achieved via airbrush spraying[40] or ink-jet printing[48–51], whereas uniform layers for imaging purposes are mainly done via bald-, dip- or spin-coating.[42] At the moment, mainly oxygen[52,53], pH[54] and temperature[55] are monitored with

luminescent sensors. Thereby dissolved oxygen measurements are by far the most prominent due to the availability of reliable sensor material and its significance in biological processes (e.g. monitoring cell growth).

2.5. Visualization of pH development in concrete structures

Concrete is the most common construction material worldwide. The determination of its durability and state of repair is crucial and plays a huge economic role. The central parameter for the assessment of concrete structures is its pH level since a decrease in pH is characteristic for all major types of chemical concrete degradation such as carbonation and acid attacks. The initial pH of ordinary Portland cement-based concrete is usually around 13[56] and is mainly affected by the content of alkali materials, supplementary cementitious materials and curing conditions.[57,58] Destructive processes which are controlled by concrete environment interactions lower this initially high pH. Due to the inhomogeneous nature of concrete, theses degradation processes mostly proceed non-linearly [56] and are governed by mineralogical and structural heterogeneities controlling the diffusion processes of aggressive species.[59,60] In this context, an accurate assessment with high spatial resolution is crucial for the understanding of pH development over time. State-of-the art pH measurement methods which are available for hardened concrete have recently been summarized by Behnood et al.[61] However, imaging techniques which allow a spatial resolution of pH are rather limited and centered around absorption based indicator dyes like phenolphthalein, which are directly deployed on concrete surfaces and usually only show a transition point. In this regard, the introduction of luminescent imaging is a huge step forward, enabling precise measurements due to powerful referencing techniques. Luminescence imaging has already been used in various different fields for diverse analytes in the past. The applications range from O_2 imaging for technical applications[62] and environmental research[63] to pH[64] and potassium[65] imaging conducted in marine biology and microbiology. With the introduction of stable fluorescent pH indicators covering alkaline pH regimes[66], it is now also possible to take full advantage of luminescent pH imaging for the assessment and development of concrete-based materials.

2.6. References

[1] A. Hulanicki, S. Glab, F. Ingman, Chemical sensors: definitions and classification, Pure and Applied Chemistry. 63 (1991) 1247–1250. https://doi.org/10.1351/pac199163091247.

[2] K. Cammann, E. Guibault, H. Hall, R. Kellner, O. Wolfbeis, The Cambridge definition of chemical sensors, Proceedings of the Cambridge Workshop on Chemical Sensors and Biosensors. Cambridge University Press, New York. (1996).

[3] P. Gründler, Chemische Sensoren: Eine Einführung für Naturwissenschaftler und Ingenieure, Springer-Verlag, Berlin Heidelberg, 2004. https://doi.org/10.1007/3-540-35052-7.

[4] S.M. Borisov, O.S. Wolfbeis, Optical Biosensors, Chem. Rev. 108 (2008) 423–461. https://doi.org/10.1021/cr068105t.

[5] C. McDonagh, C.S. Burke, B.D. MacCraith, Optical Chemical Sensors, Chem. Rev. 108 (2008) 400–422. https://doi.org/10.1021/cr068102g.

[6] B. Valeur, M.N. Berberan-Santos, Molecular fluorescence: principles and applications, Second edition, Wiley-VCH ; Wiley-VCH Verlag GmbH & Co. KGaA, Weinheim, Germany : [Chichester, England], 2012.

[7] J.R. Lakowicz, ed., Principles of Fluorescence Spectroscopy, Springer US, 1983. https://doi.org/10.1007/978-1-4615-7658-7.

[8] G. Liebsch, Time-Resolved Luminescence Liftime Imaging with Optical Chemical Sensors, Dissertation, Universität Regensburg. (2000).

[9] M.E. Diaz-Garcia, R. Pereiro-García, N. Velasco-García, Optical oxygen sensing materials based on the room-temperature phosphorescence intensity quenching of immobilized Erythrosin B, Analyst. 120 (1995) 457–461. https://doi.org/10.1039/AN9952000457.

[10] B. Müller, P.C. Hauser, Fluorescence optical sensor for low concentrations of dissolved carbon dioxide, Analyst. 121 (1996) 339–343. https://doi.org/10.1039/AN9962100339.

[11] Y.L. Wang, J.M. Baten, S.P. Mcmaughan, D.R. Bobbitt, Optical Fiber-Based Sensor for Calcium Using Hydrophobically Associated Calcein and Laser-Induced Fluorescence Detection, Microchemical Journal. 50 (1994) 385–396. https://doi.org/10.1006/mchj.1994.1102.

[12] M.J.P. Leiner, P. Hartmann, Theory and practice in optical pH sensing, Sensors and Actuators B: Chemical. 11 (1993) 281–289. https://doi.org/10.1016/0925-4005(93)85266-D.

[13] Y. Amao, K. Asai, T. Miyashita, I. Okura, Novel optical oxygen sensing material: platinum porphyrin–styrene–pentafluorostyrene copolymer film, Anal. Commun. 36 (1999) 367–

369. https://doi.org/10.1039/A907024I.

[14] X. Wu, M.M. F. Choi, D. Xiao, A glucose biosensor with enzyme-entrapped sol–gel and an oxygen-sensitive optode membranePresented at the Fifth Asian Conference on Analytical Sciences, Xiamen University, Xiamen, China, 4–7 May 1999., Analyst. 125 (2000) 157–162. https://doi.org/10.1039/A904925H.

[15] T. Itoh, K. Yaegashi, T. Kosaka, T. Kinoshita, T. Morimoto, In vivo visualization of oxygen transport in microvascular network, American Journal of Physiology-Heart and Circulatory Physiology. 267 (1994) H2068–H2078. https://doi.org/10.1152/ajpheart.1994.267.5.H2068.

[16] M. Dellian, G. Helmlinger, F. Yuan, R.K. Jain, Fluorescence ratio imaging of interstitial pH in solid tumours: effect of glucose on spatial and temporal gradients., Br J Cancer. 74 (1996) 1206–1215.

[17] G.R. Martin, R.K. Jain, Fluorescence ratio imaging measurement of pH gradients: calibration and application in normal and tumor tissues, Microvasc. Res. 46 (1993) 216–230. https://doi.org/10.1006/mvre.1993.1048.

[18] J.W. Parker, Olga. Laksin, Clement. Yu, M.Ling. Lau, Suzanne. Klima, Russell. Fisher, Ian. Scott, B.W. Atwater, Fiber-optic sensors for pH and carbon dioxide using a self-referencing dye, Anal. Chem. 65 (1993) 2329–2334. https://doi.org/10.1021/ac00065a027.

[19] R.P. Haugland, Handbook of fluorescent probes and research chemicals, Molecular Probes, Eugene. 8 (1996). https://ci.nii.ac.jp/naid/10004050155/ (accessed February 27, 2020).

[20] M.E. Lippitsch, J. Pusterhofer, M.J.P. Leiner, O.S. Wolfbeis, Fibre-optic oxygen sensor with the fluorescence decay time as the information carrier, Analytica Chimica Acta. 205 (1988) 1–6. https://doi.org/10.1016/S0003-2670(00)82310-7.

[21] I. Klimant, C. Huber, G. Liebsch, G. Neurauter, A. Stangelmayer, O.S. Wolfbeis, Dual Lifetime Referencing (DLR) — a New Scheme for Converting Fluorescence Intensity into a Frequency-Domain or Time-Domain Information, in: B. Valeur, J.-C. Brochon (Eds.), New Trends in Fluorescence Spectroscopy: Applications to Chemical and Life Sciences, Springer, Berlin, Heidelberg, 2001: pp. 257–274. https://doi.org/10.1007/978-3-642-56853-4_13.

[22] G. Marriott, R.M. Clegg, D.J. Arndt-Jovin, T.M. Jovin, Time resolved imaging microscopy. Phosphorescence and delayed fluorescence imaging, Biophys. J. 60 (1991) 1374–1387. https://doi.org/10.1016/S0006-3495(91)82175-0.

[23] X.F. Wang, T. Uchida, D.M. Coleman, S. Minami, A Two-Dimensional Fluorescence Lifetime Imaging System Using a Gated Image Intensifier, Appl. Spectrosc., AS. 45 (1991) 360–366.

[24] C.G. Morgan, A.C. Mitchell, Fluorescence lifetime imaging: an emerging technique in fluorescence microscopy, Chromosome Res. 4 (1996) 261–263. https://doi.org/10.1007/BF02263674.

[25] K. König, S. Boehme, N. Leclerc, R. Ahuja, Time-gated autofluorescence microscopy of motile green microalga in an optical trap, Cell. Mol. Biol. (Noisy-Le-Grand). 44 (1998) 763–770.

[26] T.W.J. Gadella, A. van Hoek, A.J.W.G. Visser, Construction and characterization of a frequency domain fluorescence lifetime imaging microscope., Journal of Fluorescence. 7 (1997) 35–43.

[27] G.M. Whitesides, The origins and the future of microfluidics, Nature. 442 (2006) 368–373. https://doi.org/10.1038/nature05058.

[28] T.M. Squires, S.R. Quake, Microfluidics: Fluid physics at the nanoliter scale, Rev. Mod. Phys. 77 (2005) 977–1026. https://doi.org/10.1103/RevModPhys.77.977.

[29] A. Manz, N. Graber, H.M. Widmer, Miniaturized total chemical analysis systems: A novel concept for chemical sensing, Sensors and Actuators B: Chemical. 1 (1990) 244–248. https://doi.org/10.1016/0925-4005(90)80209-I.

[30] D.R. Reyes, D. Iossifidis, P.-A. Auroux, A. Manz, Micro Total Analysis Systems. 1. Introduction, Theory, and Technology, Anal. Chem. 74 (2002) 2623–2636. https://doi.org/10.1021/ac0202435.

[31] C.T. Culbertson, T.G. Mickleburgh, S.A. Stewart-James, K.A. Sellens, M. Pressnall, Micro total analysis systems: fundamental advances and biological applications, Anal. Chem. 86 (2014) 95–118. https://doi.org/10.1021/ac403688g.

[32] D.E.W. Patabadige, J. Sadeghi, M. Kalubowilage, S.H. Bossmann, A.H. Culbertson, H. Latifi, C.T. Culbertson, Integrating Optical Fiber Bridges in Microfluidic Devices to Create Multiple Excitation/Detection Points for Single Cell Analysis, Anal. Chem. 88 (2016) 9920–9925. https://doi.org/10.1021/acs.analchem.6b03133.

[33] M.T. Guo, A. Rotem, J.A. Heyman, D.A. Weitz, Droplet microfluidics for high-throughput biological assays, Lab Chip. 12 (2012) 2146–2155. https://doi.org/10.1039/c2lc21147e.

[34] T.S. Kaminski, O. Scheler, P. Garstecki, Droplet microfluidics for microbiology: techniques, applications and challenges, Lab Chip. 16 (2016) 2168–2187. https://doi.org/10.1039/C6LC00367B.

[35] E.K. Sackmann, A.L. Fulton, D.J. Beebe, The present and future role of microfluidics in biomedical research, Nature. 507 (2014) 181–189. https://doi.org/10.1038/nature13118.

[36] S.N. Bhatia, D.E. Ingber, Microfluidic organs-on-chips, Nat. Biotechnol. 32 (2014) 760–772. https://doi.org/10.1038/nbt.2989.

[37] J.H. Sung, Y.I. Wang, N. Narasimhan Sriram, M. Jackson, C. Long, J.J. Hickman, M.L. Shuler, Recent Advances in Body-on-a-Chip Systems, Anal. Chem. 91 (2019) 330–351. https://doi.org/10.1021/acs.analchem.8b05293.

[38] S.L. Maldonado, P. Panjan, S. Sun, D. Rasch, A.M. Sesay, T. Mayr, R. Krull, A fully online sensor-equipped, disposable multiphase microbioreactor as a screening platform for biotechnological applications, Biotechnology and Bioengineering. 116 (2019) 65–75. https://doi.org/10.1002/bit.26831.

[39] H. Zirath, M. Rothbauer, S. Spitz, B. Bachmann, C. Jordan, B. Müller, J. Ehgartner, E. Priglinger, S. Mühleder, H. Redl, W. Holnthoner, M. Harasek, T. Mayr, P. Ertl, Every Breath You Take: Non-invasive Real-Time Oxygen Biosensing in Two- and Three-Dimensional Microfluidic Cell Models, Front. Physiol. 9 (2018). https://doi.org/10.3389/fphys.2018.00815.

[40] J. Ehgartner, P. Sulzer, T. Burger, A. Kasjanow, D. Bouwes, U. Krühne, I. Klimant, T. Mayr, Online analysis of oxygen inside silicon-glass microreactors with integrated optical sensors, Sensors and Actuators B: Chemical. 228 (2016) 748–757. https://doi.org/10.1016/j.snb.2016.01.050.

[41] P. Gruber, M.P.C. Marques, N. Szita, T. Mayr, Integration and application of optical chemical sensors in microbioreactors, Lab Chip. 17 (2017) 2693–2712. https://doi.org/10.1039/C7LC00538E.

[42] S.A. Pfeiffer, S. Nagl, Microfluidic platforms employing integrated fluorescent or luminescent chemical sensors: a review of methods, scope and applications, Methods Appl. Fluoresc. 3 (2015) 034003. https://doi.org/10.1088/2050-6120/3/3/034003.

[43] S. Sun, B. Ungerböck, T. Mayr, Imaging of oxygen in microreactors and microfluidic systems, Methods Appl. Fluoresc. 3 (2015) 034002. https://doi.org/10.1088/2050-6120/3/3/034002.

[44] A. Funfak, J. Cao, O.S. Wolfbeis, K. Martin, J.M. Köhler, Monitoring cell cultivation in microfluidic segments by optical pH sensing with a micro flow-through fluorometer using dye-doped polymer particles, Microchim Acta. 164 (2009) 279–286. https://doi.org/10.1007/s00604-008-0096-0.

[45] B. Ungerböck, A. Pohar, T. Mayr, I. Plazl, Online oxygen measurements inside a microreactor with modeling of transport phenomena, Microfluidics and Nanofluidics. 14 (2013) 565–574. https://doi.org/10.1007/s10404-012-1074-8.

[46] L. Mahler, M. Tovar, T. Weber, S. Brandes, M.M. Rudolph, J. Ehgartner, T. Mayr, M.T. Figge, M. Roth, E. Zang, Enhanced and homogeneous oxygen availability during incubation of microfluidic droplets, RSC Adv. 5 (2015) 101871–101878. https://doi.org/10.1039/C5RA20118G.

[47] J. Cao, S. Nagl, E. Kothe, J.M. Köhler, Oxygen sensor nanoparticles for monitoring bacterial growth and characterization of dose–response functions in microfluidic screenings, Microchim Acta. 182 (2015) 385–394. https://doi.org/10.1007/s00604-014-1341-3.

[48] A.R. Thete, G.A. Gross, T. Henkel, J.M. Koehler, Microfluidic arrangement with an integrated micro-spot array for the characterization of pH and solvent polarity, Chemical Engineering Journal. 135 (2008) S327–S332. https://doi.org/10.1016/j.cej.2007.07.012.

[49] A.R. Thete, G.A. Gross, J.M. Koehler, Differentiation of liquid analytes in gel films by permeability-modulated double-layer chemo-chips, Analyst. 134 (2009) 394–400. https://doi.org/10.1039/B808257J.

[50] C. Herzog, E. Beckert, S. Nagl, Rapid Isoelectric Point Determination in a Miniaturized Preparative Separation Using Jet-Dispensed Optical pH Sensors and Micro Free-Flow Electrophoresis, Analytical Chemistry. 86 (2014) 9533–9539. https://doi.org/10.1021/ac501783r.

[51] E. Poehler, C. Herzog, M. Suendermann, S.A. Pfeiffer, S. Nagl, Development of microscopic time-domain dual lifetime referencing luminescence detection for pH monitoring in microfluidic free-flow isoelectric focusing, Engineering in Life Sciences. 15 (2015) 276–285. https://doi.org/10.1002/elsc.201400081.

[52] S.M. Grist, L. Chrostowski, K.C. Cheung, Optical Oxygen Sensors for Applications in Microfluidic Cell Culture, Sensors. 10 (2010) 9286–9316. https://doi.org/10.3390/s101009286.

[53] M. Quaranta, S.M. Borisov, I. Klimant, Indicators for optical oxygen sensors, Bioanal Rev. 4 (2012) 115–157. https://doi.org/10.1007/s12566-012-0032-y.

[54] D. Wencel, T. Abel, C. McDonagh, Optical Chemical pH Sensors, Anal. Chem. 86 (2014) 15–29. https://doi.org/10.1021/ac4035168.

[55] X. Wang, O.S. Wolfbeis, R.J. Meier, Luminescent probes and sensors for temperature, Chem. Soc. Rev. 42 (2013) 7834–7869. https://doi.org/10.1039/C3CS60102A.

[56] M. Alexander, A. Bertron, N. De Belie, eds., Performance of Cement-Based Materials in Aggressive Aqueous Environments, Springer Netherlands, Dordrecht, 2013. https://doi.org/10.1007/978-94-007-5413-3.

[57] G. Plusquellec, M.R. Geiker, J. Lindgård, J. Duchesne, B. Fournier, K. De Weerdt, Determination of the pH and the free alkali metal content in the pore solution of concrete: Review and experimental comparison, Cement and Concrete Research. 96 (2017) 13–26. https://doi.org/10.1016/j.cemconres.2017.03.002.

[58] Q. Pu, L. Jiang, J. Xu, H. Chu, Y. Xu, Y. Zhang, Evolution of pH and chemical composition of pore solution in carbonated concrete, Construction and Building Materials. 1 (2012)

519–524. https://doi.org/10.1016/j.conbuildmat.2011.09.006.

[59] J. Stark, B. Wicht, Dauerhaftigkeit von Beton, Springer Berlin Heidelberg, Berlin, Heidelberg, 2013. https://doi.org/10.1007/978-3-642-35278-2.

[60] C.L. Page, M.M. Page, eds., Durability of concrete and cement composites, CRC Press, Boca Raton, Fla., 2007.

[61] A. Behnood, K. Van Tittelboom, N. De Belie, Methods for measuring pH in concrete: a review, Construction and Building Materials. 105 (2016) 176–188. http://dx.doi.org/10.1016/j.conbuildmat.2015.12.032.

[62] O.S. Wolfbeis, Materials for fluorescence-based optical chemical sensors, Journal of Materials Chemistry. 15 (2005) 2657. https://doi.org/10.1039/b501536g.

[63] K. Koren, S.L. Jakobsen, M. Kühl, In-vivo imaging of O2 dynamics on coral surfaces spray-painted with sensor nanoparticles, Sensors and Actuators B: Chemical. 237 (2016) 1095–1101. https://doi.org/10.1016/j.snb.2016.05.147.

[64] M. Larsen, S.M. Borisov, B. Grunwald, I. Klimant, R.N. Glud, A simple and inexpensive high resolution color ratiometric planar optode imaging approach: application to oxygen and pH sensing., Limnology and Oceanography: Methods. 9 (2011) 348–360. https://doi.org/10.4319/lom.2011.9.348.

[65] B.J. Müller, A.V. Zhdanov, S.M. Borisov, T. Foley, I.A. Okkelman, V. Tsytsarev, Q. Tang, R.S. Erzurumlu, Y. Chen, H. Zhang, C. Toncelli, I. Klimant, D.B. Papkovsky, R.I. Dmitriev, Nanoparticle-Based Fluoroionophore for Analysis of Potassium Ion Dynamics in 3D Tissue Models and In Vivo, Advanced Functional Materials. 28 (2018) 1704598. https://doi.org/10.1002/adfm.201704598.

[66] C. Staudinger, J. Breininger, I. Klimant, S.M. Borisov, Near-infrared fluorescent aza-BODIPY dyes for sensing and imaging of pH from the neutral to highly alkaline range, Analyst. 144 (2019) 2393–2402. https://doi.org/10.1039/C9AN00118B.

Part II

Results – Microfluidic Cell Monitoring

3. Measurement of Respiration and Acidification Rates of Mammal Cells in non-PDMS-based Microfluidic Devices

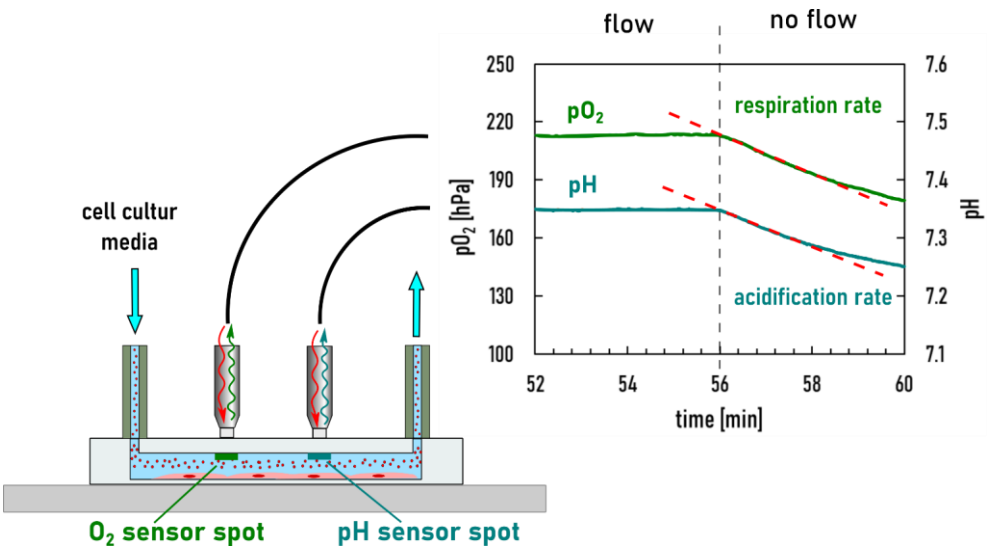

3.1. Preface for the Manuscript

This represents work which has been conducted within the FFG project "NextGenUpCon" (Project number 849791) and focuses on the utilization of thermoplastic microfluidic systems with integrated luminescent sensors as a cell toxicity assay for novel nanomaterials.

The origin of this project was the development of novel upconversion nanoparticles by Prof. Lining Sun and her workgroup located in the University of Shanghai. These particles have the property to absorb two photons of low energy (NIR region) and emit one electron with a higher energy (red or green emission). Therefore, the emission source has lower energy, disturbs biological matter less and has a higher penetration depth. It was attempted to couple these particles with pH sensor dyes from the Analytical Chemistry and Food Chemistry Department at Graz University of Technology to develop novel pH probes.

Risk assessment for new nanomaterials is until now a very difficult and unprecise task which are performed with classical cell cultures in combination with expensive animal models. Especially predictions from cell models are thereby quite problematic since they struggle with sedimentation and exact dosages. Therefore, the second big goal of the project was the development of a microfluidic cell assay capable of monitoring the metabolism of mammalian cells in cooperation with the workgroup of Prof. Peter Ertl, located at Vienna University of Technology, and kdg opticom GmbH, a company specialized on high-precision injection molding. The cell-chip group of Prof. Ertl contributed their expertise in microfluidic design, handling and cell cultivation, Kdg Opticom provided a novel prototyping approach for thermoplastic microfluidic structures and the Department of Analytical Chemistry and Food Chemistry developed the necessary sensor material and the integration technique for microfluidic channels.

This cooperation resulted in a microfluidic prototype chip with four channels, consisting each of two connected 5 µl cell chambers with a channel height of 280 µm. An oxygen sensor spot and a pH sensor spot with sizes of <0.8 mm were integrated in each chamber. COC was used as thermoplastic chip material due to its low oxygen permeability and its good optical properties. The chips were closed with adhesive tape and a COC foil since this technique is the simplest solution for a small series of chips. A new technique for sensor spot integration on structured substrates was developed utilizing a so-called microdispenser. This technique, based on a piezoelectrically driven tappet, allows the fabrication of viscous sensor formulations and spot sizes down to 300 µm, with exact positioning even onto multiple substrates at once. Due to the miniaturization, high efforts were made in order to guarantee a good alignment of the sensor spots and the optical fibers of the miniaturized phasefluorimeter utilized for read-out. A custom-made chip holder allowed for exact repositioning even after removing the read-out device which enables cell inspection with a microscope.

Metabolic parameters of A549 human lung carcinoma cells were measured in these microfluidic chips via stop/flow measurements. The results of the conducted experiments are presented in this publication.

Measurement of Respiration and Acidification Rates of Mammal Cells in non-PDMS-based Microfluidic Devices

This manuscript is submitted as *Full Paper* in

ACS Sensors, 2020 (submitted)

doi: xxx/xxx/xxx

Authors: Bernhard Müller[1], Philipp Sulzer[1], Manuel Walch[2], Helene Zirath[3], Tomas Buryska[3], Mario Rothbauer[3], Peter Ertl[3], Torsten Mayr[1*]

[1] Institute of Analytical Chemistry and Food Chemistry, Graz University of Technology, Stremayrgasse 9, 8010 Graz, Austria

[2] kdg opticomp GmbH, Dorf 91, 6652 Elbigenalp, Austria

[3] Institute of Applied Synthetic Chemistry, Vienna University of Technology, Getreidemarkt 9/163, 1060 Vienna, Austria.

***Corresponding author:** torsten.mayr@tugraz.at

Keywords: Luminescent optical sensor, oxygen and pH measurement, pO_2, online-monitoring, cell culture, cell metabolism, thermoplastic microfluidics

3.2. Abstract

Luminescent chemical sensors have been proven to be a valuable asset in cell cultures and generally in microbiological studies. The presented optical chemical oxygen and pH sensors offer not only the possibility to monitor dissolved oxygen and pH levels in microfluidic devices, but are sensitive enough to enable the measurement of respiration and acidification rates of mammalian cells. Therefore, metabolic changes can be observed with this method by temporarily stopping the incubation flow, barely influencing the cell culture. A thermoplastic polymer is used as oxygen impermeable chip material to enable the measurement of respiration rates, which are not possible with widely used PDMS-based microfluidics. Hence, an innovative fast prototyping strategy is utilized to enable the replication of small series of thermoplastic microfluidic chips. We were able to demonstrate the suitability of this measurement method by monitoring the metabolic response of A549 human lung carcinoma epithelial-like cell line to exposure to FCCP, a drug known for its upregulating effect on respiration and acidification rates. This universal measurement approach can potentially be deployed in all sorts of microfluidic devices and help to retrieve valuable data from inside those systems beyond classical end-point detection methods. Therefore, it complements modern 3D cell cultures and organ-on-chip research with a powerful analytical technology for gathering information over ongoing cell metabolism.

3.3. Introduction

The past decade has seen the rapid development of microfluidic technology in different fields ranging from lab-on-a-chip applications to organ-on-chip technology. To fully take advantage of the controlled and well-defined microfluidic environment, sensor integration into those systems is essential. [1] Particularly since end-point detection methods, like cell viability assays, only allow characterization of highly toxic compounds causing permanent cellular changes. [2] Gathering real-time information from inside microfluidic chips has proven challenging and so far only limited technologies exist, especially with regards to parallelization and multi-parameter read-out. Moreover, most microfluidic devices are designed as a single use platform and therefore low costs of the sensors are essential for a board use.

One common method to gather information from living cell tissue is the measurement of the activity of muscle tissues by observing the bending of flexible pillars. This method does not only measure present forces, but can also evaluate cardiac beat dynamics via pixel analysis of image data as assessment for cardiac health, instead of classical cell viability. [3]–[5] Another method is the utilization of microelectrode arrays (MEAs) to assess electrophysiological dynamics of neuronal and cardiac tissues. [3],[6]–[8] With a similar technique the integrity of barrier tissues like the blood brain barrier, gastrointestinal tract and skin can be investigated noninvasively via transendothelial electrical resistance (TEER) measurements. [9]–[12]

Integration of electrochemical sensors has been utilized for monitoring external parameters in microfluidic systems. For example, detection of dissolved oxygen has been shown with miniaturized electrodes, implemented via inkjet printing technique, in microfluidic devices.[13] Further parameters, like pH [14] and temperature [2], have also been realized as electrochemical sensors. There have also been huge advances in the development of electrochemical immune-biosensors for monitoring soluble biomarkers in recent years. [15],[16] In general, those electrochemical sensors are difficult to integrate, require a reference electrode and in some cases even consume the analyte.

This is not the case for optical detection methods and luminescent optical sensors have proven to be a good approach since they are easy to miniaturize, can be read out externally and can therefore be produced at a low cost. Optical oxygen measurements have been successfully integrated in various applications reaching from micro-bioreactors to cell cultures in cell chambers or microfluidic devices. [17]–[22] Even a pesticide detection module, based on the respiration of algae, has been realized. [23] Luminescent pH measurements are more difficult, due to a lack of stable and bright pH indicators, and are so far mainly done via absorption measurements of the incubation media (phenol red). [2] However, absorption measurements of the media are intrinsically difficult to scale down to small channel heights for true microfluidic systems since a certain pathlength is required to gain sufficient signal intensities.

The possibility of monitoring these extrinsic parameters is already a huge progress in terms of reliable cell conditioning and understanding cell activity. However, it still doesn't enable analysis of cell metabolism and only to a certain extend the examination of non-lethal effects of potentially

toxic substances. In this regard, the measurement of respiration and acidification rates is a much more powerful tool, since those measurements lead to a better understanding of the ongoing cell metabolism. Papkovsky and Dmitriev have summarized the importance of luminescent oxygen sensing for biological detection, especially for determination of respiration rates. [24] So far, such rates were determined in static cell cultures [25] and systems for their measurement have been commercialized. [26] However, static cell culturing conditions mimic physiological conditions only to a certain point and lack resemblance in terms of sheerstress and biomarker concentration. Moreover, risk assessment for new nanomaterials is not possible due to sedimentation and aggregate formation. [27] This leads to a demand in sensor technology capable to perform such respiration and acidification measurements in microfluidic cell cultures and organ-on-chip applications.

Nowadays the majority of such systems utilize PDMS as substrate for microfluidic chips. The problem with this material is, next to its known absorbance properties for biomarkers and drugs due to its lipophilic nature, [28],[29] its high oxygen permeability which does not allow viable oxygen or respiration measurements. For this purpose, oxygen impermeable thermoplastic polymer materials, like COC, PET, PC or even PS, are needed as chip material. Prototyping of thermoplastic materials is however quite difficult and they are usually fabricated with industrial techniques such as injection molding.

Herein, we want to present a microfluidic chip made from thermoplastic, oxygen impermeable COC via an innovative fast-prototyping strategy, equipped with luminescent oxygen and pH sensor spots. With these sensor spots, it is not only possible to monitor the pH and the oxygen concentration inside the microfluidic cell chamber, but via stop/flow measurements, also determine the respiratory and acidification rates of mammalian cells.

3.4. Materials and Methods

3.4.1. Sensor Material

The aza-BODIPY pH indicator dye 4-(7-(4-hydroxyphenyl)-5,5-difluoro-1,9-diphenyl-5H-5l4,6l4-dipyrrolo[1,2c:2′,1′f][1,3,5,2]triazaborinin-3-yl)-N-(2l5,12l3-dodecan-2-yl)benzamide (OHC12) and microcrystalline powder of silanized Egyptian Blue, were synthesized in our lab as previously described. [30],[31] Poly-tert-butylstyrene particles (ptBS particles) stained with 2% (w/w) oxygen sensitive platinum(II)-meso-tetra(4-fluorophenyl)tetrabenzoporphyrin (PtTPTBPF) were prepared as described elsewhere. [32] Hydromed D4, a polyurethane based hydrogel, purchased from AvanSource biomaterials was used as matrix polymer. Buffer substances were bought from Carl Roth GmbH and used without further purification.

3.4.2. Microfluidic Chip

3.4.2.1. Fast Prototyping

A master of the microfluidic chip was 3D printed, con-sisting of four channels with two cell chambers each. With a channel height of 280 µm and a surface area of 18 mm² for each chamber, this leads to a chamber volume of 5 µl (for further details of the chip dimensions see supporting info figure SI1). Via electroplating and resulting Ni deposition, a negative master copy was produced. This negative master has the dimensions of standardized optical media (CD's, DVD's) and was inserted in regular injection molding machines used for their production. Cyclic olefin copolymer (COC) was used for the performed experiments due to its low oxygen permeability and good transparency. Post-processing of the obtained green bodies is necessary, since with this fast prototyping technique no structures deeper than 250 µm can be produced.

The post-processing step includes the manual cutting of the upper halves (= structured part) of the microfluidic chips from the discs and drilling of holes (Ø2 mm) for positioning. Further the surface of the microfluidic chip was scratched with a drill and a stencil and the exact position for the sensor spots was marked. This led to a pattern of two spots per chamber, which was later matched by the arrangement of the optical fibers. After sensor integration (described in 3.4.3) holes with a diameter of 2.5 mm were drilled and pieces of Tygon® R3607 tubing (2.33 mm OD, 0.51 mm ID; Ismatec, IDEX Corporation, Switzerland) were glued into the holes in order to provide ports for the microfluidic system.

3.4.2.2. Chip Bonding

Chips were bonded using 80 µm thick double-sided adhesive tape ARcare 90445 (Adhesive Research). The microfluidic channels were cut out using a CAMM-1 Gs24 cutting plotter (Roland, Germany) equipped with carbide blades (ZEC-U3017; Roland, Germany). The structured tape was removed from the substrate liner, aligned with the structured part of the microfluidic chip (upper half) and manually laminated to ensure proper bonding. After removal of the remaining protective lining layer, the chips were disinfected with the UV lamp of a lamina flow workbench and sealed with a 240 µm thick Topas® COC foil (Denz Biomedical GmbH, Austria) under aseptic conditions.

3.4.3. Sensor Integration

A microdispenser MDS3200+ from VERMES Microdispensing GmbH, equipped with a 70 µm nozzle and a tungsten tappet with a tip diameter of 0.7 mm, was used for sensor integration. It was mounted on a custom-made CNC platform, which was controlled via Linux CNC and allowed exact positioning of the sensor spots. The used printing parameters for oxygen and pH sensors spots are shown in table SI1 in the supporting information.

The pH sensor formulation consists of 0.33 mg of OHC12 dye and 54,8 mg of Egyptian Blue which were suspended in 1380 mg of a solution of hydrogel D4 (8% w/w) in THF/water (9+1). Homogenization was done with a Sonifier® from Branson with 10 one second pules with nine second cooldown intervals. After evaporation of the solvents the resulting sensor spot consisted of

0.2% w/w indicator dye (OHC12), 33.3% w/w reference dye (Egyptian Blue) and 66.5% w/w host polymer (hydrogel D4).

For the O_2 sensor formulation 82.5 mg ptBS particles, stained with 2% PtTPTBPF, were suspended in 1650 mg of a hydrogel D4 solution (5% w/w) in isopropanol/water (3+1). The mixture was homogenized with a Sonifier® from Branson and the resulting sensor consisted of 50% w/w ptBS particles and 50% w/w hydrogel D4 after evaporation of the solvents leading to a relative Pt-dye concentration of 1% w/w.

3.4.4. Sensor Stability

Sensor stability was tested for the pH sensor spots by submerging an unclosed microfluidic chip with a holder into a beaker containing a buffer solution made from 10 mM Tris, 10 mM BisTris, 150 mM NaCl and 1.5 mM NaN_3. The buffer was kept at 37°C and alkaline solution (300 mM NaOH with 10 mM Tris and 10 mM BisTris) and acidic solution (300 mM HCl with 10 mM Tris and 10 mM BisTris) were added automatically with a Cavro® Centris Pump from Tecan to adjust the pH. The pH was measured with a glass pH electrode and a NaCl filled reference electrode from Idronaut. The stability test ran for 10 days at pH 7.5 and once a day a calibration between pH 5 and 9 was done with 18 distinct pH values. The read-out of the sensor spots was conducted with a miniaturized phaseflourimeter (Firesting) from Pyroscience equipped with 1-meter-long, polished POF 1/2.2 mm fibers. The measurement settings can be found in table SI2 (supporting info). The cotangents of the measured phaseangle was plotted against the pH value und the calibration function was obtained by fitting with a Boltzmann equation (Eq. 1) where *A* represents the top value under acidic conditions, *B* the bottom value under basic conditions, *pKa* the apparent pKa value and *slope* the slope at the pKa value.

$$\cot(d\varphi) = B + \frac{A-B}{1+10^{\frac{pH-pKa}{slope}}} \qquad \textbf{Eq. 1}$$

For the oxygen sensor spots no distinct durability tests were performed since their stability has been shown in previous reports. [17],[19],[23]

3.4.5. Set Up

A chip holder was constructed in order to guarantee a good alignment of the optical fibers from the read-out device with the sensor spots in the microfluidic channels. The holder consists of a frame holding the chip and an optic block which positions the fibers. The optic block can be removed in order to allow inspection of the cells in the fluidic chamber via microscope. A CAD drawing of the holder can be found in the supporting information (Figure SI 2). Since eight chambers, with two spots each, were incubated in parallel on one chip, read-out was done with four separate four-channel Firesting phasefluorimeters from Pyroscience equipped with 1 meter polished POF 1/2.2 mm fibers. The chip holder with the microfluidic chip was placed on a heated stage with integrated temperature control, which was set to 37°C. For fluid transport a four-syringe KDS 250 syringe pump (KD Scientific, USA) was used with 20 mL glass syringes (ILS, Germany) connected

to 1/32" PEEK tubing (Ismatec, Germany) via 4-way PEEK valves (IDEX Health & Science, USA). A microfluidic bubble trap system, comprising of nine circular 1 mm diameter trapping wells (250 µm height), was used as preheating, as well as bubble trapping unit. The bubble trap was then directly connected with the cultivating chambers via 4 cm long 1/32" PEEK tubing. A picture of the assembled set-up is shown in SI3 (supporting information).

3.4.6. Calibration

3.4.6.1. O_2

Since the used sensor material was the same used by Nacht et. al, their calibration data were used as factory setting for the oxygen sensor spots. [32] A two-point calibration at anoxic conditions and air-saturated conditions was performed for one spot at 37°C in cell medium to account for the slight changes environment and used for all oxygen sensor spots. Anoxic conditions were established by adding $NaSO_3$, air saturated conditions by shaking the medium right before measurement. The measurement settings for the phasefluorimeter can be found in table SI2 (supporting information).

3.4.6.2. pH

Calibration of the pH sensor spots was performed with 10% FCS supplemented cell culture medium (Gibco) spiked with 10 mM of a buffer substance (acetate, Mes, Tris or glycin) between pH 4.5 and pH 10. The buffer substance with the appropriate pKa value was dissolved in the media, the pH adjusted with 1 M NaOH or 1M HCl at 37°C and afterwards filtered through a 0.45 µm sterile filter (VWR, Austria). A list with the used buffers and their pH can be found in table SI3 in the supporting information. The buffers were transferred under aseptic conditions within a laminar-flow cabinet into 20 mL glass syringes and manually flushed through the microfluidic chip. The measurement settings for the phasefluorimeter can be found table SI2 (supporting information).

3.4.7. Cell Seeding

3.4.7.1. Pretreatment

In order to get aseptic surfaces in the microfluidic chips, the structured parts, containing the sensor spots, were treated with UV light (λ~250 nm) from the laminar flow workbench for 15 minutes prior to chip bonding. Microfluidic tubing, valves, the double adhesive tape and the COC foil were desinfected with 70% ethanol. In a second step, the COC foil is treated with ambient oxygen plasma for 10 minutes using a plasma chamber (Harrick Plasma, USA) equipped with an Equinox pressure control unit (Blackhole Lab, France) for 2 minutes at 450 mTorr to enhance cell adhesion on the polymer surfaces. The chip was bonded according to 3.4.2.2 at aseptic conditions. To enable a fast cell adhesion and keeping the incubation time as short as possible, the closed chip was treated with a 1% collagen I (Sigma Al-drich) solution in PBS (Sigma Aldrich) for one hour. In the next step the chips were flushed with supplemented RPMI 1640 medium (Gibco) and the sensor spots calibrated according to 3.4.6.

3.4.7.2. Seeding and Incubation

A549 human lung carcinoma epithelial-like cell line (ATCC) were cultured in a RPMI 1640 Medium (Gibco) supplemented with 10% fetal bovine serum, L-glutamine, and 1% antibiotic/antimycotic solution. The trypsinized cells, with a concentration of 10^6 cells/mL, were loaded in into the calibrated microfluidic chips and seeding was observed under the microscope. The oxygen concentration within the chambers was checked via the sensor spots, to prevent oxygen limitation. After 4 hours, cell seeding was complete and a confluent cell layer has formed. The cells were cultivated within the chip at a tempter of 37°C and with constant perfusion of media of 10 µL/min. Cell density was evaluated by counting cells stained with Hoechst 33342 fluorescent dye with ImageJ software after the end of the experiments.

3.4.8. Acidification and Respiration Rate Measurement

The acidification and respiration rate of the cells were analyzed by stopping the flow for approximately 30 minutes. Afterwards the flow was turned on again (10 µL/min) and the chip flushed with fresh media until the oxygen saturation and pH level returned to normal.

In order to see a change in the metabolism the cells were poisoned with FCCP (Carbonyl cyanide-4-(trifluoromethoxy)phenylhydrazone from Sigma Al-drich) which leads to an upregulation of the respiratory rate and the acidification rate. [24] The cells were incubated with media spiked with 0.5, 5 and 20 µM FCCP for 5.5 hours and the acidification rates and respiration rates measured multiple times.

3.5. Results and Discussion

3.5.1. Sensor Materials

The sensor materials are chosen according to previous experiences and reports and are immobilized in a hydrogel D4 matrix. This swellable material is FDA approved and designed in a way so proteins do not adhere to it. Therefore, it is not possible for cells to grow on it, effectively shielding the sensitive dyes from the cells and eliminating otherwise possible interactions. No adverse effects of the sensor material to the cells thus has been observed so far (Figure SI4, supporting information).

Oxygen measurements are performed with PtBS particles stained with PtTPTBPF since they have proven their stability and suitability for measurements in biological systems multiple times. [17],[23],[32] They can be excited with red light (620 nm) and emit in the near infrared (NIR) part of the electromagnetic spectrum. The lifetime of the excited dye molecule is proportional to the oxygen partial pressure and is used as a robust, intensity independent parameter.

The pH sensitive OHC12 dye has a reported apparent pKa value of 7.59 in hydrogel D4 [30] and is therefore perfectly suited to monitor the decrease in pH in cell culture media from pH 7.5 to pH 6.5. It is used together with Egyptian Blue particles as an inert, phosphorescent reference with similar

spectral properties as the indicator dye to enable dual-lifetime referenced (DLR) meas-urements. [33],[34] This technique is reportedly more robust than simple intensity measurements and therefore small changes in pH can be detected more reliably. The pH indicator and the reference material both can be excited with red light (620 nm) and emit light in the NIR part of the electromagnetic spectrum. The stability of the pH sensor spots at 37 °C was investigated over 10 days. The daily calibration points are fitted with a Boltzmann equation (Eq. 1) and the respective curves are shown in figure 1. A slight drift of about 0.01 pH units per day can thereby be observed at the point of inflection. This drift is acceptable, keeping in mind that only the relative change of the pH over two minutes is measured to determine the acidification rate.

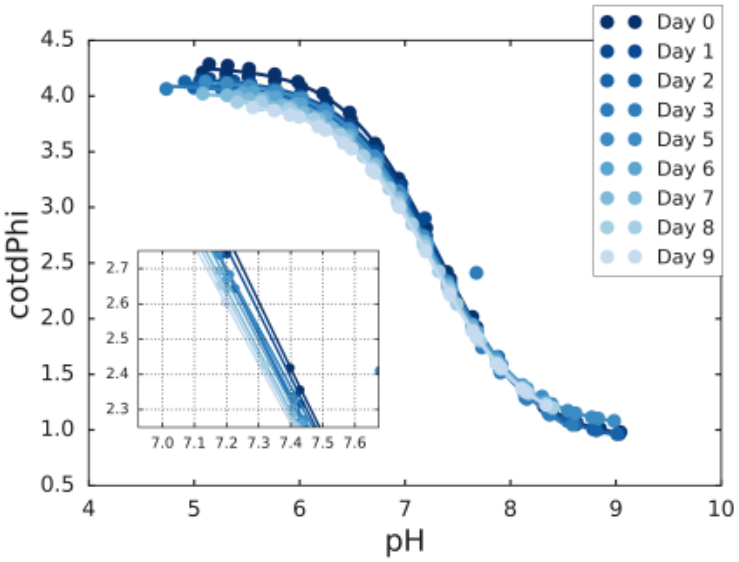

Figure 1: Sigmoidal calibration curves of the pH sensor spot in the course of 10 days. A shift in the apparent pKa of around 0.01 pH unit per day can be observed.

3.5.2. Microfluidic Chip Fabrication and Sensor Integration

PDMS is the most common material for microfluidic chips for cell conditioning. The material is known for its ease of fabrication and its excellent oxygen permeability, leading to air-saturated conditions in the cell media. However, PDMS is also known for its unspecific binding of substances due to the lipophilic character of the material. [28],[29] In order to be able to perform respiration measurements an oxygen impermeable chip material was used. COC has an oxygen permeability as low as 18.52 cm^3 mm/m^2 day atm [35], very good optical properties and good biocompatibility and is consequently a suitable material for respiration measurements of cells in a microfluidic device. Therefor the injection molded structured part of the chip, as well as the cover foil is made from this material. However, processing of thermoplastic materials is significantly more effort when, due to small chip numbers, fabrication methods for mass production are not an option. This problem is addressed by utilizing a novel fast prototyping method. The method allows the fabrication of microfluidic green bodies made from thermoplastic materials, utilizing conventional injection molding machines for optical media such as compact discs. Manufacturing of the needed inlays

comes at reasonable costs even for small series of prototype chips. Therefore, a master chip gets covered with nickel via electroplating, forming the inlay yielding a negative master of the chip structure. The technique is compromised by a limited structural height of 250 µm and therefore no possibility for holes. Figure 2b shows the 200 µm deep structure of the designed chip, whereas in figure 2c a ready-made green body can be seen. Subsequently the chips have to be cut out from the disc and holes for positioning and the fluidic ports have to be drilled during post-processing. Further the substrate was scratched with a drill and a stencil at the exact locations where the sensor spots are afterwards placed. This marks enable the exact positioning of the spots and subsequently allow the alignment with the optical fibers. Moreover, the rough mark improves the adhesion of the hydrogel-based sensor spot to the smooth COC surface by enhancing the mechanical link between the two materials.

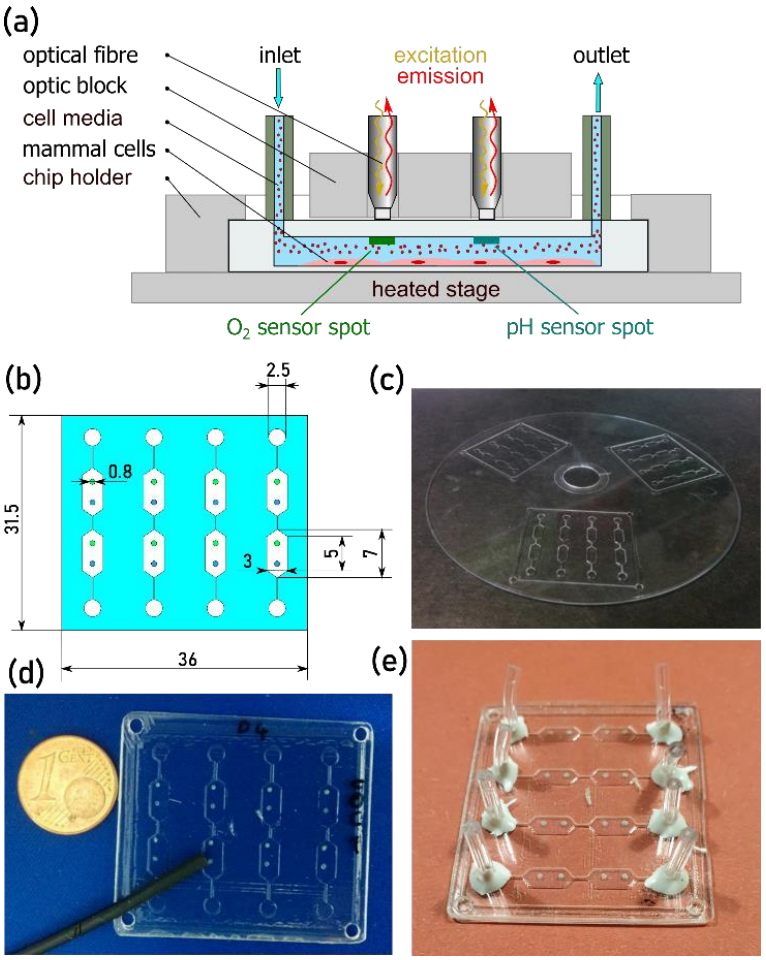

Figure 2: Different development stages of the microfluidic chip; (a) Utilized concept of the microfluidic chip; (b) Sketch of the prototype after which the 3D print is modeled; (c) Green body of the chip in shape of an optical media after injection molding; (d) Structured part of the chip after drilling of positioning holes and sensor integration; (e) Fully assembled microfluidic chip with ports before collagen treatment.

The sensor material is deployed into the chambers of the chip via so called microdispensing. This technique utilizes a piezoelectrically driven tappet to mechanically force the sensor formulation through a nozzle. With this method, viscos solutions and dispersions can be processed. This is key for processing the pH sensor formulation, since it needs to be quite viscose to prevent fast sedimentation of the ceramic reference particles. It allows using particle sizes up to 10 µm in diameter and is capable of printing into chambers and channels of microfluidic devices, which cavities can be as deep as 5 mm. Depending on the settings and sensor formulation, sensor spots as small as 500 µm can be printed. The dispenser is mounted on a custom-made CNC platform allowing exact positioning of the sensor spot. Since the optical fibers used for read-out have an inner diameter of 1 mm, the goal is to produce spots, which are smaller, so the entire spot contributes to the signal. Since the average size of the produced sensor spots is around 0.8 mm this is achieved and therefore inhomogeneities within one spot do not affect its overall signal. Figure 2d shows the chip after sensor integration and allows for a size comparison between the optical fiber and the sensor spot.

The simple port system is fabricated utilizing pieces of Tygon tubing. They are glued into holes drilled in the structured part of the chip. The inner diameter (0.51 mm) of this flexible material is a little bit smaller than the outer diameter (0.79 mm) of the PEEK tubing, used for connecting the fluidic system, allowing a tight fit. The chips are closed using a double-sided adhesive tape from which the structure of the microfluidic channels has been previously removed. It is 80 µm thick and contributes to the total height of the microfluidic structure. After laminating the tape onto the structured part of the chip it is disinfected with UV light. The COC cover foil is treated with ambient oxygen plasma to disinfect it and activate its surface at the same time. The chip is afterwards assembled in a laminar flow workbench, treated with collagen and the ports are closed with disinfected plugs. The chips are stored this way until they are calibrated right before use. Figure 2e shows such an assembled chip right before the collagen treatment.

3.5.3. Set-Up Characterization

In order to gain stabile results, a good alignment between the optical fiber and the sensor spot has to be guaranteed. Therefore, a chip holder is manufactured, consisting of a frame for positioning the microfluidic chip and an optical block, which supports the polished POF fibers. The frame features a pocket at the bottom in which the microfluidic chip is positioned with four pins. The pocket has the same height as the chip and therefore presses it down when assembled on a heated stage. The window in the frame is big enough to enable microscopic inspection of the cell chambers and allow connection of the tubing to the chip. The optic block is positioned with four bolts and screw nuts in the optical window. It holds up to 16 POF fibers (two for each cell chamber) and presses them onto the topside of the chip right above the sensor spots. The CAD drawing of the chip holder is shown in figure SI2 (supporting information).

In order to minimize bubble formation during incubation, all culture media is degassed at 37°C and stored in glass syringes. Further, a bubble trap is deployed right before the cell chamber in order to preheat the media and capture bubbles before entering the microfluidic chamber during incubation.

The pH sensor spots are calibrated by fitting the measurement points with the Boltzmann equation (Eq.1). Figure 3 shows the calibration curves for all eight pH sensor spots of one microfluidic chip. The maximal value under acidic conditions (top value A) is different for each spot due to small variations in the ratio between the indicator dye and the reference particles. These inhomogenities of the sensor material are caused during the microdispensing process of the dispersion due to the density difference between the polymer solution and the ceramic reference particles. However, the fluctuation of the top value barely influences the apparent pKa (values displayed in figure 3) leading to similar sensor characteristics. The pH measurements of the cell cultures are carried out between pH 7.5 and 6.8 and are therefore perfectly covered by the pH sensors linear range.

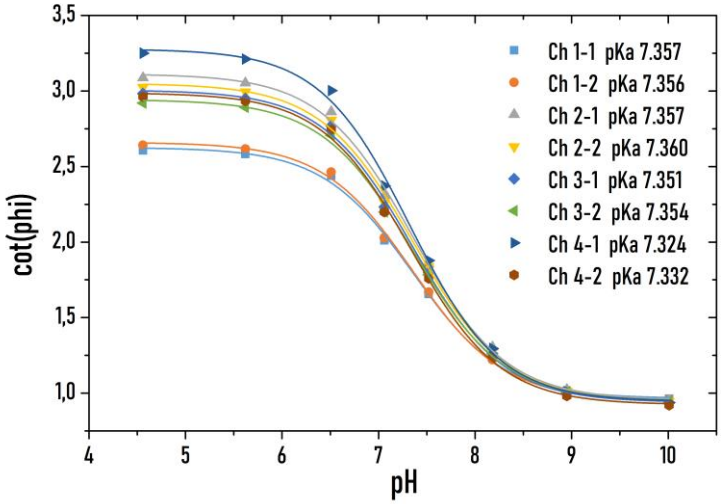

Figure 3: Sigmoidal calibration curves of eight pH sensor spots located in one chip showing different top values but similar apparent pKa values.

3.5.4. Cell cultivation

The microfluidic chip is treated with collagen right after assembling to guarantee a fast cell adhesion. (<4h). The oxygen levels during the seeding procedure are monitored with the oxygen sensor spots to ensure a sufficient O_2 supply. The oxygen concentration did not decrease under 22 hPa (≙ 10% air saturation). Fig 4 shows a microscopic image of the cells after seeding, just before staring the incubation flow confirming a confluent layer of cells.

A549 human lung carcinoma epithelial-like cell line (ATCC) is used as a robust model system. The cell line shows a high metabolic activity and is a suitable model for toxicological screening since it is a human lung cell-line. [36]

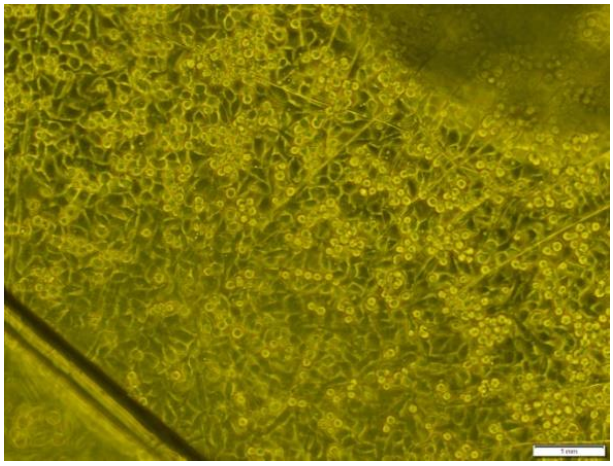

Figure 4: Microscopic image of A549 human lung carcinoma epithelial-like cell line (ATCC) before starting incubation flow. In the top right corner of the image the pH sensor spot, located at the topside of the chamber, is visible (out-of-focus).

3.5.5. Acidification and Respiration Rate Measurements

The cells are incubated with a flow of 10 µl/min, guaranteeing air saturation of the cell media and therefore a sufficient oxygen supply for the cells. The incubation flow is stopped for the acidification and respiration measurements and the decrease in oxygen and pH monitored. Figure 5 shows four consecutive measurements conducted 44 hours after cell seeding. The flow of culture media is stopped for approximately 30 minutes, never letting the oxygen concentration decrees beyond 10% air saturation (22hPa). It is visible that the cell concentration in the second chamber (pO_2 Ch 2-2) is higher than in the first chamber (pO_2 Ch 2-1) leading to a faster decrease of pO_2, respectively a steeper slope. Interestingly, the oxygen saturation in the second chamber does not reach air saturation, even during the incubation flow. This is probably due the respiratory behavior of the cells in the first chamber and shows how oxygen impermeable the used system is. The effect of metabolic activity of the cells in the first chamber can also be seen at the slightly lower pH during incubation flow in the second chamber. However, this effect is way less pronounced for pH.

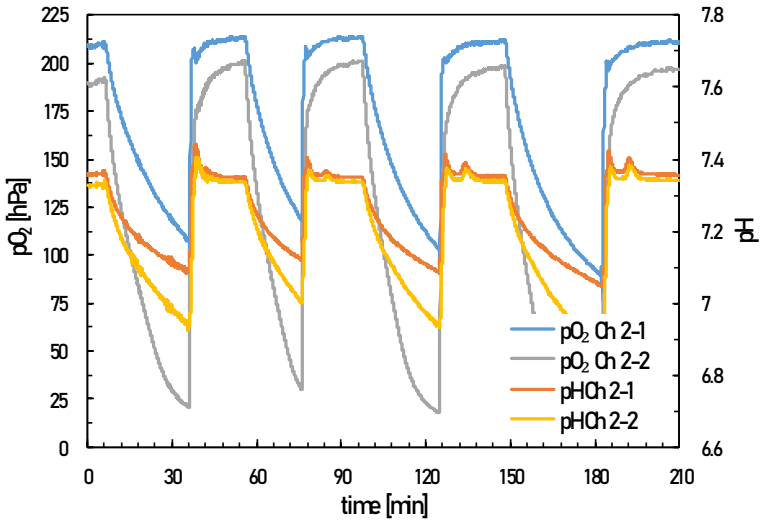

Figure 5: Stop/flow measurements for the determination of acidification and respiration rates. Shown are two consecutive chambers of one channel 44 hours after seeding.

To get acidification and respiration rates, the slopes of the drops after stopping the incubation flow, are analyzed. The first 60 measurement points (e.g. two minutes) show the most stable results and are therefore sufficient to determine the respiration and acidification rates. Figure 6 shows two sets of measurements from channel 2, conducted 18 and 44 hours after seeding with multiple measurements conducted at each point. Obviously, the repeatability of the measurement is good and only slight differences are visible, showing the usefulness of this method. Within each set, a measurement was done every 30 minutes. Since the cell concentration was different between the two chambers, the respiration and acidification rates are different as well. Interestingly, the gap between the difference in acidification rate and respiration rate is not the same. This is probably due to a different apparent buffer capacity of the media in the chamber originating from a different starting pH value.

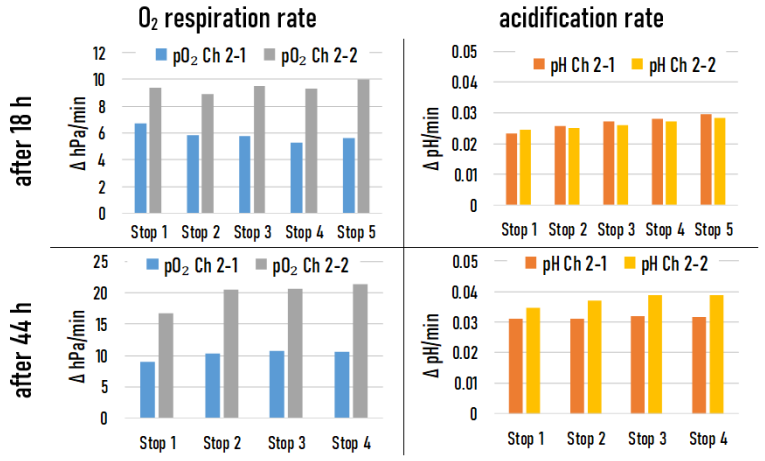

Figure 6: Respiration and acidification rates of A549 human lung carcinoma epithelial-like cell line (ATCC) 18 and 44 hours after seeding. Repeated measurements are done every 30 minutes.

To show the potential of the oxygen and pH sensor spots for the evaluation of the metabolism of living cells, ATTC cells are incubated with FCCP and their response is monitored. FCCP is a compound known for is upregulating effect on the respiration and acidification rate. [24] This effect can be reproduced in the conducted poisoning study shown in figure 7. After seeding and an initial growth phase, three chambers are incubated with different concentrations of FCCP. A strong increase in the acidification and respiration rate can be observed for the concentrations of 0.5 and 5 µM. However, for the chamber incubated with 20 µM this was not the case. The best explanation is, that the high concentration is lethal to the cells and therefore no increase is visible. Since the cell count is only determined at the end of the poisoning experiment it is not possible to correct the measured rates for the cell count of living cells at that moment of the measurement.

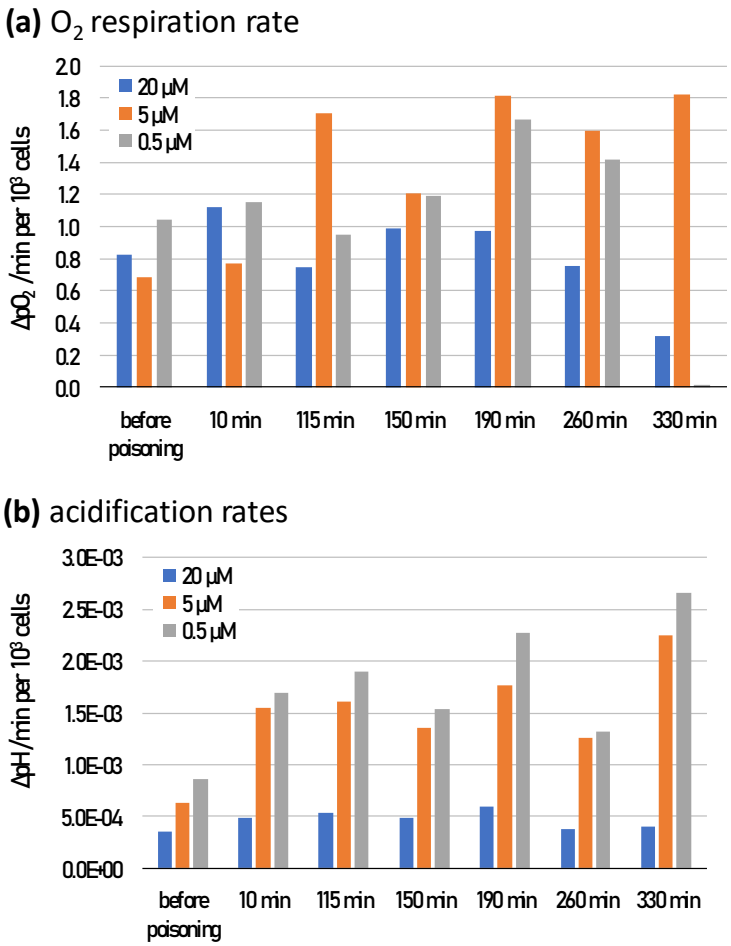

Figure 7: Development of respiration (A) and acidification (B) rates of A549 human lung carcinoma epithelial-like cell line (ATCC) during incubation with three different concentrations of FCCP.

3.6. Conclusion and Outlook

In conclusion, microfluidic chips, made from thermoplastic COC, were fabricated via a fast prototyping strategy for injection molding. Luminescent oxygen and pH sensor spots were integrated in the cell chambers using a microdispenser. Sensor spots with a diameter of around

0.8 mm were produced with this technique, showing sufficient signal intensity for contactless read-out with optical fibers connected to a miniaturized phasefluorimeter. Afterwards, the chips were manually closed with adhesive tape and ATCC cells seeded in the incubation chambers of the chip. Oxygen and pH levels were monitored for several days and multiple respiration and acidification rate measurements were carried out showing matching results. The effect of FCCP, a drug responsible for an upregulation of the respiration and acidification rate, on the metabolism of ATCC cells was successfully monitored via a series of consecutive measurements.

Further work will focus on the enhancement of the microfluidic system improving channel dimensions and the port system. Moreover, the optimization of the spotting process will enable a simpler calibration routine with 2-point or 1-point calibration. Overall, the goal is to improve the reliability and ease-of-use of the system to enable high-throughput data collection and subsequent comparison with existing data. The sensor technology, including integrated sensing elements and read-out systems, can be easily transferred to other existing microfluidic platforms. This is of tremendous interest for 3D cell cultures and organ-on-chip systems, since there is a lack of inline analytical methods for the determination of the cell metabolism and monitoring of culture conditions.

Acknowledgements

Financial support by the Austrian Research Promotion Agency (FFG) in the project NextGenUpCon (Project number 849791) is gratefully acknowledged.

3.7. References

[1] J.H. Sung, Y.I. Wang, N. Narasimhan Sriram, M. Jackson, C. Long, J.J. Hickman, M.L. Shuler, Recent Advances in Body-on-a-Chip Systems, Anal. Chem. 91 (2019) 330–351. https://doi.org/10.1021/acs.analchem.8b05293.

[2] Y.S. Zhang, J. Aleman, S.R. Shin, T. Kilic, D. Kim, S.A. Mousavi Shaegh, S. Massa, R. Riahi, S. Chae, N. Hu, H. Avci, W. Zhang, A. Silvestri, A. Sanati Nezhad, A. Manbohi, F. De Ferrari, A. Polini, G. Calzone, N. Shaikh, P. Alerasool, E. Budina, J. Kang, N. Bhise, J. Ribas, A. Pourmand, A. Skardal, T. Shupe, C.E. Bishop, M.R. Dokmeci, A. Atala, A. Khademhosseini, Multisensor-integrated organs-on-chips platform for automated and continual in situ monitoring of organoid behaviors, Proc. Natl. Acad. Sci. 114 (2017) E2293–E2302. https://doi.org/10.1073/pnas.1612906114.

[3] C. Oleaga, A. Riu, S. Rothemund, A. Lavado, C.W. McAleer, C.J. Long, K. Persaud, N.S. Narasimhan, M. Tran, J. Roles, C.A. Carmona-Moran, T. Sasserath, D.H. Elbrecht, L. Kumanchik, L.R. Bridges, C. Martin, M.T. Schnepper, G. Ekman, M. Jackson, Y.I. Wang, R. Note, J. Langer, S. Teissier, J.J. Hickman, Investigation of the effect of hepatic metabolism on off-target cardiotoxicity in a multi-organ human-on-a-chip system, Biomaterials. 182 (2018) 176–190. https://doi.org/10.1016/j.biomaterials.2018.07.062.

[4] C. Oleaga, C. Bernabini, A.S.T. Smith, B. Srinivasan, M. Jackson, W. McLamb, V. Platt, R. Bridges, Y. Cai, N. Santhanam, B. Berry, S. Najjar, N. Akanda, X. Guo, C. Martin, G. Ekman, M.B. Esch, J. Langer, G. Ouedraogo, J. Cotovio, L. Breton, M.L. Shuler, J.J. Hickman, Multi-Organ toxicity demonstration in a functional human in vitro system composed of four organs, Sci. Rep. 6 (2016). https://doi.org/10.1038/srep20030.

[5] F. Qian, C. Huang, Y.-D. Lin, A.N. Ivanovskaya, T.J. O'Hara, R.H. Booth, C.J. Creek, H.A. Enright, D.A. Soscia, A.M. Belle, R. Liao, F.C. Lightstone, K.S. Kulp, E.K. Wheeler, Simultaneous electrical recording of cardiac electrophysiology and contraction on chip, Lab. Chip. 17 (2017) 1732–1739. https://doi.org/10.1039/C7LC00210F.

[6] B.M. Maoz, A. Herland, O.Y.F. Henry, W.D. Leineweber, M. Yadid, J. Doyle, R. Mannix, V.J. Kujala, E.A. FitzGerald, K.K. Parker, D.E. Ingber, Organs-on-Chips with combined multi-electrode array and transepithelial electrical resistance measurement capabilities, Lab. Chip. 17 (2017) 2294–2302. https://doi.org/10.1039/C7LC00412E.

[7] M. Stancescu, P. Molnar, C.W. McAleer, W. McLamb, C.J. Long, C. Oleaga, J.-M. Prot, J.J. Hickman, A phenotypic in vitro model for the main determinants of human whole heart function, Biomaterials. 60 (2015) 20–30. https://doi.org/10.1016/j.biomaterials.2015.04.035.

[8] E. Moutaux, B. Charlot, A. Genoux, F. Saudou, M. Cazorla, An integrated microfluidic/microelectrode array for the study of activity-dependent intracellular

dynamics in neuronal networks, Lab. Chip. 18 (2018) 3425–3435. https://doi.org/10.1039/C8LC00694F.

[9] D. Elbrecht, C. Long, J. Hickman, Transepithelial/endothelial Electrical Resistance (TEER) theory and applications for microfluidic body-on-a-chip devices, J. Rare Dis. Res. Treat. 1 (2016) 46–52. https://doi.org/10.29245/2572-9411/2016/3.1026.

[10] Y.I. Wang, H.E. Abaci, M.L. Shuler, Microfluidic blood–brain barrier model provides in vivo-like barrier properties for drug permeability screening, Biotechnol. Bioeng. 114 (2017) 184–194. https://doi.org/10.1002/bit.26045.

[11] M.B. Esch, H. Ueno, D.R. Applegate, M.L. Shuler, Modu-lar, pumpless body-on-a-chip platform for the co-culture of GI tract epithelium and 3D primary liver tissue, Lab. Chip. 16 (2016) 2719–2729. https://doi.org/10.1039/C6LC00461J.

[12] F.A. Alexander, S. Eggert, J. Wiest, Skin-on-a-Chip: Transepithelial Electrical Resistance and Extracellular Acidification Measurements through an Automated Air-Liquid Interface, Genes. 9 (2018) 114. https://doi.org/10.3390/genes9020114.

[13] A. Moya, M. Ortega-Ribera, X. Guimerà, E. Sowade, M. Zea, X. Illa, E. Ramon, R. Villa, J. Gracia-Sancho, G. Gabriel, Online oxygen monitoring using integrated inkjet-printed sensors in a liver-on-a-chip system, Lab. Chip. 18 (2018) 2023–2035. https://doi.org/10.1039/C8LC00456K.

[14] I.A. Ges, B.L. Ivanov, D.K. Schaffer, E.A. Lima, A.A. Werdich, F.J. Baudenbacher, Thin-film IrOx pH microelectrode for microfluidic-based microsystems, Biosens. Bioelectron. 21 (2005) 248–256. https://doi.org/10.1016/j.bios.2004.09.021.

[15] R. Riahi, S.A.M. Shaegh, M. Ghaderi, Y.S. Zhang, S.R. Shin, J. Aleman, S. Massa, D. Kim, M.R. Dokmeci, A. Khademhosseini, Automated microfluidic platform of bead-based electrochemical immunosensor integrated with bioreactor for continual monitoring of cell secreted biomarkers, Sci. Rep. 6 (2016) 1–14. https://doi.org/10.1038/srep24598.

[16] S.R. Shin, Y.S. Zhang, D.-J. Kim, A. Manbohi, H. Avci, A. Silvestri, J. Aleman, N. Hu, T. Kilic, W. Keung, M. Righi, P. Assawes, H.A. Alhadrami, R.A. Li, M.R. Dokmeci, A. Khademhosseini, Aptamer-Based Microfluidic Electrochemical Biosensor for Monitoring Cell-Secreted Trace Cardiac Biomarkers, Anal. Chem. 88 (2016) 10019–10027. https://doi.org/10.1021/acs.analchem.6b02028.

[17] S.L. Maldonado, P. Panjan, S. Sun, D. Rasch, A.M. Sesay, T. Mayr, R. Krull, A fully online sensor-equipped, disposable multiphase microbioreactor as a screening platform for biotechnological applications, Biotechnol. Bioeng. 116 (2019) 65–75. https://doi.org/10.1002/bit.26831.

[18] H. Zirath, M. Rothbauer, S. Spitz, B. Bachmann, C. Jordan, B. Müller, J. Ehgartner, E. Priglinger, S. Mühleder, H. Redl, W. Holnthoner, M. Harasek, T. Mayr, P. Ertl, Every

Breath You Take: Non-invasive Real-Time Oxygen Biosensing in Two- and Three-Dimensional Microfluidic Cell Models, Front. Physiol. 9 (2018). https://doi.org/10.3389/fphys.2018.00815.

[19] J. Ehgartner, P. Sulzer, T. Burger, A. Kasjanow, D. Bouwes, U. Krühne, I. Klimant, T. Mayr, Online analysis of oxygen inside silicon-glass microreactors with integrated optical sensors, Sens. Actuators B Chem. 228 (2016) 748–757. https://doi.org/10.1016/j.snb.2016.01.050.

[20] P. Gruber, M.P.C. Marques, N. Szita, T. Mayr, Integration and application of optical chemical sensors in microbioreactors, Lab. Chip. 17 (2017) 2693–2712. https://doi.org/10.1039/C7LC00538E.

[21] S.A. Pfeiffer, S. Nagl, Microfluidic platforms employing integrated fluorescent or luminescent chemical sensors: a review of methods, scope and applications, Methods Appl. Fluoresc. 3 (2015) 034003. https://doi.org/10.1088/2050-6120/3/3/034003.

[22] S. Sun, B. Ungerböck, T. Mayr, Imaging of oxygen in microreactors and microfluidic systems, Methods Appl. Fluoresc. 3 (2015) 034002. https://doi.org/10.1088/2050-6120/3/3/034002.

[23] I.B. Tahirbegi, J. Ehgartner, P. Sulzer, S. Zieger, A. Kasjanow, M. Paradiso, M. Strobl, D. Bouwes, T. Mayr, Fast pesticide detection inside microfluidic device with integrated optical pH, oxygen sensors and algal fluorescence, Biosens. Bioelectron. 88 (2017) 188–195. https://doi.org/10.1016/j.bios.2016.08.014.

[24] D.B. Papkovsky, R.I. Dmitriev, Biological detection by optical oxygen sensing, Chem. Soc. Rev. 42 (2013) 8700–8732. https://doi.org/10.1039/C3CS60131E.

[25] J. Hynes, T.C. O'Riordan, A.V. Zhdanov, G. Uray, Y. Will, D.B. Papkovsky, In vitro analysis of cell metabolism using a long-decay pH-sensitive lanthanide probe and extracellular acidification assay, Anal. Biochem. 390 (2009) 21–28. https://doi.org/10.1016/j.ab.2009.04.016.

[26] D.A. Ferrick, A. Neilson, C. Beeson, Advances in measuring cellular bioenergetics using extracellular flux, Drug Discov. Today. 13 (2008) 268–274. https://doi.org/10.1016/j.drudis.2007.12.008.

[27] S.K. Mahto, V. Charwat, P. Ertl, B. Rothen-Rutishauser, S.W. Rhee, J. Sznitman, Microfluidic platforms for advanced risk assessments of nanomaterials, Nanotoxicology. 9 (2015) 381–395. https://doi.org/10.3109/17435390.2014.940402.

[28] M. W. Toepke, D. J. Beebe, PDMS absorption of small molecules and consequences in microfluidic applications, Lab. Chip. 6 (2006) 1484–1486. https://doi.org/10.1039/B612140C.

[29] R. Gomez-Sjoberg, A.A. Leyrat, B.T. Houseman, K. Shokat, S.R. Quake, Biocompatibility

and Reduced Drug Absorption of Sol–Gel-Treated Poly(dimethyl siloxane) for Microfluidic Cell Culture Applications, Anal. Chem. 82 (2010) 8954–8960. https://doi.org/10.1021/ac101870s.

[30] M. Strobl, T. Rappitsch, S.M. Borisov, T. Mayr, I. Klimant, NIR-emitting aza-BODIPY dyes – new building blocks for broad-range optical pH sensors, Analyst. 140 (2015) 7150–7153. https://doi.org/10.1039/C5AN01389E.

[31] S.M. Borisov, C. Würth, U. Resch-Genger, I. Klimant, New Life of Ancient Pigments: Application in High-Performance Optical Sensing Materials, Anal. Chem. 85 (2013) 9371–9377. https://doi.org/10.1021/ac402275g.

[32] B. Nacht, C. Larndorfer, S. Sax, S.M. Borisov, M. Hajnsek, F. Sinner, E.J.W. List-Kratochvil, I. Klimant, Integrated catheter system for continuous glucose measurement and simultaneous insulin infusion, Biosens. Bioelectron. 64 (2015) 102–110. https://doi.org/10.1016/j.bios.2014.08.012.

[33] C. Huber, I. Klimant, C. Krause, T. Werner, T. Mayr, O.S. Wolfbeis, Optical sensor for seawater salinity, Fresenius J. Anal. Chem. 368 (2000) 196–202. https://doi.org/10.1007/s002160000493.

[34] C. Huber, I. Klimant, C. Krause, O.S. Wolfbeis, Dual Lifetime Referencing as Applied to a Chloride Optical Sensor, Anal. Chem. 73 (2001) 2097–2103. https://doi.org/10.1021/ac9914364.

[35] T.E. Pedersen, Evaluation of polymer properties influencing oxygen transfer rates (OTR) in microfluidic cell culture, Graz Univ. Technol. Master's Thesis (2017).

[36] J. Li, S. Zhao, X. Zhou, T. Zhang, L. Zhao, P. Miao, S. Song, X. Sun, J. Liu, X. Zhao, G. Huang, Inhibition of Lipolysis by Mercaptoacetate and Etomoxir Specifically Sensitize Drug-Resistant Lung Adenocarcinoma Cell to Paclitaxel, PLoS ONE. 8 (2013). https://doi.org/10.1371/journal.pone.0074623.

3.8. Supporting Information

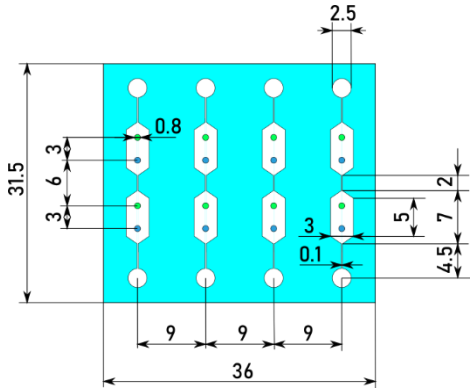

Figure SI1: Dimensions of the microfluidic chip. The depth of the structure is 200 µm.

Table SI1: Printing parameters for the microdispenser

	O_2 sensor spots	pH sensor spots
tappet lift	65%	65%
rising time	0.3 ms	0.2 ms
opening time	0.1 ms	0 ms
falling time	0.1 ms	0.07 ms
number of pulses	3	3
delay	0.1 ms	0.1 ms
reservoir pressure	0.4 bar	1 bar
number of repetitions	1	2

Table SI2: Measurement settings for the phasefluorimeters

	O_2	pH
measurement frequency	4000 Hz	2000 Hz
LED intensity	40%	100%
amplification	400x	400x
measuring time	50 ms	50 ms

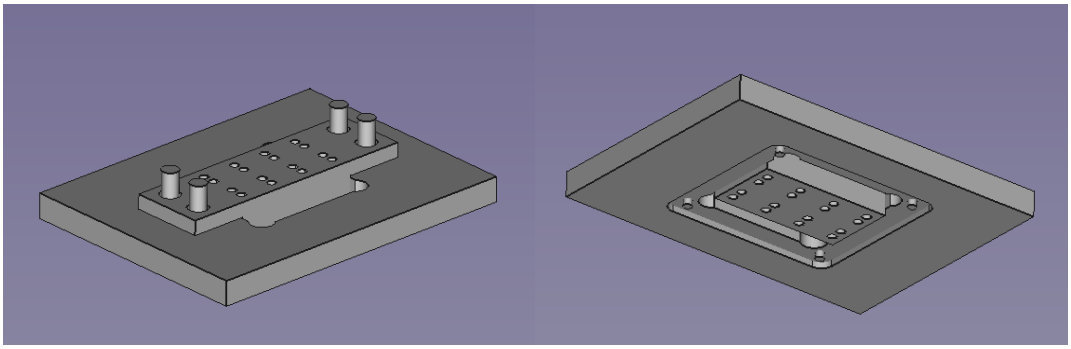

Figure SI2: Assembled 3D image of the chip holder consisting of a frame and an optic block. (A) Top view with optic block, (B) Bottom view with the pocket for the chip visible.

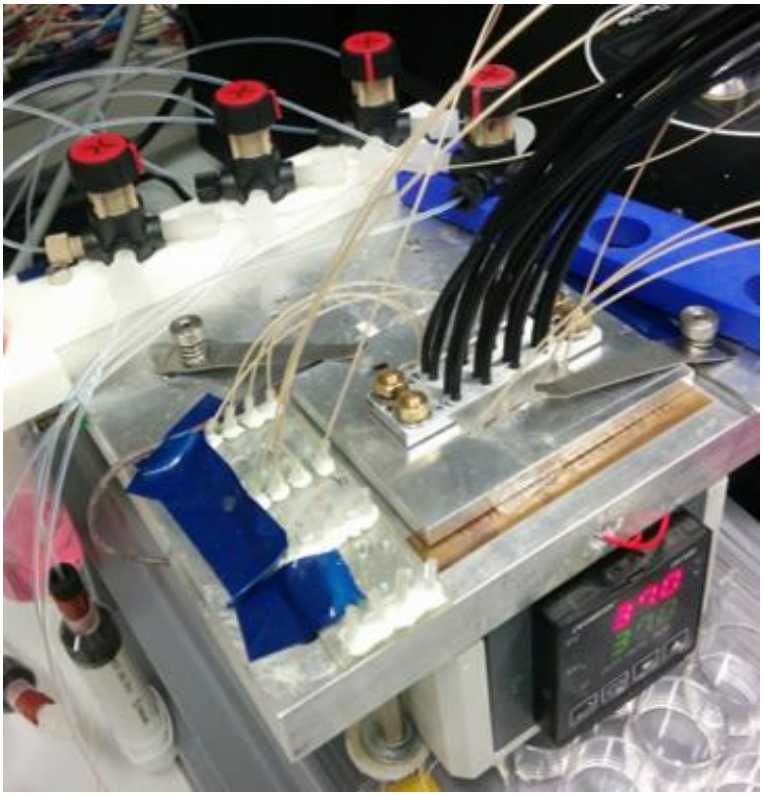

Figure SI3: Assembled set-up on a heated plat form. The PEEK valves, tubing and the bubble trap are visible next to the chip holder with the optic block.

Table SI3: pH of the used buffers with the respective buffer substance

aimed pH	substance	adjusted pH at 37°C
4.5	Ac	4.56
5.5	Mes	5.62
6.5	Mes	6.51
7	Tris	7.06
7.5	Tris	7.52
8	Tris	8.18
9	Gly	8.95
10	Gly	10.01

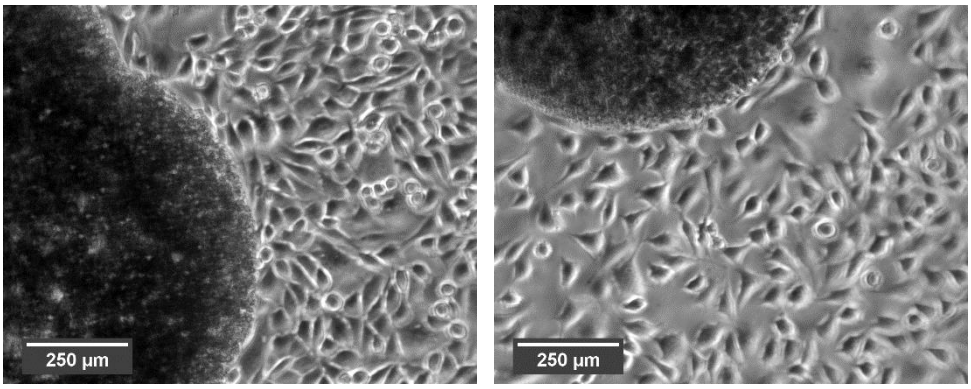

O_2 sensitive spot pH sensitive D4 spot

Figure SI4: Transmitted light microscope images of L929 (mouse fibroblastic cell line) on plasma treated PET support after 72h incubation

Part III

Resuts – pH Imaging of Concrete

4. High-resolution optical pH imaging of concrete exposed to chemically corrosive environments

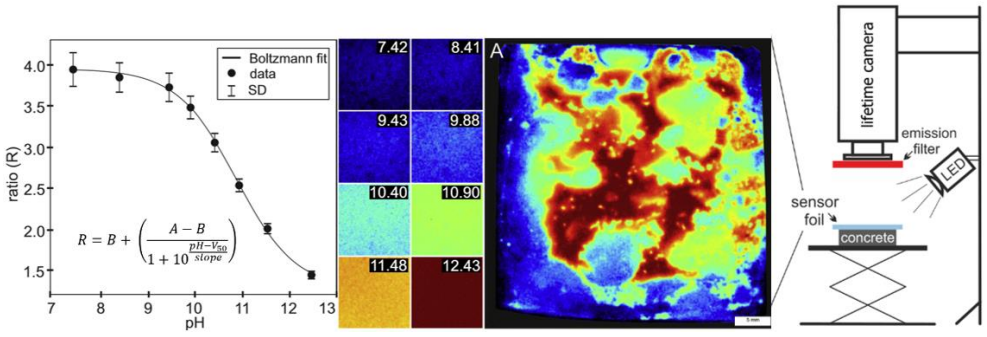

4.1. Preface for the Manuscript

This publication represents the first approach of a pH imaging method for concrete based construction materials. It was achieved due to a collaboration with the Institute of Applied Geosciences and the Institute of Technology and Testing of Building Materials, both located at Graz University of Technology. This cooperation started in fall 2017 when senior researcher Dr. Cyrill Grengg, who is working on strategies to prevent biogenic acid corrosion in concrete sewer systems, approached the Institute for Analytical Chemistry and Food Chemistry regarding new methods for pH measurement on concrete surfaces since existing method, like spray-coating with phenolphthalein or measurements with flat-surface glass-electrodes, lack sufficient spatial resolution or pH precision.

Concrete is a very alkaline environment starting with a pH as high as 12.8 for freshly cured samples. With ongoing deterioration process the pH of the material drops down to pH 8.8 for carbonation attacks or even as low as pH 2 for biogenic acid attacks. Until recently, there were barely any stable luminescent pH indicators for such high pH levels available and therefore basically no research has been done utilizing luminescent sensors in this area before. With the introduction of aza-BODIPY based pH indicators with high apparent pKa values by our group (Staudinger et al.) this field of application became available.

By combining these new indicators with traditional imaging methods from environmental science and biochemistry the measurement method described in this publication was developed. It utilizes the luminescence decay time as a measurement parameter to enable dual lifetime referencing in the time-domain for stable read-out and minimal background interference. For this technique a phosphorescent reference dye with similar spectral properties and a fast gate-able camera for image acquisition is deployed. Establishing the measurement method described in this publication, the ground for further prosperous collaborations between the involved institutes has been laid.

High-resolution optical pH imaging of concrete exposed to chemically corrosive environments

This manuscript was published as *Full Paper* in

Cement and Concrete Research Volume 116, February 2019, Pages 231-237.

doi: 10.1016/j.cemconres.2018.10.027

Authors: Cyrill Grengg[a*] & Bernhard Mueller[b*], Christoph Staudinger[b], Florian Mittermayr[c], Johanna Breininger[b], Birgit Ungerböck[b], Sergey Borisov[b], Torsten Mayr[b] & Martin Dietzel[a]

[a] Institute of Applied Geosciences, Graz University of Technology, Rechbauerstraße 12, 8010 Graz, Austria

[b] Institute of Analytical Chemistry and Food Chemistry, Graz University of Technology, Stremayrgasse 9, 8010 Graz, Austria

[c] Institute of Technology and Testing of Building Materials, Graz University of Technology, Inffeldgasse 24, 8010 Graz, Austria

*both authors contributed equally to this work

Corresponding author: cyrill.grengg@tugraz.at

Keywords: pH, image analyses, carbonation, corrosion, durability

4.2. Abstract

Major types of chemical concrete degradation such as carbonation, leaching and acid attacks are strongly associated with decreasing internal, surface and/or external pH. Thus, a precise pH determination is crucial for the assessment regarding the degree of corrosion and corresponding development of prevention strategies. Conventional pH measurement methods for concrete, such as pH visualization via color change of phenolphthalein indicator, pH analyses of extracted pore solutions and surface pH characterizations using flat surface electrodes have proven to hold significant limitations and inadequacies. This contribution presents the application of sensor foils based on luminescent, pH sensitive dyes for quantification and imaging of the spatial distribution of surface pH of concrete within a pH range between 9.35 and 12.35. For this purpose, an imaging technique called time-domain dual lifetime referencing (t-DLR) was used. High-resolution pH images of concrete samples exposed to carbonation and biogenic acid corrosion were successfully recorded and consequently compared to the state-of-the-art methods for pH assessment on concrete-based construction materials.

4.3. Introduction

The time resolved development of internal and surface pH of construction materials is a central parameter to determine the state of repair and durability of concrete structures. The pH level of pore fluids, considering ordinary Portland cement-based concretes, is mostly controlled by the content of alkali metals, the addition of supplementary cementitious materials (SCMs) and curing conditions [1,2]. Thereby, the pH of fresh concrete is usually around 13 [3]. Major types of chemical concrete degradation such as carbonation and acid attacks are associated with decreasing external, surface and internal pH. During these destructive processes, changes in pH are controlled by concrete - environment interactions, such as penetration of chemically aggressive solutions or diffusion of harmful gases, and consequent alteration of chemical and mineralogical concrete properties. In this context an accurate assessment and understanding of the pH development over time is crucial for a holistic process understanding of the different corrosion mechanisms and associated development of sustainable concrete-based infrastructure. The state-of-the-art methods for pH assessment in hardened concrete have recently been summarized by Behnood et al. (2015), subcategorizing destructive and non-destructive approaches [4]. While destructive methods are centered around expression of interstitial concrete pore fluids and leaching methodologies, non-destructive research focuses on the development of embedded sensors, such as potentiometric electrodes and fiber optic sensors [5–7]. At the same time, limited methods exist for the measurement of the spatially resolved distribution of pH in concrete structures.

Since concrete is a multicomponent, porous material, pH change over time proceeds mostly non-linear [3]. Thereby, the change in pH is strongly governed by the mineralogical heterogeneities within the concrete microstructure and differences in porosity controlling the diffusion of corrosive dissolved components and gases [8,9]. In order to characterize this non-linear pH change during different concrete alteration processes, proper imaging techniques of the latter are required. To date, methodologies for measuring spatial pH distribution on concrete are limited, although being crucial for the understanding of pH dependent degradation. In this context, the state-of–the-art is centered on the applications of indicator dyes, such as phenolphthalein (PHPHT). This concept relies on a change of the absorption properties of PHPHT at distinct pH (color change), and subsequent pH classification of the soaked concrete regions into areas of higher and lower pH, in respect to the known pKa value [10]. Advantages of pH indicator dyes are their simple application, quick analytical output and cost efficiency. At the same time, detailed information on pH distribution cannot be achieved and the system is not referenced. Moreover, PHPHT is known to have carcinogenic effects and its widespread use should be avoided [11]. Recently, Liu et al. (2017) introduced a concept for optical imaging of strongly alkaline pH levels (11.0-13.5) utilizing a halochromic porphyrin dye (TFPLPt) [12]. Therein, dissolved TFPLPt molecules were applied on newly fractured concrete and mortar samples. The pH images were obtained using a digital single lens camera, a white light source and two optical filters. Prior to the measurement, the diagnostic absorption bands were characterized in solutions (simulated concrete pore solution + TFPLPt and PHPHT) of various pH levels via transmittance spectroscopy. This set-up allowed the first mapping

of pH distribution on strongly alkaline concrete surfaces, thereby increasing the understanding of chemical concrete degradation mechanisms at early (high alkaline) stages.

Nevertheless, highly relevant aspects of pH measurements on concrete structures, such as time dependency, impact of ionic strength, reproducibility, scattering of the background and light in homogeneities (in the case of imaging techniques) remain ambiguous. Additionally, to date, no imaging technique exists, that is covering a wider pH range.

Herein we present a method for high-resolution surface pH imaging, demonstrated on concrete samples pre-exposed to accelerated carbonation and biogenic acid corrosion. The pH imaging set-up was realized by utilizing time-domain dual lifetime referencing (t-DLR) [13]. Therefore, a fluorescent pH indicator dye (short lifetime, nanoseconds (ns)) is combined with a phosphorescent reference pigment (long lifetime, microseconds (µs)) with similar spectral properties. Both dyes are excitable with red light and emit in the near infrared part of the electromagnetic spectrum. Ratiometric pH images of concrete surfaces were gained by dividing an image containing the input of both dyes (fluorescence and phosphorescence) against one containing only the input of the reference dye (phosphorescence). Using this technique, we show its high potential for pH quantifications by critically discussing the scientific background and methodology, together with an in-depth discussion on decisive aspects of common surface pH measurements of concrete samples.

4.4. Methods

4.4.1. Concrete

The concrete used for this study was a C55/67 (exposition classes: XC4/XD2/XF3/XA2L/XA2T) according to ÖNORM B4710-1 (Concrete - Part 1: Specification, production, use and verification of conformity. Rules for the implementation of EN 206 for normal and heavy concrete). This concrete was fabricated with a CEM I 42.5 R SR0 (EN 197-1), a w/c ratios of 0.43, predominantly siliceous aggregates (maximum size 16 mm) and about 4 % of entrained air. 15x15x15 cm3 cubes were casted and cured according to ÖNORM B4710-1. The 28d compressive strength was 84 N/mm2. For the experiments, 4x4x7.5 cm3 concrete specimens were cut out of a cube with an angle grinder before exposing them to two different chemically aggressive conditions.

One specimen was treated in a CO2 climatic chamber at 20 °C, relative humidity (r.h.) of 65 % and a CO2 concentration of 2 % for 30 days [14]. Thereafter, fresh cross-section areas were produced by cutting the specimens with an angle grinder. In order to prevent further surface pH alterations, samples were stored in a desiccator under nitrogen atmosphere.

Another specimen was cut into several 4x4x1 cm3 slices before outsourcing them for 30 days into a sewer system, strongly affected by biogenic acid corrosion. Therein, prevailing environmental

conditions comprised r.h. levels of between 80 and 100 % and high concentrations of hydrogen sulfide (H2S) (average of 34 ppm; peak levels of 350 ppm) and CO2 (1000 to 6200 ppm). A detailed characterization of the exposure system is given elsewhere [15,16]. After sample collection, concrete specimens were dried at 40 °C for 24 h. In order to prevent further surface pH alterations, samples were stored in a desiccator under nitrogen atmosphere.

4.4.2. Sensor material

The dye class of aza-BODIPYS is well known for their stability, their good near infrared emission and tunable pKa value [17]. The recently developed aza-BODIPY dye (Figure 1B) from Staudinger et al. [18] features a rather high apparent pKa value of 10.8 in a polyurethane hydrogel, which makes it suitable for the envisaged application. The dye can be excited from 600 nm to 720 nm, with its maximum absorption being at 696 nm, while emitting from 670 nm to 850 nm, with its maximal emission at 722 nm (Figure 1C). Egyptian Blue, a calcium copper silicate [19], was used as a reference for the t-DLR system. Egyptian Blue is a ceramic bulk material that exhibits excellent chemical and photochemical stability and shows near-infrared emission from around 800 nm to 1100 nm. It can be excited from 500 nm to 700 nm and exhibits no cross-sensitivity to oxygen. Both components were dissolved/suspended in an 8 wt.% polymer solution of a polyurethane hydrogel (HydroMed D4 from Advanced Biomaterials) in tetrahydrofuran/water (9+1). The sensor formulation was homogenized with a Sonifier W-450 D from Branson. The concentration of aza-BODIPY and Egyptian Blue in the solvent-free sensor material was 0.2 wt.% and 33.3 wt.%, respectively. The sensor formulation was knife coated on a 125 µm thick PET foil from DuPont Teijin Films (Melinex 506), using a 3x10-3 in (76 µm) wet film knife from Byke. Since the nonvolatile compounds represent 11.54 % of the sensor formulation, the thickness of the dry sensor film was approximately 8.7 µm. Due to a water uptake of 50 % of the hydrogel D4 matrix the sensor film has an estimated thickness of 13.2 µm in the wet state. A schematic representation of the senor film is shown in figure 1A. For measurements, the sensor foil was cut into a 4x4 cm square in order to fit the concrete samples, and stored in deionized water.

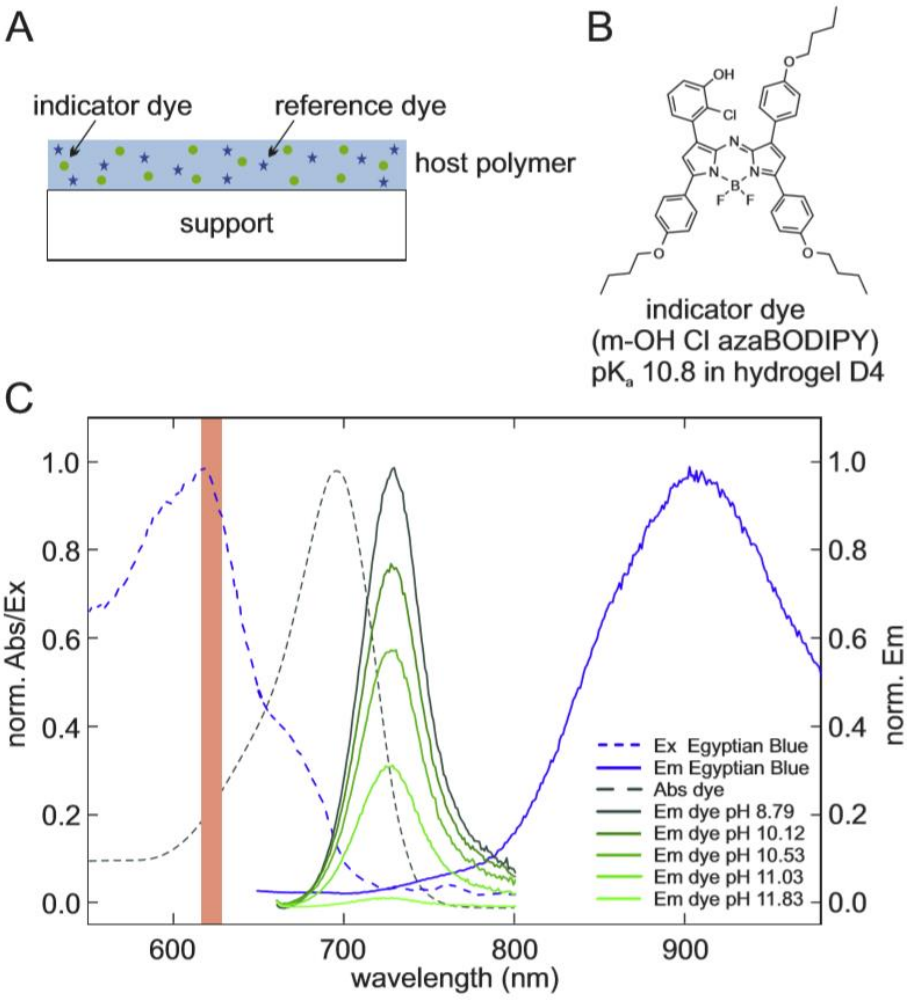

Figure 1: (A) Schematic drawing of the sensor foil composition; (B) Chemical structure of the used pH indicator dye; (C) Absorption/excitation and emission spectra of indicator dye and reference phosphor. The emission of the indicator dye is shown for different pH values; the used excitation wavelength of the sensor system is represented by the red bar at 625 nm.

For excitation a power LED array LR CP7P from OSRAM Opto Semiconductors GmbH, with a mean emission wavelength of 625 nm, was used. It was operated at a constant current of 200 mA, provided by the DC power supply DF1730SL from Ningbo Jinyaun (G.S) Electricity Co. In order to generate constant light pulses, a pre-resistor with 3.9 Ω was used. A RG9 emission filter from Schott, transmitting wavelengths from 700 - 1000 nm, was placed in front of the time-gateable SensiCam from PCO AG equipped with a PENTAX TV lens 12 mm for collecting images. The time coordination between these two devices was realized by a trigger box from Biocam GmbH. A schematic view of the imaging set-up is presented in Figure 2.

The surface pH of concrete samples was imaged by placing the wet, calibrated sensor foil onto the samples. Air pockets were eliminated by striking gently across the foil and two consecutive pictures were taken every 5 seconds to track the sensor response. The first was recorded during the excitation phase (window 1; “light-on”), where both dyes contribute to the image and the second one right after the excitation (window 2; “light-off”), where only the reference phosphor is emitting (Figure 2). The timeframes of each measurement were optimized in a way, so that window 2 showed

sufficient signal intensity under alkaline conditions (phosphorescence only) and window 1 was not saturated under acidic conditions (fluorescence + phosphorescence). This optimization led to a window length of 20 µs for both pictures each and an excitation phase of 100 µs. The images were taken 80 µs and 101 µs after the start of the excitation phase. To gain sufficient signal intensity an integration time of 500 ms was used in which the entire recording process was repeated constantly. The "light-on" and the "light-off" images were divided through each other utilizing a python script to gain the ratiometric image, which was recalculated with the corresponding calibration function into a pH image.

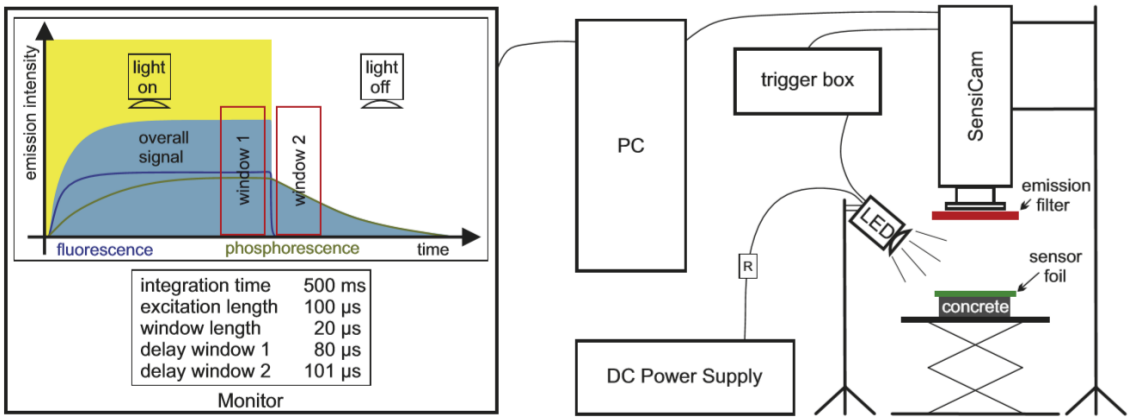

Figure 2: Schematic illustration of the imaging setup. Constant light pulses were obtained using a power LED operated by the DC power supply equipped with a pre-resistor (R). NIR images of pH distribution of concrete samples were taken using a SensiCam adopted with an upstream RG9 emission filter. Two consecutive images (windows 1 and 2) were recorded utilizing a trigger box for timing. Window 1 was taken during the excitation phase (light on) and captures the emission signals of the indicator and the reference dye (fluorescence and phosphorescence signal). Window 2 was taken after the excitation (light off), therefore only containing the long living phosphorescence signal of the reference phosphor.

4.4.3. Calibration

A rough assessment of the expected ionic strength (IS) of the supernatant water used for the measurement was done by applying three different amounts (150 µL, 300 µL and 400 µL) of distilled water on three different concrete surfaces. After an equilibration time of 30 and 60 seconds respectively, the residual water film was collected. After dilution to 2.5 mL the electrical conductivity (EC) was measured using a WTW Multi350i instrument equipped with a TetraCon325 electrode and recalculated into ionic strength following Equation 1 [20]:

$$IS\left(\frac{mol}{L}\right) = 1.6 \cdot 10^{-5} \cdot EC\left(\frac{\mu S}{cm}\right) \qquad \textbf{Equation 1}$$

Based on the average ionic strength of the supernatant, the sensor foil was calibrated using 10 mM Goods buffer (TRIS, CHES, CAPS). The ionic strength of the buffer solutions was adjusted with NaCl to 10 mM. The exact pH of the buffer solutions was adjusted using NaOH or HCl, respectively. For each calibration point the sensor foil was soaked in the buffer solution with the adjusted pH,

placed on a black background and pictures were taken as described in 2.3. The mean ratiometric values of representative areas of interest (roughly 2x2 cm) were plotted against the respective pH values and fitted using the Boltzmann equation (Equation 2) to generate the calibration function:

$$R = B + \left(\frac{A - B}{1 + 10^{\frac{pH - V_{50}}{slope}}} \right) \qquad \textbf{Equation 2}$$

Where R represents the ratio, A the top value, B the bottom value, pH the pH value, V50 the point of inflection and slope the slope in the point of inflection of the Boltzmann function.

4.4.4. Background check

The influence of the background was evaluated by taking images of the sensor foil soaked in moderate (pH <9.35) and alkaline (pH >12.35) buffer solutions. The foil was placed on a concrete specimen wrapped in a cling film in order to avoid interaction of the sensor material with the concrete. The pH images were taken with the same settings as described in 2.3.

4.4.5. Reference pH measurement

On each concrete specimen, four to five reference pH measurements, randomly distributed at the surface, were conducted using an Extech PH100 flat surface electrode. For each measurement, one drop of ultrapure water was applied on the concrete surface. The electrode was placed on the wetted surface and measurements were taken when stabilization of the pH was reached (roughly after 20 to 30 s).

4.5. Results and Discussion

4.5.1. Ionic strength measurements & sensor calibration

The approximate ionic strength of the fluids applied on concrete surfaces was 14 mmol L^{-1} (Table 1). This surprisingly low value shows that over a realistic measurement time only a small amount of solids dissolve. A prior check of the ionic strength is central since pH measurements (potentiometric and optical) are prone to errors at low salinities if not addressed correctly during calibration. Accordingly, such considerations have also been taken into account when using state-of-the-art pH electrodes (e.g. flat surface electrodes).

Table 1: Estimation of ionicstrength[a]

ID	Volume (µL)	Exposure time (s)	EC (µS cm^{-1})	Ionic strength (mmol L^{-1})
1	400	30	740	11.84
2	300	60	893	14.29
3	150	30	986	15.78

[a] using electrical conductivity measurements of three different volumes of supernatant after 30 and 60 second exposure time on concrete surfaces.

For the sake of simplicity, the sensor materials used in this study contained only one aza-BODIPY dye limiting the sensitive range to roughly three pH units. Nevertheless, due to their photochemical and spectral similarities mixing of multiple aza-BODIPY dyes with different pKa values is possible. This is expected to result in extension of the pH sensitive range as shown by Strobl et al. (2015) for a pH sensor with extended dynamic range from pH 2 - 9 [17]. Using the pH indicators reported by Staudinger et al. (2018) a sensor covering pH range from 6 to 13 is feasible [18].

The sensor foil was calibrated using the Boltzmann equation (Equation 2) as fitting function (Figure 3). The resulting Boltzmann sigmoid has its point of inflection (V50) at a pH value of 10.84, representing the apparent pKa value of the sensor foil. As expected, this matches closely the reported apparent pKa value of the aza-BODIPY dye in hydrogel D4 with an apparent pKa of 10.8, estimated from fluorescence intensity measurements [18]. The top value of the sigmoid (A) has a ratio of 3.95, whereas the bottom value (B) shows a ratio of 1.27. The sensitivity of this sensor foil within its linear range is defined by its slope at the inflection point (slope) with a change in ratio of 1.42 per pH unit. As described above, the linear range of this sensor system, utilizing a single indicator dye is roughly ±1.5 pH units around the apparent pKa, resulting in a sensitive range for this sensor foil from pH 9.35 to pH 12.35. Therefore, for image processing only this range was visualized to analyze the pH distribution of the concrete specimens with high resolution.

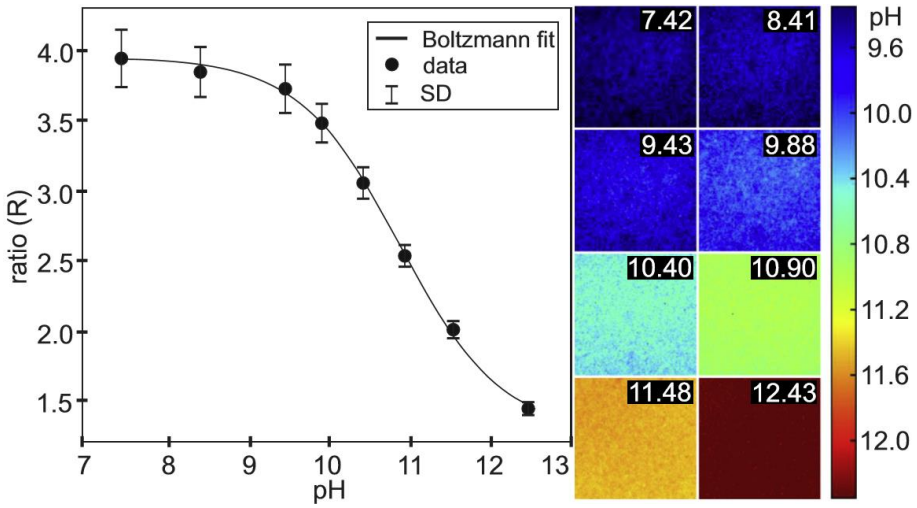

Figure 3: Calibration curve of the sensor foil obtained with a Boltzmann fit. The analyzed areas of interest are shown together with the respective pH value. The sensitivity of this sensor foil within its linear range is defined by its slope at the inflection point (corresponding pKa of 10.84) with a change in ratio of 1.42 per pH unit. Standard deviations (SD) of the areas are given.

4.5.2. pH imaging of chemically altered concrete surface

In order to provide prove of concept, pH imaging measurements were performed on concrete specimens strongly affected by different types of chemical alteration mechanisms. Concrete specimens were used after pre-exposure to accelerated carbonation and biogenic acid corrosion. High-resolution surface pH images of cross sections from concrete specimen were obtained after one minute (see response time mentioned above) and subsequently compared to spot pH measurements of the same concrete surfaces, conducted by flat surface electrode (Figure 4 and 5).

Obviously, the imaging technique allows detailed visualization of pH gradients along the concrete surface, demonstrating a high spatial resolution in the pH range from 9.35 to 12.35.

Images of concrete samples, which were pre-exposed to carbonation, show an inhomogeneous, gradual decrease of the pH from the cementitious matrix of rim areas, corresponding to progressive carbonation, while a generally high pH remains within the core areas (Figure 4A). Additionally, strong microscale pH variations within the core regions were obtained, which can be clearly attributed to the heterogenic mineralogy of the concrete specimens. For instance, a sharp drop in pH from >12.3 to around 10.0 is clearly visible between the strongly alkaline cementitious matrix and the silicate aggregates (Figure 4C). These details were obviously not resolved using the flat surface pH electrode (Figure 4C). However, the spot measurements of the pH using the flat surface electrode are in good agreement with the overall pH distributions obtained with the novel t-DLR imaging technique. In this context, spot analysis using the flat surface electrode corresponds approximately to a mean pH of the concrete surface within the size of the cross section of the electrode (~8 mm). Thus, pH gradients and variations cannot be resolved at a sub-centimeter level using the latter.

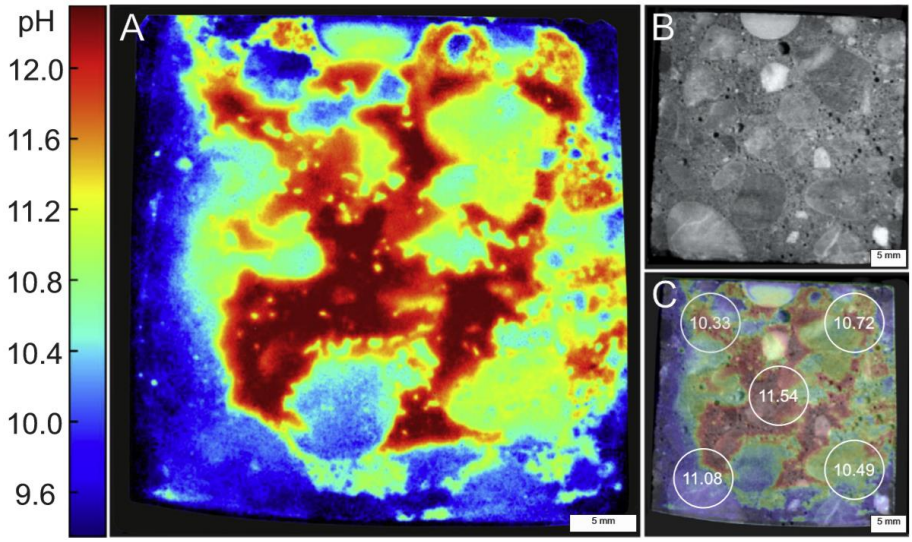

Figure 4: Concrete specimen previously exposed to accelerated carbonation. (A) pH image of the sample recorded with t-DLR imaging. (B) Image of the concrete surface used for pH imaging. (C) Combined image of A and B including reference pH measurements using a flat surface electrode.

Images taken of concrete surfaces exposed to biogenic acid corrosion showed an overall lower pH compared to samples pre-exposed to carbonation (Figure 5). No sharp pH transitions are visible between the cementitious matrix and the silicate aggregates using t-DLR imaging. The reasons therefore are uniform biogenic influences and corresponding surficial biofilm development, as well as secondary surficial mineral precipitations, such as elemental sulfur. Both of these processes are indicative for biogenic acid corrosion on concrete [15,21–24]. The additional decrease in pH within the rim areas can be explained by predated atmospheric carbonation of the concrete specimens, prior to the sample preparation and slicing. Therefore, pH distributions obtained on the latter samples can be allocated to a combination of carbonation and subsequent alteration due to biogenic acids. Reference measurements with the flat surface pH electrode confirmed the pH values obtained via imaging, although as mentioned above not being able to reach detailed spatial resolution. It is apparent that the t-DLR imaging technique exhibits high potential for adding knowledge regarding the understanding of chemical and mineralogical processes responsible for the corrosion of concrete materials.

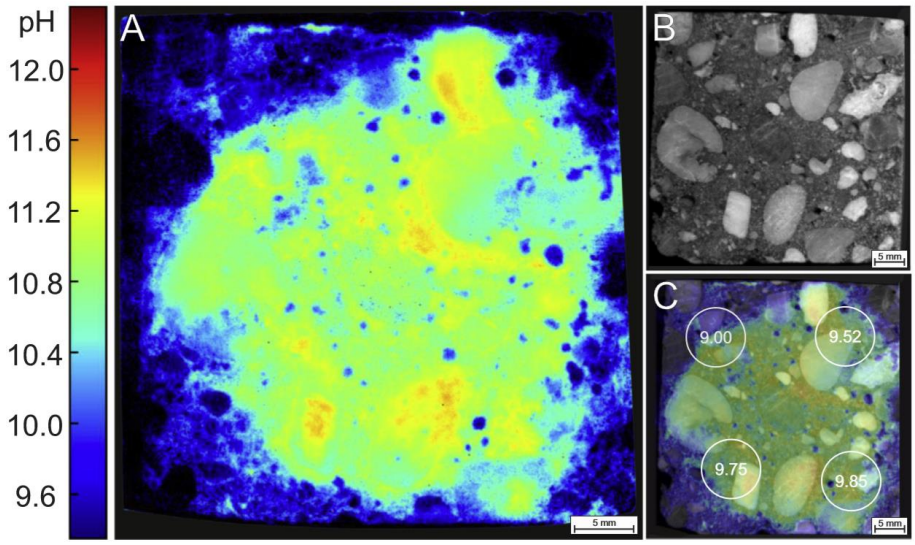

Figure 5: Concrete specimen previously exposed to a biogenic acid corrosive environment. (A) pH image of the sample recorded with t-DLR imaging. (B) Image of the concrete surface used for pH imaging. (C) Combined image of A and B including reference pH measurements using a flat surface electrode.

4.5.3. Time dependency, reproducibility & background scattering

Since the pH value is defined in an aqueous environment all solid surfaces have to be wetted in order to measure the latter. In the case of porous materials, the determination of the surface pH is therefore inevitably difficult, since diffusion of substances (e.g. from inner regions to the surface) cannot be avoided. The response time of a given sensor is therefore a central aspect. To address this issue, images were taken every 5 seconds for a period of 150 seconds and the pH response was tracked in low and high pH areas of the sample, in respect to the sensor sensibility range. Figure 6 shows the development of the surface pH over time. After approximately 60 seconds, a stable pH

was reached in the alkaline region. However, a slight ongoing drift can be observed which is caused by lateral and horizontal diffusion processes leading to blurry images and a generally higher pH values over time.

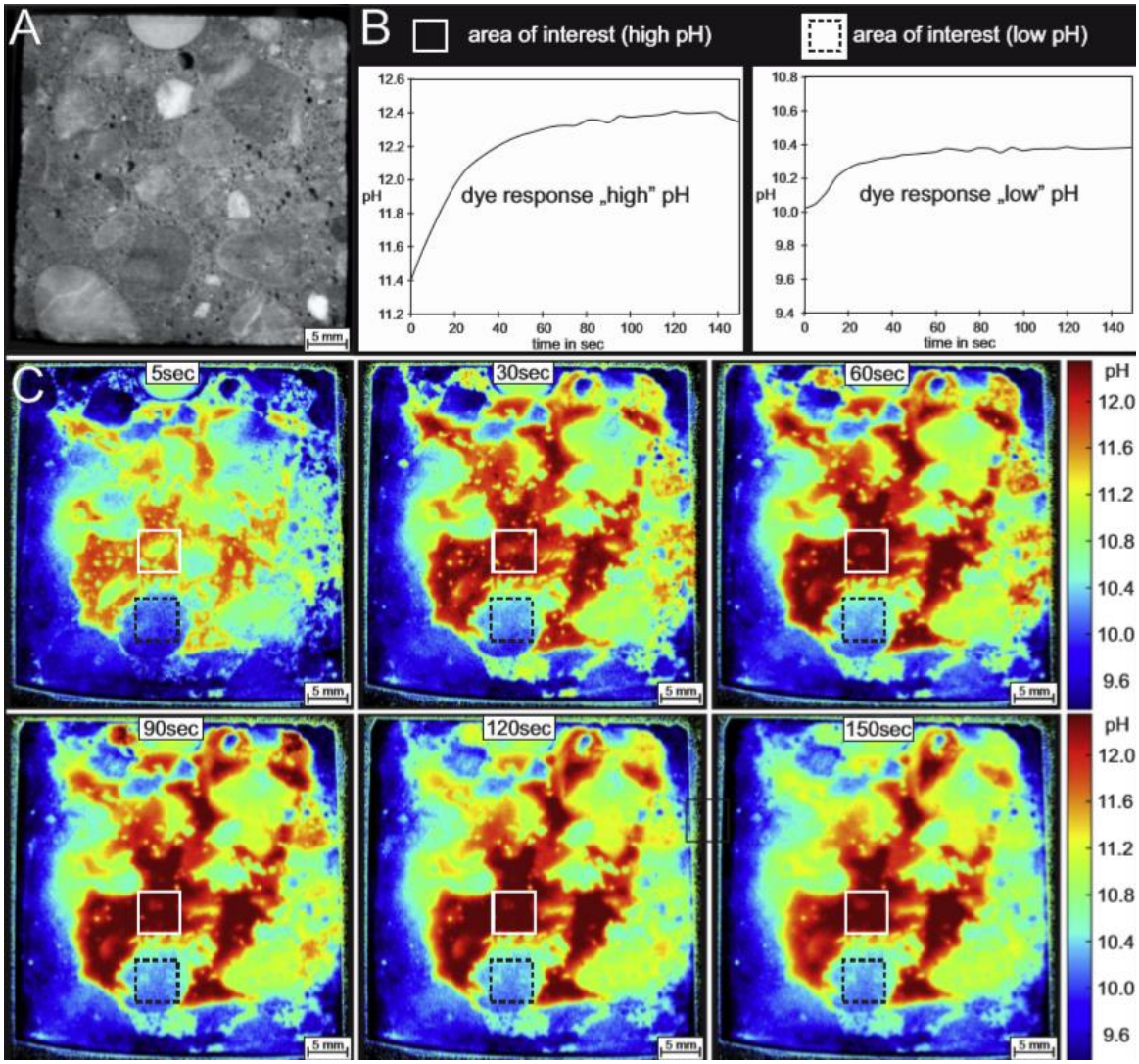

Figure 6: pH response over time of a concrete specimen previously exposed to accelerated carbonation conditions with t-DLR imaging. (A) Image of the sample. (B) pH response of selected areas of interest for regions with low and high pH. (C) Representative images of the measurement development over time.

Keeping this in mind, it is apparent that any measurement influences the surface pH of a sample. In order to determine the degree of influence two consecutive measurements were performed on the same concrete surface previously exposed to a biogenic acid corrosive environment. In between the measurements, a period of 3 minutes was kept in order to allow the drying of the surface. Between the first set of images and the second set, a maximum drift of 0.2 pH units in the center (worst case) was visible (Figure A2). However, the overall pH information of the image remained the same.

Scattering, reflection and absorption effects are generally challenging for all imaging techniques, and referencing strategies or optical insulations are needed to suppress them. The t-DLR system

presented here utilizes Egyptian Blue as an inert reference. The robustness of this system is shown in Figure 7. Under alkaline conditions, the background is very homogenous and only slight light inhomogeneities are visible. Under low pH conditions (for this sensor <9.35), the background is not totally compensated and silicate aggregates are slightly visible. This is probably due to different scattering of the emission light on the brighter surface, which is dissimilar for both used dyes, since the emission spectra do not overlap perfectly. The reason for the better homogeneity at high pH conditions can be explained by the low contribution of the indicator dye to the overall signal at such conditions. Thus, different scattering of the emission light shows minor effects. This discrepancy can be improved by applying an additional optical insulation layer or by using a reference dye, which has a more similar emission.

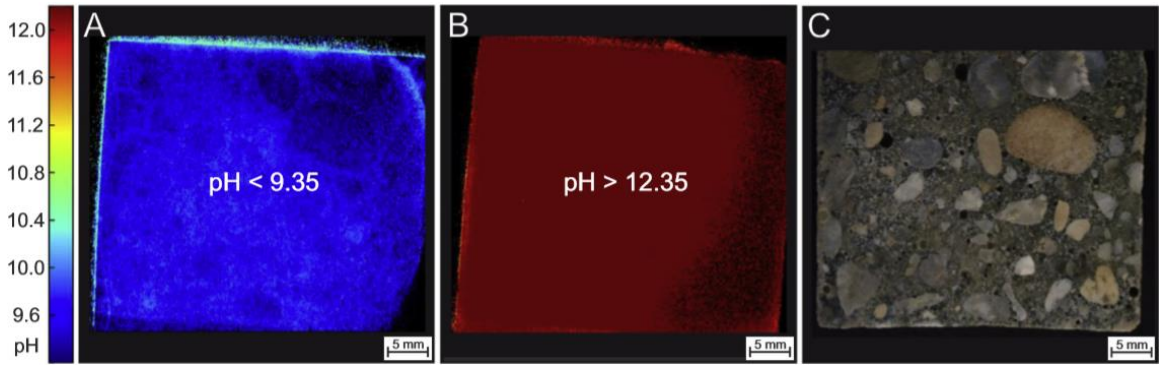

Figure 7: t-DLR images of sensor foil soaked in acidic (A) and alkaline (B) buffers recorded while placed on a concrete sample (C) to check for inhomogeneities due to the background.

4.6. Conclusion and Outlook

The aim of this study was to explore the t-DLR method as an imaging technique for pH measurements on concrete in order to gain a better understanding of ongoing processes and to critically discuss state-of-the-art measurements, such as flat surface electrodes and PHPHT staining. The results clearly demonstrate the potential of the t-DLR based imaging technique to obtain high-resolution spatial pH information, irrespectively of the type of chemical deterioration mechanisms and the exposed environments. Furthermore, the set-up described can significantly contribute towards an advanced understanding in respect to crucial unanswered questions regarding the impact of diffusion (horizontally and vertically) driven pH drifts during measurements and the impact of porosity and material heterogeneities.

Challenges, such as the imperfect background compensation under low pH conditions, can be tackled by using optical insulation layers based on TiO_2 and carbon black in the future.

Further developments will cover the combination of several aza-BODIPY dyes in order to extend the linear pH range of the sensor and facilitate broadband pH applications. As mentioned before,

aza-BODIBY dyes show similar spectral properties and their pKa value can be tuned over a wide range (pH 2.6 to pH 11.9). Since Strobl et al. (2015) showed a broad-range pH sensor (pH 2 to pH 9), a similar imaging system can be achieved [17].

This will especially provide important insights for different types of acid attacks on concrete, such as the presented biogenic induced acid corrosion.

The current resolution of around 75 µm per pixel can be further tuned with appropriate optical equipment. The limiting factor for close-up images using this system is the particle size of the reference compound with around 5 µm. Additionally, the fabrication of sensor particles for sprayed applications instead of sensor foils, to tackle the challenge of measuring on uneven surfaces, would allow an even wider range of applications and simplify the method for field application.

We therefore conclude that the t-DLR pH imaging set-up provides a viable and highly promising tool for gaining a deeper knowledge about ongoing destructive surface processes of heterogenic, porous concrete samples.

Acknowledgements

The authors thank Helmar Wiltsche, Lukas Troi, Joachim Juhart, and Vasileios Mavromatis for fruitful discussions and Tobias Eder for help regarding sample preparation and laboratory work.

4.7. References

[1] G. Plusquellec, M.R. Geiker, J. Lindgård, J. Duchesne, B. Fournier, K. De Weerdt, Determination of the pH and the free alkali metal content in the pore solution of concrete: Review and experimental comparison, Cem. Concr. Res. 96 (2017) 13–26. doi:10.1016/j.cemconres.2017.03.002.

[2] Q. Pu, L. Jiang, J. Xu, H. Chu, Y. Xu, Y. Zhang, Evolution of pH and chemical composition of pore solution in carbonated concrete, Constr. Build. Mater. 28 (2012) 519–524. doi:10.1016/j.conbuildmat.2011.09.006.

[3] M. Alexander, A. Bertron, N. De Belie, Performance of Cement-Based Materials in Aggressive Aqueous Environments, 1st ed., Springer, Ghent, 2013. doi:10.1007/978-94-007-5413-3.

[4] A. Behnood, K. Van Tittelboom, N. De Belie, Methods for measuring pH in concrete: A review, Constr. Build. Mater. 105 (2016) 176–188. doi:10.1016/j.conbuildmat.2015.12.032.

[5] A. Safavi, M. Bagheri, Novel optical pH sensor for high and low pH values, Sensors Actuators, B Chem. Actuators. 90 (2003) 143–150.

[6] K. Pásztor, A. Sekiguchi, N. Shimo, N. Kitamura, H. Masuhara, Iridium oxide-based microelectrochemical transistors for pH sensing, Sensors Actuators B. Chem. 12 (1993) 225–230. doi:10.1016/0925-4005(93)80023-5.

[7] O.S. Wolfbeis, Fiber-Optic Chemical Sensors and Biosensors, Anal. Chem. 76 (2004) 3269–3284. doi:10.1021/ac040049d.

[8] J. Stark, B. Wicht, Dauerhaf tigkeit von Beton, 2nd ed., Springer, 2013. doi:10.1007/978-3-642-35278-2.

[9] C.L. Page, M.M. Page, Durability of concrete and cement composites, CRC Press, 2007.

[10] L.J. Parrott, A Review of carbonation in reinforced concrete, Springer, Wexham Springs, Slough; Garston, Watford, 1987.

[11] J.R. Dunnick, June K. Hailey, Phenolphthalein Exposure Causes Multiple Carcinogenic Effects in Experimental Model Systems, Cancer Res. 56 (1996) 4922–4926. http://cancerres.aacrjournals.org/content/canres/56/21/4922.full.pdf.

[12] E. Liu, M. Ghandehari, C. Brückner, G. Khalil, J. Worlinsky, W. Jin, A. Sidelev, M.A. Hyland, Mapping high pH levels in hydrated calcium silicates, Cem. Concr. Res. 95 (2017) 232–239. doi:10.1016/j.cemconres.2017.02.001.

[13] C.R. Schröder, B.M. Weidgans, I. Klimant, pH Fluorosensors for use in marine systems, Analyst. 130 (2005) 907. doi:10.1039/b501306b.

[14] International Federation for Structural Concrete, Model Code for Service Life Design, Fib

Bull. 34 (2006) 116.

[15] C. Grengg, F. Mittermayr, a. Baldermann, M.E. Böttcher, a. Leis, G. Koraimann, P. Grunert, M. Dietzel, Microbiologically induced concrete corrosion: A case study from a combined sewer network, Cem. Concr. Res. 77 (2015) 16–25. doi:10.1016/j.cemconres.2015.06.011.

[16] C. Grengg, Microbial induced acid corrosion in sewer environments, PhD Thesis, Graz University of Technology, 2018.

[17] M. Strobl, T. Rappitsch, S.M. Borisov, T. Mayr, I. Klimant, NIR-emitting aza-BODIPY dyes – new building blocks for broad-range optical pH sensors, Analyst. 140 (2015) 7150–7153. doi:10.1039/C5AN01389E.

[18] C. Staudinger, J. Breininger, S. Borisov, I. Klimant, Aza-BODIPY based pH indicators with purely PET based quenching mechanism, Analyst. submitted (2018).

[19] S.M. Borisov, C. Würth, U. Resch-Genger, I. Klimant, New life of ancient pigments: Application in high-performance optical sensing materials, Anal. Chem. 85 (2013) 9371–9377. doi:10.1021/ac402275g.

[20] Y. Zeng, Colloidal Dispersions under Slit-Pore Confinement, Springer, 2012.

[21] C. Grengg, F. Mittermayr, N. Ukrainczyk, G. Koraimann, S. Kienesberger, M. Dietzel, Advances in concrete materials for sewer systems affected by microbial induced concrete corrosion: A review, Water Res. 134 (2018) 341–352. doi:10.1016/j.watres.2018.01.043.

[22] C. Grengg, F. Mittermayr, G. Koraimann, F. Konrad, M. Szabó, A. Demeny, M. Dietzel, The decisive role of acidophilic bacteria in concrete sewer networks: A new model for fast progressing microbial concrete corrosion, Cem. Concr. Res. (2017). doi:10.1016/j.cemconres.2017.08.020.

[23] M. Peyre-Lavigne, A. Bertron, C. Botanch, L. Auer, G. Hernandez-Raquet, A. Cockx, J.-N. Foussard, G. Escadeillas, E. Paul, Innovative approach to simulating the biodeterioration of industrial cementitious products in sewer environment. Part II: Validation on CAC and BFSC linings, Cem. Concr. Res. (2015). doi:10.1016/j.cemconres.2015.10.002.

[24] A. Grandclerc, M. Minerbe-Guéguen, I. Nour, P. Dangla, T. Chaussadent, Impact of cement composition on the adsorption of hydrogen sulphide and its subsequent oxidation onto cementitious material surfaces, Constr. Build. Mater. 152 (2017) 576–586. doi:10.1016/j.conbuildmat.2017.07.003.

4.8. Supporting Information

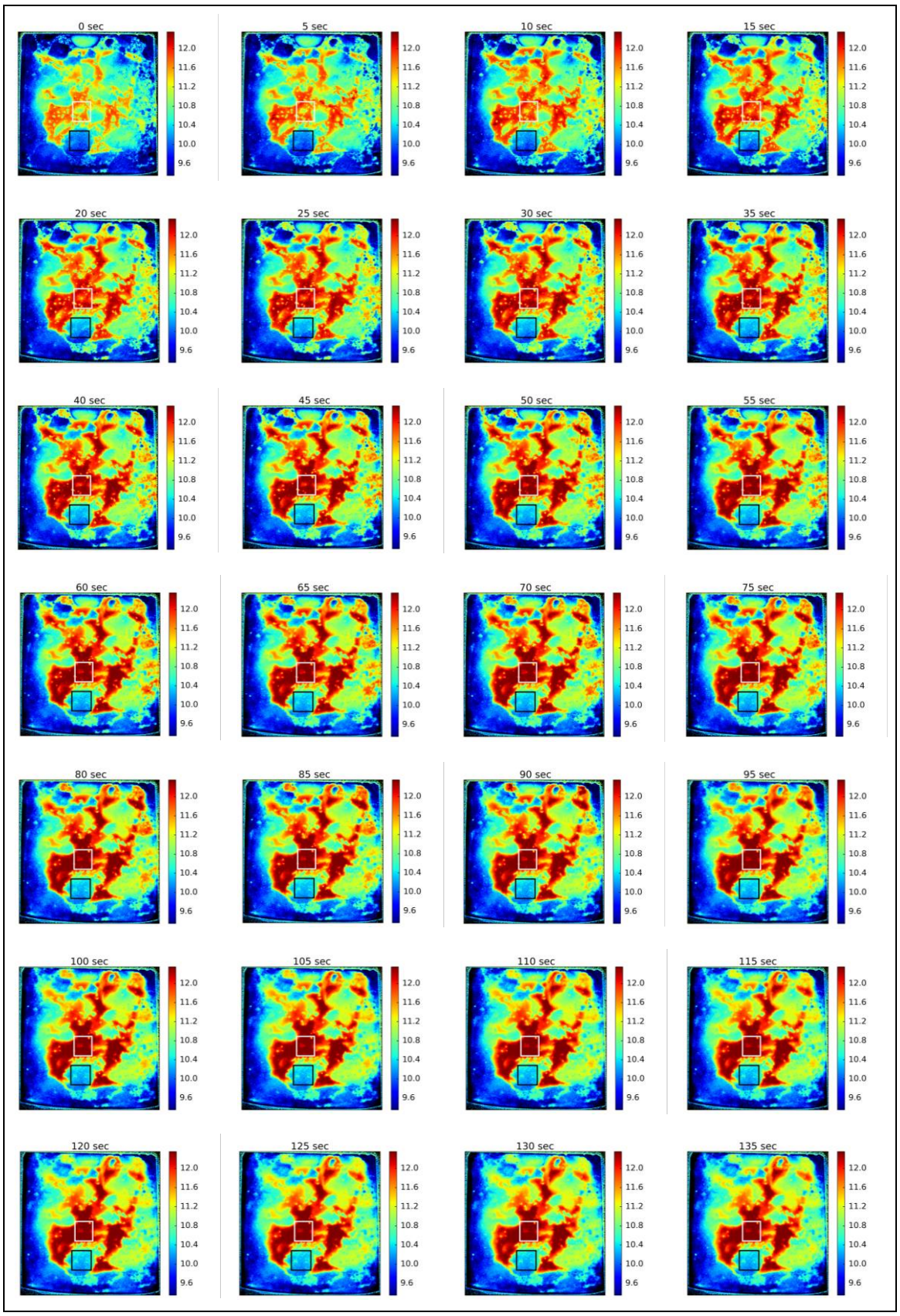

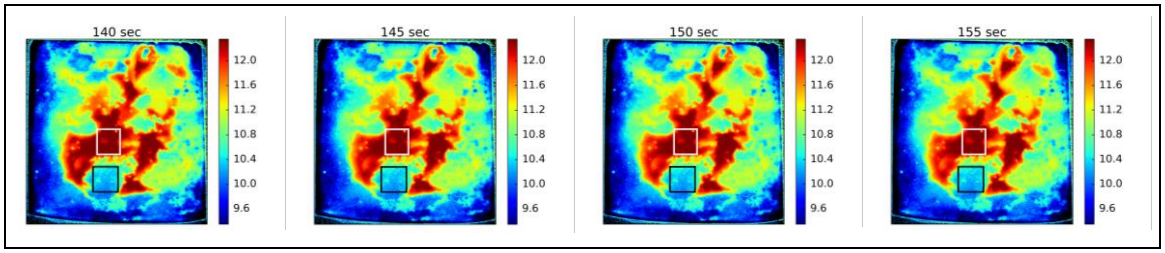

Figure A1: pH response over time of a concrete specimen previously exposed to accelerated carbonation conditions with t-DLR imaging. Pictures taken every 5 seconds

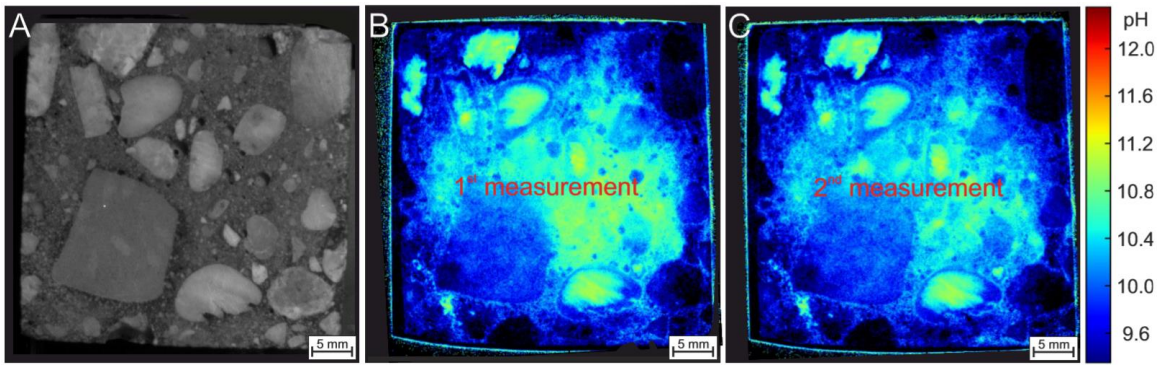

Figure A2: Reproducibility measurement of a concrete specimen previously exposed to a biogenic acid corrosive environment. (A) Image of the sample. (B) & (C) t-DLR images of the same sample recorded twice where the surface was allowed to dry in between.

5. Wide-range optical pH imaging of cementitious materials exposed to chemically corrosive environments

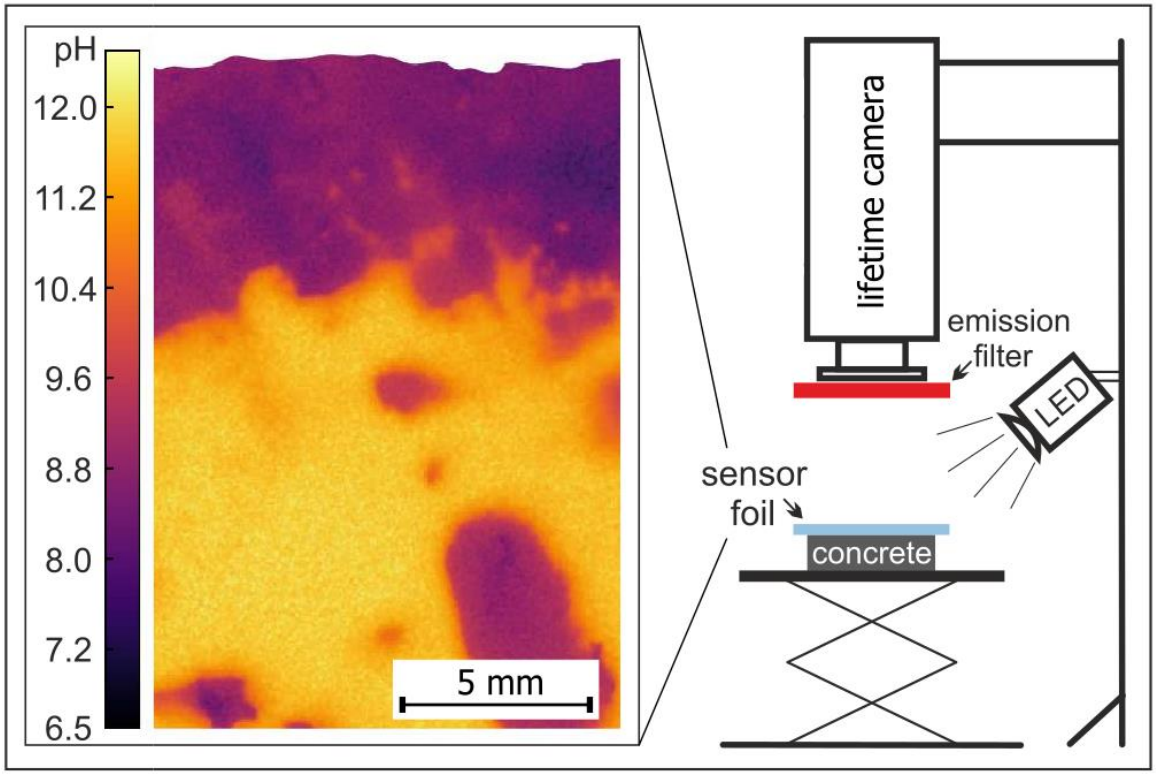

5.1. Preface for the Manuscript

This publication describes the improvements made on the pH imaging system for concrete-based materials after the previous report of this method. However, due to a long peer-reviewing process of the first publication in the CCR journal, this report was actually published slightly before the original one.

The same collaboration partners were involved in the reported improvements as for the first publication. The Institute of Applied Geosciences and the Institute of Technology and Testing of Building Materials supported the project with their knowledge which areas of concrete deterioration to focus on and provided concrete samples from ongoing research projects. The method was tested for different types of concrete, including classical Portland cement based B6 concrete, UHPC concrete and wet-mix shotcrete mixtures. The set-up was expanded to enable close-up images with a resolution of 35 µm per pixel with respect to the important role of transition zones in concrete deterioration processes. Further, the pH range of the sensor was improved by incorporation of two similar pH indicators with different sensitive areas in one sensor foil. Moreover, a new reference material was used. This material showed a better spectral match with the indicator dyes and provided a better optical insulation at the same time. Therefor it vastly improves the compensation of reflection and scattering effects of the inhomogeneous background.

With the improved pH imaging method, samples from other international cooperation partners were analyzed. However, these results are not part of in this publication. For example, samples form the work group of Prof. Alexandra Bertron (INSA Toulouse- Department of Civil Engineering) and from the workgroup of Prof. Ueli Angst (ETH Zürich- Department of Civil, Environmental and Geomatic Engineering) were investigated. Moreover, this imaging system resulted in the draft of a research proposal in cooperation with the ÖBV (Austrian society for construction technology), involving the Austrian infrastructure operators ÖBB and ASFiNAG. The proposal is currently under review by the Austrian Research Promotion Agency (FFG).

Wide-range optical pH imaging of cementitious materials exposed to chemically corrosive environments

This manuscript was published as *Full Paper* in

RILEM Technical Letters (2018) 3: 39-45

doi: 10.21809/rilemtechlett.2018.72

Authors: Bernhard Müller[a]*, Cyrill Grengg[b], Viktor Schallert[a], Marlene Sakoparnig[c], Christoph Staudinger[a], Johanna Breininger[a] Florian Mittermayr[c], Birgit Ungerböck[a], Sergey Borisov[a], Martin Dietzel[b] & Torsten Mayr[a]

[a] Institute of Analytical Chemistry and Food Chemistry, Graz University of Technology, Stremayrgasse 9, 8010 Graz, Austria

[b] Institute of Applied Geosciences, Graz University of Technology, Rechbauerstraße 12, 8010 Graz, Austria

[c] Institute of Technology and Testing of Building Materials, Graz University of Technology, Inffeldgasse 24, 8010 Graz, Austria

***Corresponding author:** bernhard.mueller@tugraz.at

Keywords: optical pH sensors; surface pH; pH-sensitive dyes; concrete carbonation; bio-corrosion

5.2. Abstract

The pH of concrete-based material is a key parameter for the assessment of its stability and durability, since a change in pH is usually associated with major types of chemical degradation such as carbonation, leaching and acid attacks. Conventional surface pH measurements with potentiometric flat surface electrodes have low spatial resolution, whereas optical pH visualization with indicator dyes (phenolphthalein) only indicates the areas with higher or lower pH than the pKa of the indicator. In this regard, it is key to develop wide-range imaging systems, enabling accurate and spatially resolved determination of pH variability for an advanced knowledge of degradation mechanisms. This contribution presents the enhancements made for a high-resolution optical pH imaging system based on fluorescent aza-BODIPY indicator dyes. The measurement range was increased to 6 pH units (pH 6.5 to pH 12.5) by a combination of two indicator dyes. Moreover, background scattering effects were sufficiently eliminated. With the improved sensor foils steep pH gradients (up to 3 pH units within 2 mm) were successfully recorded in various concrete specimens using a macro lens reaching a resolution of down to 35 µm per pixel.

5.3. Introduction

To determine the state of repair and durability of concrete structures, the development of pH over time and space is a key parameter. Chemical degradation mechanisms, such as carbonation, leaching reactions and acid attack, e.g. triggered by concrete - environmental interactions (e.g. aggressive solutions or gases), are directly associated with decreasing pH in the internal pore solutions and the external fluids [1–4]. In this perspective, detailed knowledge of pH distribution and associated pH gradients is crucial to gain a holistic process understanding of the different corrosion mechanisms and kinetics, to advance towards the development of sustainable concrete-based infrastructure. The pH of fresh Portland cement-based concrete is usually around 13 [5] and mainly controlled by the content of alkali-metals, portlandite, curing conditions and the addition of supplementary cementitious materials (SCMs) [6,7]. Behnood et al (2015) subcategorized state-of-the-art pH assessments for hardened concrete in destructive methods, such as expression of interstitial concrete pore fluids and leaching methodologies, and non-destructive methods, including embedded sensors like potentiometric electrodes and fiber optic sensors [8]. All these methods lack a sufficiently high spatial resolution to fully capture alteration processes [9–14]. Since concrete is a heterogeneous and porous material with various different components, pH changes usually proceed non-linear [5]. Thereby, the diffusion rates of aggressive fluids and gases are controlled by mineralogical heterogeneities in the microstructure of the concrete and variations in porosity, directly corresponding to pH alterations [15,16]. Accordingly, proper imaging techniques, which can resolve the spatial distribution of pH, are required for the characterization of these non-linear pH changes.

So far, mainly absorption-based indicator dyes, like phenolphthalein (PHPHT), are used to tackle this problem. This concept relies on the change of absorption properties, leading to a change in color depending on the pH. Therefore, classification in areas with higher or lower pH compared to the indicators pKa value (pH 9.7 in the case of PHPHT) is possible [17]. Their use is quite common, because pH indicator dyes are easy to use, cost efficient and provide quick analytical output. However, detailed information on the apparent pH value is not accessible and these unreferenced systems are prone to errors. Moreover, PHPHT is known for its carcinogenic effects and its widespread use should be avoided [18]. The first imaging technique of pH distribution on strongly alkaline concrete surfaces was introduced by Liu et al. (2017) based on a porphyrinoid dye (TFPLPt) covering a pH range from 11.0 to 13.5 [19]. Therein, dissolved TFPLPt molecules were coated on fractured mortar samples and images were recorded using a digital single lens camera, a white excitation light source and optical filters. The diagnostic bands were characterized in solution (artificial pore solution + TFPLPT and PHPHT) at various pH levels via transmittance spectroscopy prior to the measurement. Understanding the potential of optical pH imaging on cementitious materials, we were able to report on a pH imaging system based on time-domain dual lifetime referencing (t-DLR) [20] utilizing aza-BODIPYs as fluorescent pH indicator dyes [21]. This methodology used a SensiCam from PCO (https://www.pco.de/) for read-out, a red excitation source and an inert, phosphorescent, reference pigment (Egyptian Blue). It resolved the surface pH

of concrete samples between pH 9.35 to 12.35 with lifetime-based, ratiometric images. These results clearly demonstrated the potential of the t-DLR based imaging methodology to obtain high-resolution spatial pH distribution information. Nevertheless, challenges such as imperfect background compensation under low pH conditions or the limited pH range of three units, remained for further development.

Accordingly, this work presents further advances of this high-resolution imaging system. By combining two pH indicator dyes, an extension of the pH range from pH 6.5 to 12.5 was attained. Further, an alternative referencing pigment, Cr-GAB, was used which also acts as an optical barrier, minimizing background influences. To show the versatility of the methodology, different types of concrete samples, exposed to (i) carbonation), (ii) biogenic acid corrosion and (iii) leaching due to soft water were analyzed. Moreover, close-up images of pH gradients were taken using a macro lens, thus increasing the resolution up to 35 µm per pixel.

5.4. Methods

5.4.1. Measurment set-up

The used set-up has been recently described by Grengg & Müller et al. [21]. In brief, a sensor foil is soaked in 150 mM NaCl solution and placed on a planar concrete surface (figure 1). By taking two consecutive pictures with the SensiCam from PCO through a RG9 long pass filter, the pH value of the surface is determined via t-DLR [20]. For t-DLR the first picture is taken during illumination, where the indicator (fluorescence) and the reference pigment (phosphorescence) contribute to the signal. It is divided by the second one, which is taken right after illumination, where only the reference pigment shows emission, due to is long phosphoresce lifetime (figure A1, supporting info). For the measurements described in this work, adjustments in regards of the excitation source were made. Two high-power LED arrays LR CP7P from OSRAM Opto Semiconductors GmbH, with a mean emission wavelength of 635 nm, were used as an excitation source to improve excitation light homogeneity. They were serially connected and operated at 60 V constant current. The optimized camera settings used for the measurements can be found in table A1 in the supporting info.

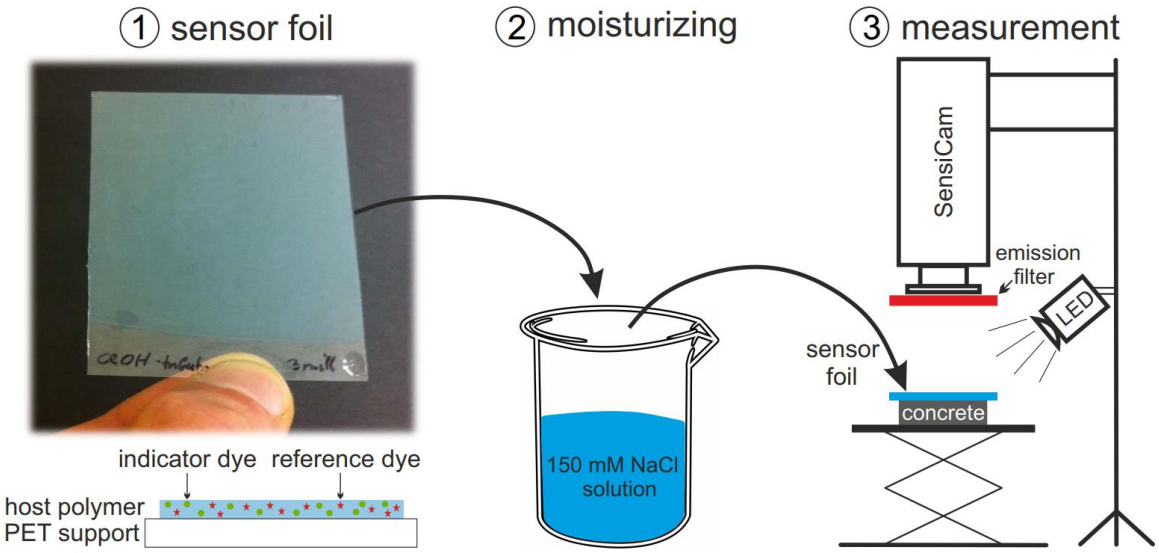

Figure. 1: Overview set-up; (1) Sensor foil based on hydrogel D4 comprising the indicator and reference dye; (2) Conditioning in 150 mM NaCl solution; (3) Lifetime-based ratiometric imaging of concrete samples with SensiCam and red excitation light [21].

5.4.2. Sensor material

Aza-BODIPYs are a class of pH indicator dyes, which are well known for their excellent chemical and photochemical stability, their bright near infrared emission and the wide range of available pKa values, which determine the most sensitive point of an optical pH-sensor [22]. A single indicator dye provides thereby an analytically useful range of 3 pH-units [23]. Staudinger et al. recently reported on a set of aza-BODIPY dyes with similar spectral properties and rather high apparent pKa values, featuring a pure PET effect [24]. Due to the similar absorption spectra a wide-range pH sensor is realized by mixing two indicators with different apparent pKa values. Chromium(III)-activated gadolinium borate (Cr-GAB) in the form of microcrystalline powder was used as reference material [25]. This inorganic phosphor exhibits similar spectral properties compared to the used pH indicator dyes and shows excellent chemical and photochemical stability. Moreover, its phosphorescence displays no cross sensitivity to oxygen, since it's a bulk material. The spectral properties of the used materials are shown in figure 2. As host polymer a polyurethane based hydrogel (HydroMed D4 from Advanced Biomaterials) is used. 100 mg are dissolved in 900 mg of a mixture of ethanol/water (9+1), 0.08% wt. of the dye with the lower pKa value (m-OH diCl azaBODIPY, pKa= 7.53) and 0.12% wt. of the dye with the higher pKa value (m-OH diF azaBODIPY, pKa= 10.29 or m-OH Cl azaBODIPY, pKa= 10.77) are added with respect to the polymer. For referencing, two times the amount of the polymer (200% wt.) of Cr-GAB was added as a fine powder (particle size ~5 µm) and suspended in the polymer solution. The resulting sensor formulation was knife-coated on a 125 µm thick PET foil from DuPont Teijin Films (Melinex 506) using a 3 mil (76 µm) wet film knife from Byke. The resulting sensor film has an approximate thickness of 19 µm after evaporation of the volatile compounds. Due to a water uptake of 50% of the hydrogel, the sensor

film has an estimated thickness of 25 µm in the wet state. The foils were cut into 5x5 cm squares to fit the samples and stored in 150 mM NaCl aqueous solution.

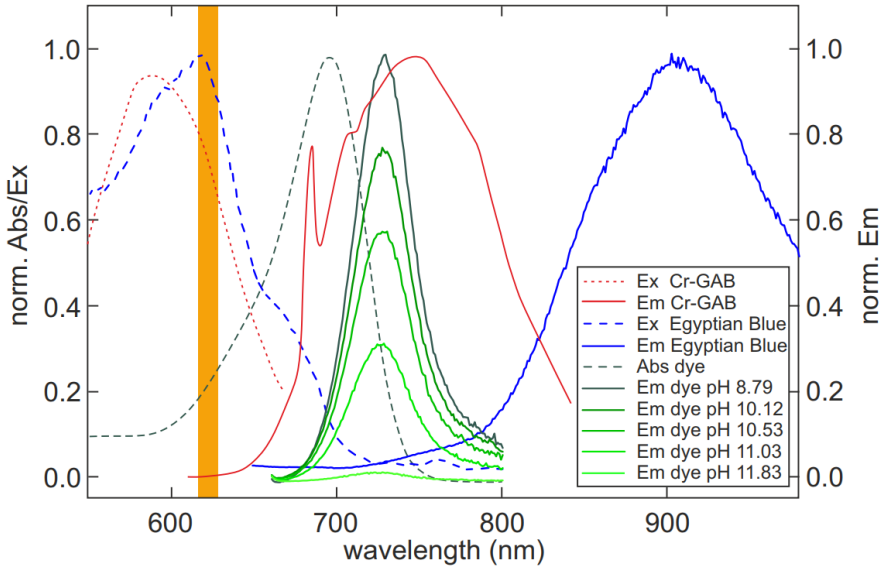

Figure 2: Absorption (Abs), excitation (Ex) and emission (Em) spectra of pH indicator dye (m-OH Cl azaBODIPY, pKa= 10.77) and reference materials. The emission of Cr-GAB matches the fluorescence of the indicator dye better than the emission of previously used Egyptian Blue. The orange bar indicates the wavelengths of the excitation source (635 nm) used for the imaging system.

5.4.3. Calibration, background evaluation & measurements

Calibration was done using solutions of 10 mM of an appropriate buffer substance (acetic acid, MES, phosphate, TRIS, CHES, and CAPS; see table A2 in the supporting info) and 150 mM NaCl. The solutions were adjusted to appropriate pH with 3 M NaOH or HCl using a potentiometric pH electrode from Mettler Toledo (InLab® Routine Pro). For each calibration point the sensor foil was soaked in buffer, placed under the camera on a black background within the focus of the lens, and pictures were taken. Data processing is done as described by Grengg & Müller et al. [21]. The mean ratiometric value of each picture is plotted against the appropriate pH value and the resulting curve is fitted using the Boltzmann equation (equation 1) to gain the calibration function:

$$R = B + \left(\frac{A - B}{1 + 10^{\frac{pH - V_{50}}{slope}}} \right) \qquad \textbf{Equation 1}$$

Where R represents the ratio, A the top value, B the bottom value, pH the pH value, V50 the point of inflection and slope the slope in the point of inflection of the Boltzmann function.

For the evaluation of the influence of the background the sensor foil was again soaked in defined buffer, as described above. However, instead of placing the foil on a black background, it was put

on a wet piece of concrete, which was wrapped in cellophane. Pictures were taken and the resulting ratio values converted to pH values using the according calibration.

Measurements on concert samples were performed by placing the calibrated sensor foil, preconditioned in 150 mM NaCl solution, on planar samples. Pictures were taken after one minute and the resulting ratio values converted to pH with the according calibration function.

5.4.4. Concrete sample

For the surface pH measurements three different concrete types were used which had been exposed to corrosive environments either in lab or in the field. Images of theses concrete specimens were recorded using a Keyence VHX-5000 Digital-Microscope.

Sprayed Concrete (SpC)

The first concrete type was a wet-mix shotcrete that was produced during real scale trials within the ASSpC research project (Advanced and Sustainable Sprayed Concrete research project; FFG project-No. 856080). The cement was a CEMII/B-M(S,L,Q) 52.5 N and the w/c ratio was 0.48. 6% of an alkali free accelerator and dolomite aggregates from 0-8 mm were used. The 28 day compressive strength was ~56 MPa. At 69 days of age, a 70 mm drill core was extracted from a larger specimen and stored for 7 days at 65% r.h. and 20 °C.

Consequently, the drill core was treated in a CO2 climatic chamber at 65% r.h., 20 °C and a CO2 concentration of 2% for 28 days. Thereafter, fresh cross-section areas were produced by cutting the specimens with an angle grinder. In order to prevent further surface pH alterations, samples were stored in a desiccator under nitrogen atmosphere.

Ultra High-Performance Fiber-Reinforced Concrete (UHPFRC)

The second concrete type was an Ultra High-Performance Fiber-Reinforced Concrete (UHPFRC) with a water/binder ratio of 0.2 and a compressive strength of ~190 MPa. The UHPFRC contained micro-steel fibers and the maximum grain size for the quartz sand used was <1 mm. From a larger specimen a 4x4x8 cm^3 prim was cut before placing it for 12 months in a sewer system, strongly affected by biogenic acid corrosion. A detailed characterization of the exposure system is given elsewhere [26,27]. In brief, prevailing environmental conditions comprised r.h. levels of between 80 and 100% and high concentrations of hydrogen sulfide (H^2S) (average of 34 ppm; peak levels of 350 ppm) and CO2 (1000 to 6200 ppm). After sample collection, concrete specimens were dried at 40 °C for 24 h. Thereafter, the sample was stabilized with a two component epoxy resin and fresh cross-section areas were produced by cutting the specimens with an angle grinder. In order to prevent further surface pH alterations, samples were stored in a desiccator under nitrogen atmosphere until measurement.

Precast Concrete (PCC)

The third concrete type was a precast concrete (tubings) that was installed 10 years ago in a headrace tunnel of a hydropower plant. Little information is available about the composition and

mechanical parameters except for the aggregates used, which were limestone and dolostone fragments made of calcite and dolomite, respectively. In the headrace tunnel, the concrete showed clear signs of soft-water-attack as most of the aggregates have been entirely leached away. The process water had an EC < 100 µS cm^{-1} with very low Ca^{2+} (~ 12 mg L^{-1}) and Mg^{2+} (~ 1 mg L^{-1}) concentrations. The extracted 50 mm drill cores were stabilized using a two-component epoxy resin. Fresh cross-section areas were produced by cutting the specimens with an angle grinder. In order to prevent further surface pH alterations, samples were stored in a desiccator under nitrogen atmosphere until measurement.

5.5. Results & Discussion

5.5.1. Improvement of the imaging method

In this study, we improved our pH-imaging technique by extending pH measurement range to up to 6 pH units (6.5 – 12.5). During laboratory work two foils have been manufactured. The first foil contains a combination of m-OH diCl azaBODIPY (pKa= 7.53) and m-OH diF azaBODIPY (pKa= 10.29). Accordingly, the gap between the pKa values was 2.79 pH units. Therefore, a nice overlap between the sensitivity ranges of the dyes is guaranteed, resulting in a good fit using the Boltzmann equation (figure 3). For the multi-dye approach to work predictably, it is important that the absorption spectra of the dyes do not change with the pH (dyes based solely on photoinduced electron transfer) in order to guarantee constant phosphorescence from the reference dye [24]. However, due to the deactivation of protonated dye molecules by deprotonated dye molecules via a Förster Resonance energy transfer (FRET) effect, a 50% higher ratio of the indicator with higher pKa value was used to guarantee equally strong fluorescence signals of both components and to have a symmetrical calibration function. This foil was finally used for the sample measurements. The close-up images were done with the same foil, resulting in a slightly different calibration function due to the use of a macro lens (figure A2, supporting info).

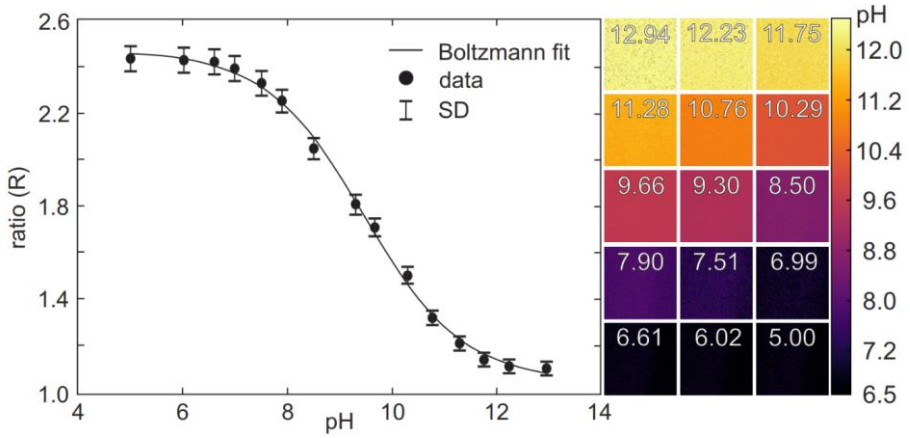

Figure 3: Left: Calibration function of the sensor foil combining the indicators m-OH diCl azaBODIPY (pKa= 7.53) and m-OH diF azaBODIPY (pKa= 10.29), which was used for sample measurements. The point of inflection (V50) is at pH 9.47 with a sensitivity (slope) of 2.16 pH units per R. The top value (A) is 2.47 and the bottom (B) value 1.05. Right: False color images of pH in calibration buffers.

The second foil contained a combination of m-OH diCl azaBODIPY (pKa= 7.53) and m-OH Cl azaBODIPY (pKa= 10.77), which have a gap between the apparent pKa values of 3.24 pH units. As previously described, a single pH dye has a sensitive range of ±1.5 pH units around their pKa value, this results in a gap of about 0.25 pH units, in which this foil has theoretically a lower sensitivity. However, a fit with the Boltzmann equation still provides an acceptable calibration (figure A3, supporting info) although the two separate sigmoidal curves may be adumbrated. The marginally lower quality of the fit outweighs the slightly wider calibration range and no measurements were done with this foil. It was used for the evaluation of the background.

Another improvement of the method is the application of an alternative reference material. Cr GAB was used, since it shows a better spectral overlap with the pH sensitive dyes (figure 2), compared to the previously used Egyptian Blue [21]. As Cr-GAB inhibits a lower brightness than Egyptian Blue, four times the amount was used. However, this turned out to be beneficial, since the resulting sensor foil was more opaque, ensuring higher robustness from the variation in background scattering and auto-fluorescence. Moreover, due to the better spectral overlap, the emitted light from the indicator and the reference have almost the same wavelength. Therefore, referencing barely suffers from reflection and absorption behavior of the background, which is wavelength dependent. The stability of the referencing system is evaluated in figure 4, where the influence of the background at different pH values is investigated. Barely any artefacts are visible. Only at low pH values, mild reflections on bright surfaces are visible.

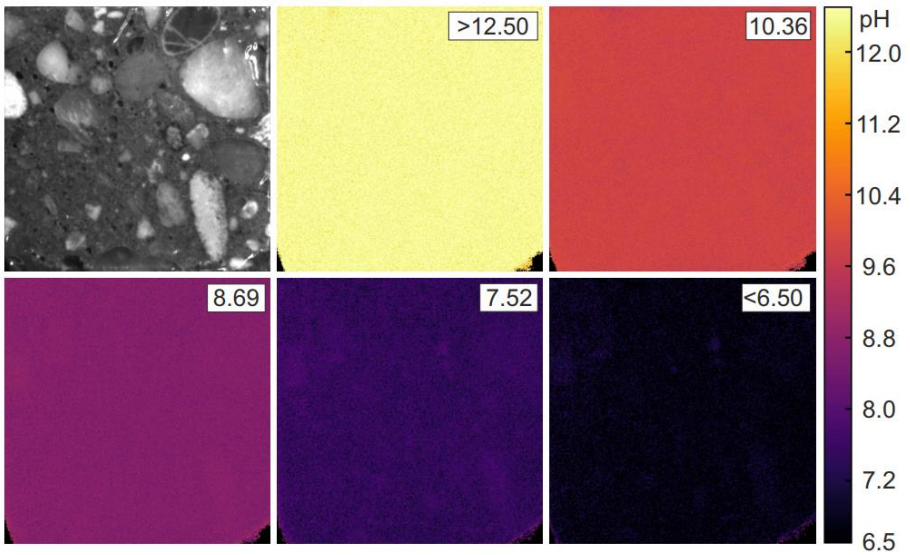

Figure 4: Artefacts at different pH values due to reflection and scattering from aggregates form the background. Only minor inhomogeneities at low pH levels are visible.

5.5.2. Measurements of different concrete samples

The change in pH of different types of concrete materials exposed to various chemical attacks has been analyzed using the pH imaging methodology described. Cross sections of UHPFRC, exposed for 12 months to biogenic acid attack, showed a strong decrease in pH of more than 6 pH units (figure 5). The intact cementitious matrix in the core region of the sample is still dominated by strongly alkaline pH conditions above pH 12, while a strong decrease, in two steps, down to a pH below the detectable level of 6.5 is visible at the surface, close to the corrosion layer (see also pH profile figure A4, supporting info). This drop in pH is accompanied by complete destruction of the cementitious microstructure, precipitation of sulfate salts and associated loss in textural stability, frequently observed by concretes exposed to biogenic acid attack [28].

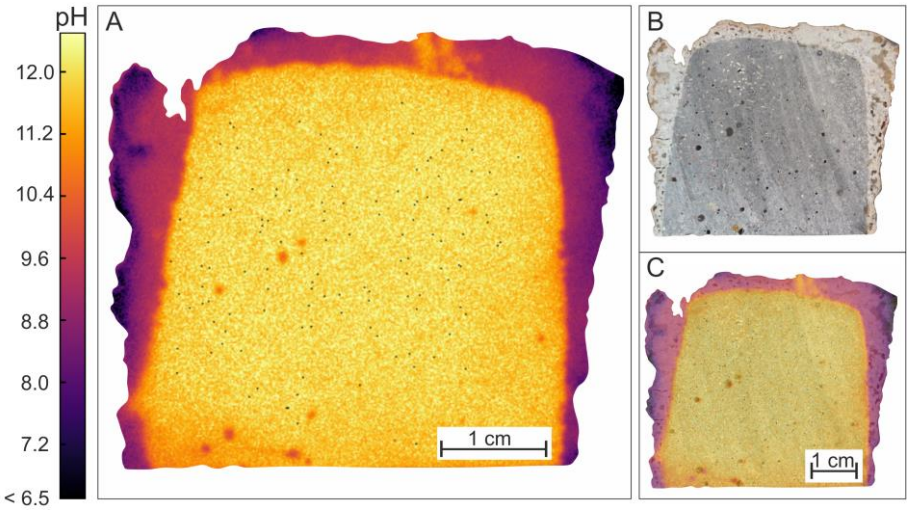

Figure 5: Cross-section of a UHPFRC sample after 12 months of exposure to biogenic acid attack. A) False color pH image of the sample. B) Sample image of the concrete block. C) Overlay of the pH image and sample image.

On the contrary, the SpC sample pre-exposed to accelerated carbonation shows a lower pH gradient, from around pH 12 down to pH 8.5. This perfectly corresponds to the well-described pH alterations frequently observed during carbonation (figure 6) [15]. A similar pH gradient is observed on the cross-section of the PCC, pre-exposed to soft waters (figure 7).

The successful use of the developed pH imaging technique on various concrete samples, exhibiting strongly varying chemical and physical properties as well as pre exposure to different alteration mechanisms, clearly demonstrates the functionality and robustness of this novel technology.

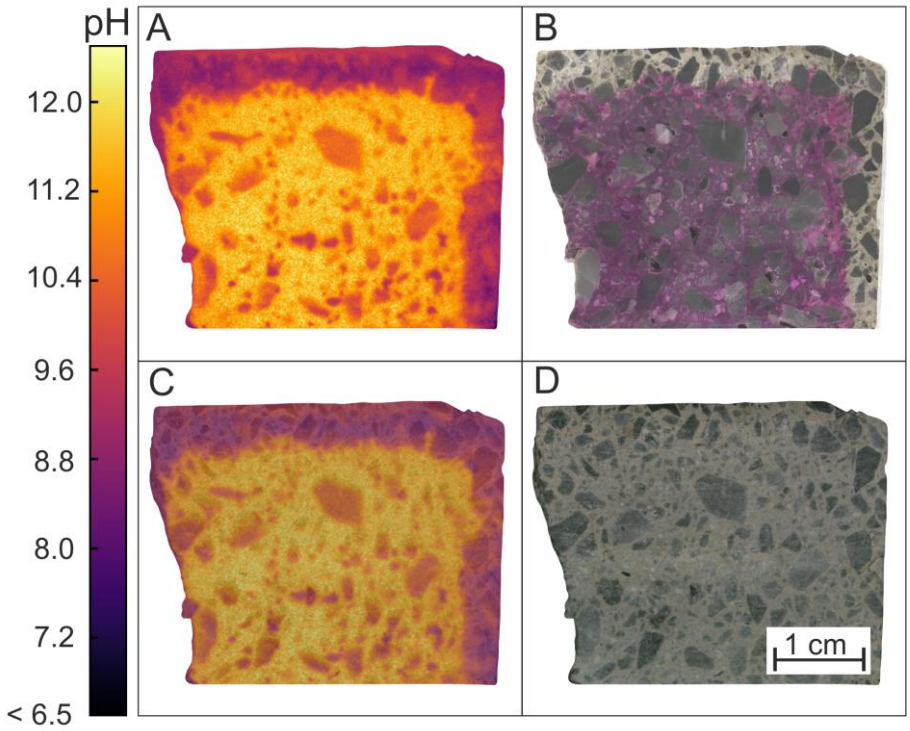

Figure 6: Cross-section of a wet-mix shotcrete with dolomite aggregates treated in a 2% CO^2 atmosphere for 28 days. A) False color pH image of the sample. B) Microscope image of the same shotcrete sample after short grinding with a 40 µm diamond-grinding wheel and spraying with phenolphthalein C) Overlay of the pH image and sample image. D) Microscope image of the shotcrete specimen.

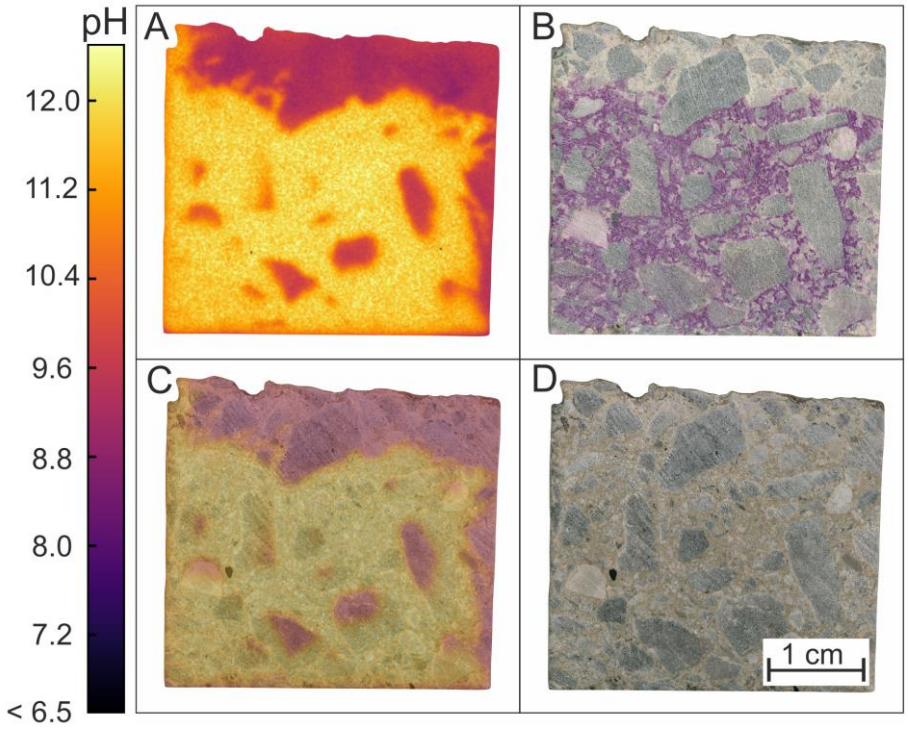

Figure 7: Cross-section of a sample taken from a precast concrete element that was exposed to soft-water for 10 years. The aggregates are dolomite and calcite. A) False color pH image of the sample. B) Microscope image of the same sample after short grinding with a 40 µm diamond-grinding wheel and spraying with phenolphthalein C) Overlay of pH image and sample image. D) Microscope image of the specimen.

5.5.3. Close-up images & repeatability

To gain a better resolution of the observed pH gradients, close-up pH images using a macro lens were obtained. The recorded images cover an area of 2.19x1.64 cm and were taken on the same specimen surfaces as the pH measurements described above. Thereby, close-up images (figure 8) were processed showing a significantly higher resolution of around 35 µm per pixel. Additionally, the actual pH image stayed basically the same, even due to the fact that the measurement was done with two different lenses with two different calibration curves on two different days. This emphasizes the reproducibility of this imaging system.

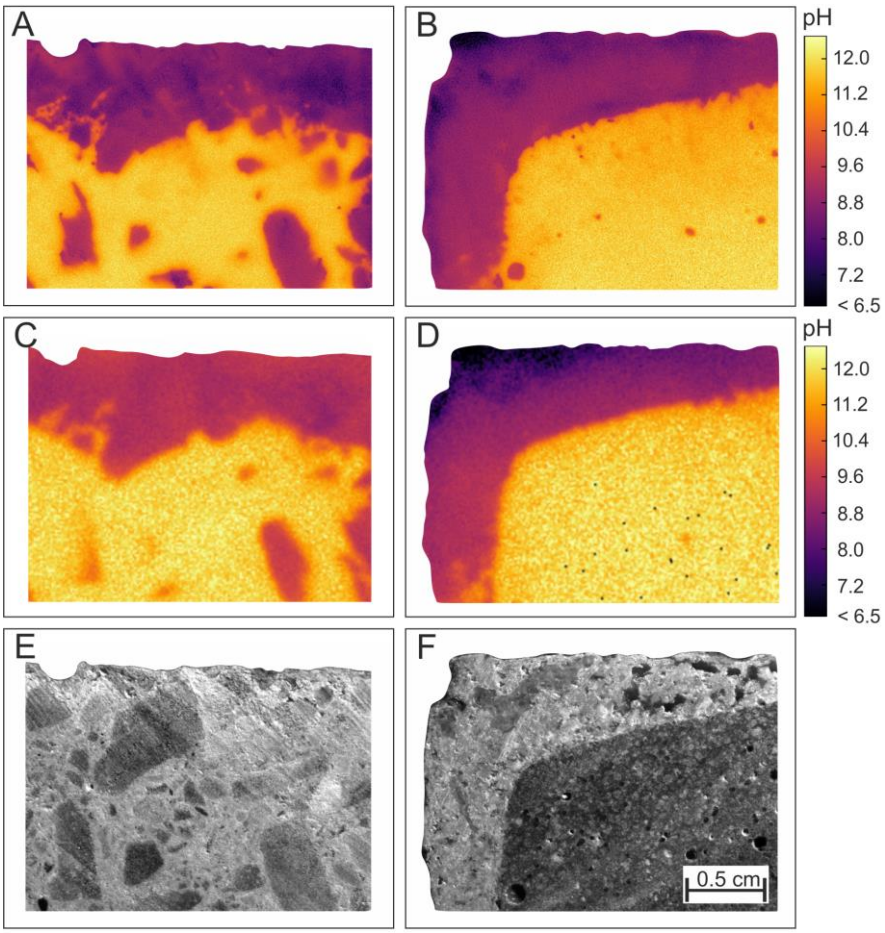

Figure 8: Comparison of close-up false color images (A, B) with the same area of the false color pH image done with the standard lens (C, D). Picture E & F show the PCC sample (E) and UHPFRC (F) were the pH images were recorded.

5.6. Conclusion & Outlook

In this study we improved the usability of t-DLR, based on versatile, pH sensitive aza-BODIBY dyes, as imaging system for concrete-based materials. An extended pH range from pH 6.5 to pH 12.5 was achieved by mixing two indicator dyes, enabling the examination of different corrosion scenarios and the surface pH of three different types of concrete was successfully imaged. For example, it was possible to follow the strong decrease in pH of more than 6 units on UHPFRC, which was strongly affected by biogenic acid attack corrosion. Thereby a very steep gradient of up to 1.5 pH units per mm was observed. Close-up images of these zones were taken with a macro lens leading to a resolution of up to 35 µm per pixel, which no other technique so far is able to achieve. These close-up images also show the reproducibility of the used imaging method, since they were taken with a different objective and therefore new calibration and still show an almost identical pH distribution.

For the future, a similar system based on polymer particles would be desirable, since it would open the possibility to measure on rough surfaces. Additionally, the exploration of wavelength-based referencing methods would be interesting, in order to open up the possibility to used standard camera equipment.

Overall, t-DLR based pH imaging has proven to be a highly promising tool for an advanced understanding of various chemical degradation mechanisms e.g. in the above heterogenic and porous concrete materials. Deciphering the reaction mechanisms and kinetics for alteration features is essentially required to develop tailored sustainable concrete-based infrastructure.

Acknowledgments

Bernhard Freytag, Walter Pichler and the ASSpC team (Advanced and Sustainable Sprayed Concrete research project; FFG project-No. 856080) are acknowledged for providing the concrete samples. We thank Isabel Galan and Joachim Juhart, Helmar Wiltsche and Lukas Troi for fruitful discussions.

5.7. References

[1] M. Stefanoni, U. Angst, B. Elsener, Corrosion rate of carbon steel in carbonated concrete – A critical review, Cement and Concrete Research. 103 (2018) 35–48. doi:10.1016/j.cemconres.2017.10.007.

[2] M. Rosenqvist, A. Bertron, K. Fridh, M. Hassanzadeh, Concrete alteration due to 55years of exposure to river water: Chemical and mineralogical characterisation, Cement and Concrete Research. 92 (2017) 110–120. doi:10.1016/j.cemconres.2016.11.012.

[3] A. Bertron, J. Duchesne, G. Escadeillas, Degradation of cement pastes by organic acids, Mater Struct. 40 (2007) 341–354. doi:10.1617/s11527-006-9110-3.

[4] A. Bertron, M.P. Lavigne, C. Patapy, B. Erable, Biodeterioration of concrete in agricultural, agro-food and biogas plants: state of the art and challenges, RILEM Technical Letters. 2 (2017) 83–89. doi:10.21809/rilemtechlett.2017.42.

[5] M. Alexander, A. Bertron, N. De Belie, eds., Performance of Cement-Based Materials in Aggressive Aqueous Environments, Springer Netherlands, Dordrecht, 2013. doi:10.1007/978-94-007-5413-3.

[6] G. Plusquellec, M.R. Geiker, J. Lindgård, J. Duchesne, B. Fournier, K. De Weerdt, Determination of the pH and the free alkali metal content in the pore solution of concrete: Review and experimental comparison, Cement and Concrete Research. 96 (2017) 13–26. doi:10.1016/j.cemconres.2017.03.002.

[7] Q. Pu, L. Jiang, J. Xu, H. Chu, Y. Xu, Y. Zhang, Evolution of pH and chemical composition of pore solution in carbonated concrete, Construction and Building Materials. 1 (2012) 519–524. doi:10.1016/j.conbuildmat.2011.09.006.

[8] A. Behnood, K. Van Tittelboom, N. De Belie, Methods for measuring pH in concrete: a review, Construction and Building Materials. 105 (2016) 176–188. doi:http://dx.doi.org/10.1016/j.conbuildmat.2015.12.032.

[9] K. Pásztor, A. Sekiguchi, N. Shimo, N. Kitamura, H. Masuhara, Iridium oxide-based microelectrochemical transistors for pH sensing, Sensors and Actuators B: Chemical. 12 (1993) 225–230. doi:10.1016/0925-4005(93)80023-5.

[10] Y.S. Femenias, U. Angst, B. Elsener, PH-monitoring in mortar with thermally-oxidized iridium electrodes, RILEM Technical Letters. 2 (2017) 59–66. doi:10.21809/rilemtechlett.2017.37.

[11] Y.S. Femenias, U. Angst, B. Elsener, Monitoring pH in corrosion engineering by means of thermally produced iridium oxide electrodes, Materials and Corrosion. 69 (2018) 76–88. doi:10.1002/maco.201709715.

[12] Y.S. Femenias, U. Angst, F. Moro, B. Elsener, Development of a Novel Methodology to Assess the Corrosion Threshold in Concrete Based on Simultaneous Monitoring of pH and Free Chloride Concentration, Sensors (Basel). 18 (2018). doi:10.3390/s18093101.

[13] A. Safavi, M. Bagheri, Novel optical pH sensor for high and low pH values, Sensors and Actuators B: Chemical. 90 (2003) 143–150. doi:10.1016/S0925-4005(03)00039-X.

[14] O.S. Wolfbeis, Fiber-Optic Chemical Sensors and Biosensors, Anal. Chem. 76 (2004) 3269–3284. doi:10.1021/ac040049d.

[15] J. Stark, B. Wicht, Dauerhaftigkeit von Beton, Springer Berlin Heidelberg, Berlin, Heidelberg, 2013. doi:10.1007/978-3-642-35278-2.

[16] C.L. Page, M.M. Page, eds., Durability of concrete and cement composites, CRC Press, Boca Raton, Fla., 2007.

[17] L.J. Parrott, Cement and Concrete Association, Building Research Establishment, A review of carbonation in reinforced concrete., Cement and Concrete Association, 1987.

[18] J.K. Dunnick', J.R. Hailey, Phenolphthalein Exposure Causes Multiple Carcinogenic Effects in Experimental Model Systems, Cancer Research. 56 (1996) 4922–4926.

[19] E. Liu, M. Ghandehari, C. Brückner, G. Khalil, J. Worlinsky, W. Jin, A. Sidelev, M.A. Hyland, Mapping high pH levels in hydrated calcium silicates, Cem Concr Res. 95 (2017) 232–239. doi:10.1016/j.cemconres.2017.02.001.

[20] C. R. Schröder, B. M. Weidgans, I. Klimant, pH Fluorosensors for use in marine systems, Analyst. 130 (2005) 907–916. doi:10.1039/B501306B.

[21] C. Grengg, B. Müller, C. Staudinger, F. Mittermayr, J. Breininger, B. Ungerböck, S.M. Borisov, T. Mayr, M. Dietzel, High-resolution optical pH imaging of concrete exposed to chemically corrosive environments, Cem Concr Res. (2018) (accepted).

[22] M. Strobl, T. Rappitsch, S.M. Borisov, T. Mayr, I. Klimant, NIR-emitting aza-BODIPY dyes – new building blocks for broad-range optical pH sensors, Analyst. 140 (2015) 7150–7153. doi:10.1039/C5AN01389E.

[23] T. Jokic, S.M. Borisov, R. Saf, D.A. Nielsen, M. Kühl, I. Klimant, Highly Photostable Near-Infrared Fluorescent pH Indicators and Sensors Based on BF2-Chelated Tetraarylazadipyrromethene Dyes, Analytical Chemistry. 84 (2012) 6723–6730. doi:10.1021/ac3011796.

[24] C. Staudinger, J. Breininger, I. Klimant, S.M. Borisov, Near-infrared aza-BODIPY dyes with fluorescence response solely due to photoinduced electron transfer: new pH indicators covering the neutral to highly alkaline range, Analyst. (2018) (submitted).

[25] S.M. Borisov, I. Klimant, A versatile approach for ratiometric time-resolved read-out of colorimetric chemosensors using broadband phosphors as secondary emitters, Analytica

Chimica Acta. 787 (2013) 219–225. doi:10.1016/j.aca.2013.05.032.

[26] C. Grengg, F. Mittermayr, A. Baldermann, M.E. Böttcher, A. Leis, G. Koraimann, P. Grunert, M. Dietzel, Microbiologically induced concrete corrosion: A case study from a combined sewer network, Cement and Concrete Research. C (2015) 16–25. doi:10.1016/j.cemconres.2015.06.011.

[27] C. Grengg, F. Mittermayr, G. Koraimann, F. Konrad, M. Szabó, A. Demeny, M. Dietzel, The decisive role of acidophilic bacteria in concrete sewer networks: A new model for fast progressing microbial concrete corrosion, Cem Concr Res. 101 (2017) 93–101. doi:10.1016/j.cemconres.2017.08.020.

[28] C. Grengg, F. Mittermayr, N. Ukrainczyk, G. Koraimann, S. Kienesberger, M. Dietzel, Advances in concrete materials for sewer systems affected by microbial induced concrete corrosion: A review, Water Res. 134 (2018) 341–352. doi:10.1016/j.watres.2018.01.043.

5.8. Supporting Information

Table A1: Camera settings for t-DLR pH imaging for the three different measurements.

	Evaluation background	Sample measurements	Close-up images
Lens	Pentax TV Lens 12 mm 1:1.2	Pentax TV Lens 12 mm 1:1.2	Schneider Xenoplan 1.4/23-0902
Aperture	16	8	5,6
Integration time	50 ms	90 ms	60 ms
Cycle time	62 µs	62 µs	62 µs
Excitation length	50 µs	50 µs	50 µs
Window length	10 µs	10 µs	10 µs
Delay window 1	40 µs	40 µs	40 µs
Delay window 2	51 µs	51 µs	51 µs

Table A2: Used buffer substances and their operational pH area

pH range	buffer substance
< 5.75	acetic acid (pKa = 4.76)
5.75 - 6.75	MES (pKa = 6.1)
6.75 - 7.75	phosphate (pKa = 7.21)
7.75 - 9.00	TRIS (pKa = 8.2)
9.00 - 10.00	CHES (pKa = 9.3)
10.00 - 11.50	CAPS (pKa = 10.4)
< 5.75	phosphate (pka= 12.32)

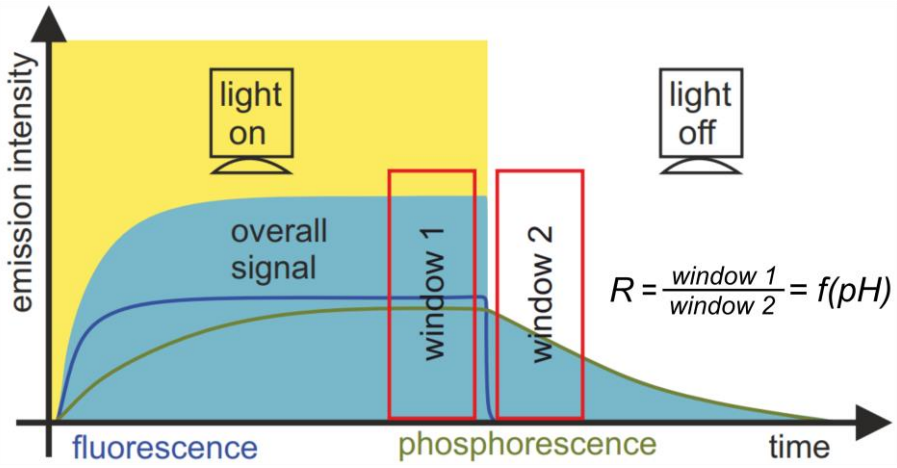

Figure. A1: Explanation time-domain dual lifetime referencing (t-DLR); The fluorescence emission of the pH indicator has a short lifetime and is only present in the first window during illumination, whereas the phosphorescence emission of the reference pigment contributes in both windows (modified after [21].)

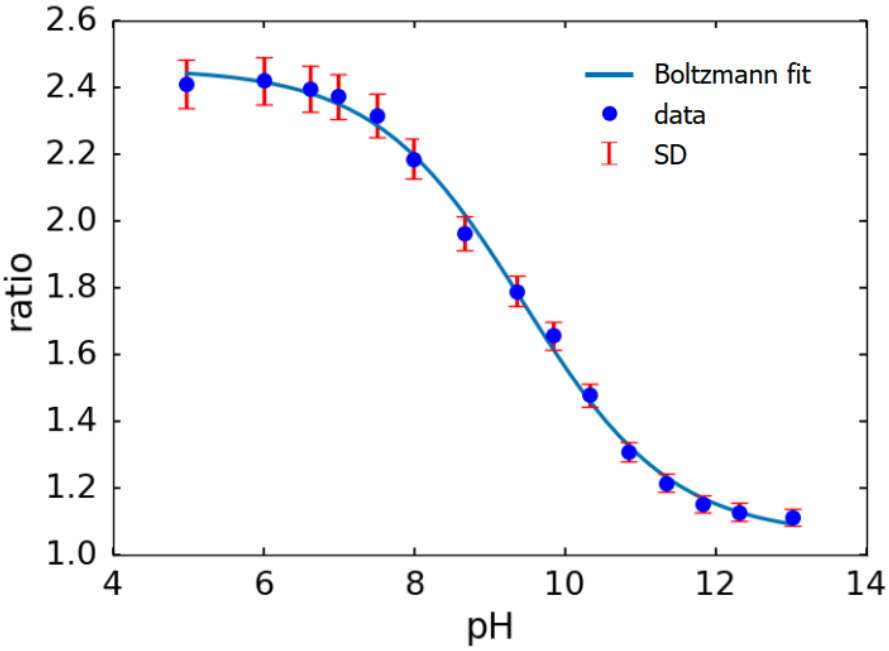

Figure A2: Calibration function, obtained with the macro lens, of the sensor foil combining the indicators m-OH diCl azaBODIPY (pKa= 7.53) and m-OH diF azaBODIPY (pKa= 10.29), which was used for sample measurements. The point of inflection (V50) is at pH 9.45 with a sensitivity (slope) of 2.26 pH units per R. The top value (A) is 2.46 and the bottom (B) value 1.06.

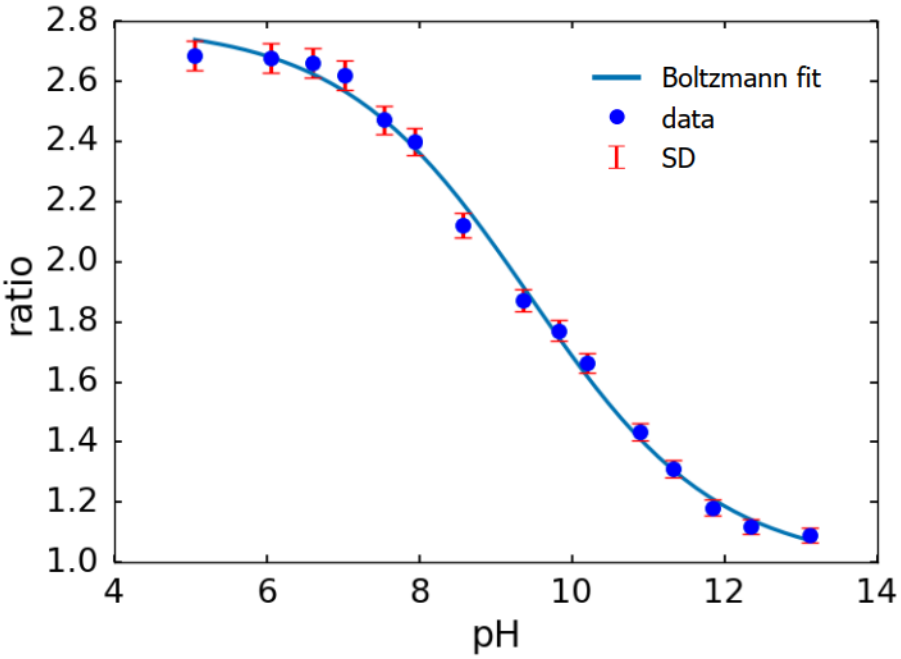

Figure A3: Calibration function, obtained with the standard lens, of the sensor foil combining the indicators m-OH diCl azaBODIPY (pKa= 7.53) and m-OH Cl azaBODIPY (pKa= 10.77), which was used for background evaluation. The point of inflection (V50) is at pH 9.44 with a sensitivity (slope) of 2.97 pH units per R. The top value (A) is 2.80 and the bottom (B) value 0.97.

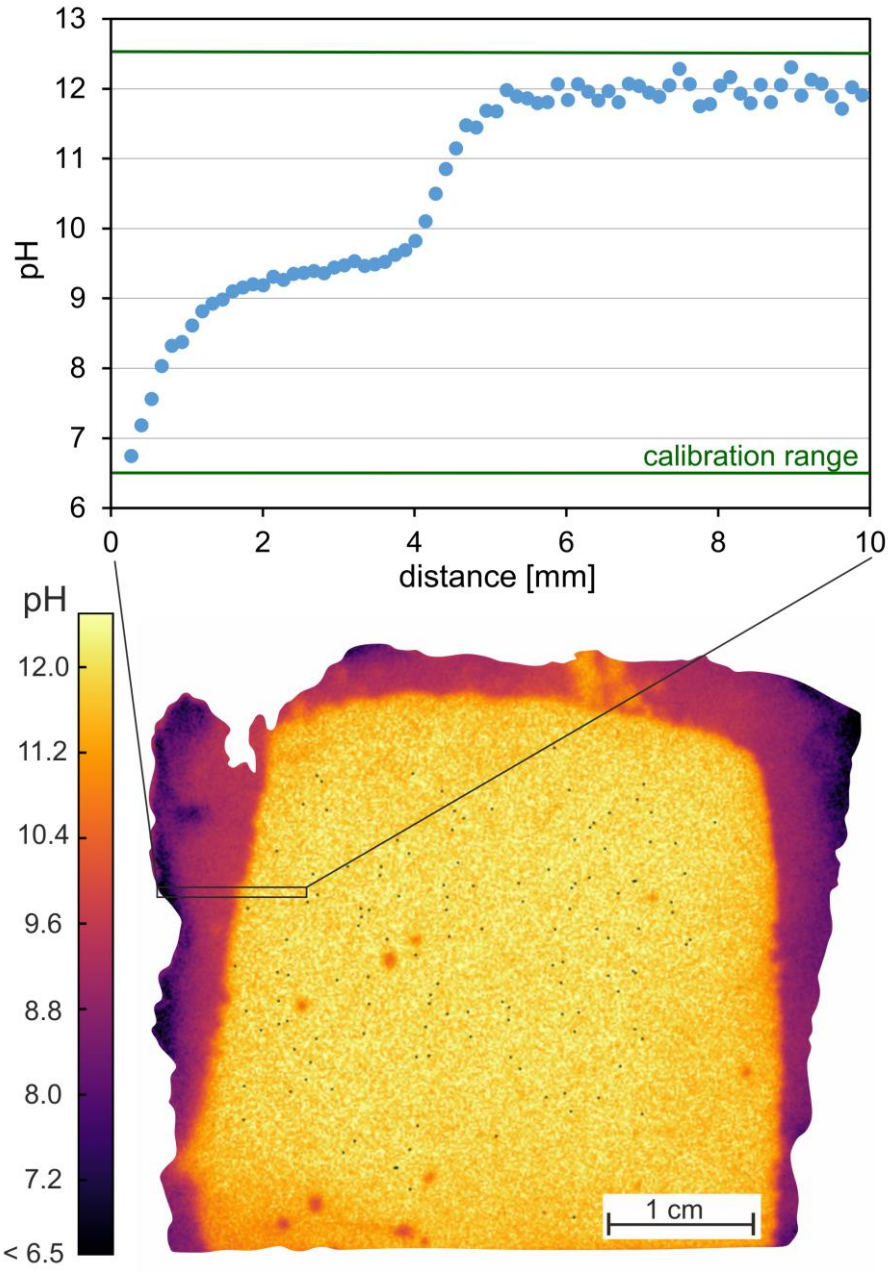

Figure A4: Cross-section of a UHPFRC sample after 12 months of exposure to biogenic acid attack. False color pH image of the sample with the pH gradient displayed for the first 10 mm.

Part IV

Future Prospects and Conclusions

6. Summary and conclusion

The purpose of the dissertation was to exploit the advantages of luminescent optical sensors with regards to their potential to be miniaturized and their capability to performed chemical imaging.

Within the first conducted project, oxygen and pH sensors with a spot size of less than 0.8 mm were successfully integrated into microfluidic chips. The used microfluidic chips for this project were produced via a novel prototyping approach based on injection molding machines for optical media. The resulting green bodies made from thermoplastic COC provided the structured parts of the chips, which were afterwards fully assembled in a post-processing step, including the integration of the sensor spots and closing of the chips utilizing adhesive tape. Sensor integration was done with a microdispensing unit which enables successful sensor integration onto structured surfaces and allows the fabrication of sensor formulations containing particles. This feature is needed to integrate pH sensor spots, which consist of a fluorescent pH indicator dye and inert phosphorescent reference particles, as well as oxygen sensor spots containing sensitive polymer particles. Sensor read out was done with miniaturized phasefluorimeters utilizing the luminescent decay time as stable measurement parameter. A chip holder was constructed in order to provide good alignment of the sensor spots with the optical fibers used for read -out. To show the viability of the new stop/flow measurement approach for monitoring of metabolic parameters of mammalian cells, A549 cells were incubated in the produced chips and several measurements of the acidification and respiration rate performed. The results showed good reproducibility and we were even able to monitor metabolic changes upon poisoning of the cells. This clearly shows the potential of this novel measurement approach which enables in-line monitoring of metabolic parameters in microfluidic devices while causing minimal disturbance for the cells. Moreover, this flexible approach can be easily transferred to other microfluidic systems giving the organ-on-chip community a new analytical method to work with.

The second project proved the suitability for luminescent imaging based on new fluorescent indicator dyes as a great measurement method for concrete research. It was shown that this new method is vastly superior to existing technologies due to its precise pH measurement with high resolution. The used measurement scheme utilizes a gate-able camera system and time-domain dual lifetime referencing as a reliable referencing technique to minimize the influence of the heterogenic background of concrete samples. This allowed for detailed monitoring of nonlinearly progressing chemical concrete degradation due to various kinds of attacks and on different concrete materials, since it is always strictly relating to the pH distribution. Therefore, a more detailed assessment of concrete durability and state-of-repair analysis is possible. In the future, exploration of particle based optical pH sensors might allow the method to be suitable for field application and therefore have an even higher impact on concrete analytics.

Part V

Appendix

7. Curriculum Vitae

Bernhard Müller, MSc.

Current Address	Stiftingtal 52/9, 8010 Graz, Austria
Permanent Address	Vogelsangweg 5, 4840 Vöcklabruck, Austria
Date of Birth	01 December 1987 in Graz
Nationality	Austria
E-Mail	berni.mueller@gmx.at

Education

02/2016 – 04/2020	**PhD student** in Technical Chemistry at Graz University of Technology, Topic: "*Application of Luminescent Sensors – A Journy from Miniaturization to Imaging", Supervisor: Assco.Prof. Torsten Mayr, Conducted* at the Institute of Analytical Chemistry and Food Chemistry
11/2012 – 05/2015	**Master program** Chemistry at Graz University of Technology and Karl-Franzens University Graz (NAWI Project) Thesis: "*Luminescent Nanosensor Particles for the Application in Microfluidic Systems", Supervisor: Assco.Prof. Torsten Mayr, Conducted* at the Institute of Analytical Chemistry and Food Chemistry
09/2011 - 05/2012	**Exchange Program**: Joint-Study; University of Calgary, Canada
10/2008 - 11/2012	**Bachelor program** Chemistry at Graz University of Technology and Karl-Franzens University Graz (NAWI Project)
09/2002 - 06/2007	**A-Level** at HTBLA Vöcklabruck; College for Mechanical Engineering Department for Environmental Technology

Additional Experience

20.July-27. July 2017	**Summer school**: Biochemical sensors in medicine, ASCOS, Třešť, Czech Republic
May 31 - June 9, 2016	**Summer school**: Microsensor Analysis in the Environmental Sciences, Marine Biological Station Rønbjerg, Denmark
06/2014 - 10/2014	Mettler Toledo; developer at R&D - Process Analytics

Awards

06/2018	Young Researcher Award at RILEM 253-MCI; Toulouse, France
03/2018	Best Poster Award at Europt(r)ode XIV - Conference on optical chemical sensors and biosensors; Naples, Italy
05/2017	Best Poster Award at ECI: Single-use Technologies II, Tomar, Portugal

Publications in Peer Reviewed Journals

Müller, B.; Sulzer, P.; Walch, M.; Zirath, H.; Buryska, T.; Rothbauer, M.; Ertl, P.; Mayr, T. Measurement of Respiration and Acidification Rates of Mammal Cells in non-PDMS-based Microfluidic Devices; 2020. (submitted)

Frey, L.; Vorländer, D.; Rasch, D.; Meinen, S.; **Müller, B**.; Mayr, T.; Dietzel, A.; Grosch, J.-H.; Krull, R. Defining Mass Transfer in a Capillary Wave Micro-Bioreactor; 2020. (submitted)

Prat, S.; Martínez-Martínez, V.; Alamo-Sanza, M.; **Müller, B.**; Mayr, T.; Nevares, I. Image of O2 Dynamics Released by Oak Wood Submerged in Model Wine with Nanoparticle Sensors. Sens. Actuators B Chem. 2019, 238, 337–345. https://doi.org/10.1016/j.snb.2018.12.131.

Frey, L.; Vorländer, D.; Rasch, D.; Ostsieker, H.; **Müller, B.**; Schulze, M.; Schenkendorf, R.; Mayr, T.; Grosch, J.-H.; Krull, R. Novel Electrodynamic Oscillation Technique Enables Enhanced Mass Transfer and Mixing for Cultivation in Micro-bioreactor. Biotechnol. Prog. 2019, 35. https://doi.org/10.1002/btpr.2827.

Grengg, C.*& **Müller, B.***; Staudinger, C.; Mittermayr, F.; Breininger, J.; Ungerböck, B.; Borisov, S. M.; Mayr, T.; Dietzel, M. High-Resolution Optical PH Imaging of Concrete Exposed to Chemically Corrosive Environments. Cem. Concr. Res. 2019, 116, 231–237. https://doi.org/10.1016/j.cemconres.2018.10.027.

Müller, B.; Grengg, C.; Schallert, V.; Sakoparnig, M.; Staudinger, C.; Breininger, J.; Mittermayr, F.; Ungerböck, B.; Borisov, S. M.; Dietzel, M.; et al. Wide-Range Optical PH Imaging of Cementitious Materials Exposed to Chemically Corrosive Environments. RILEM Tech. Lett. 2018, 3, 39–45. https://doi.org/10.21809/rilemtechlett.2018.72.

Staudinger, C.; Strobl, M.; Fischer, J.; Thar, R.; Mayr, T.; Aigner, D.; **Müller, B.**; Müller, B.; Lehner, P.; Mistlberger, G.; et al. A Versatile Optode System for Oxygen, Carbon Dioxide, and PH Measurements in Seawater with Integrated Battery and Logger. Limnol. Oceanogr. Methods 2018, 16. https://doi.org/10.1002/lom3.10260.

Zirath, H.; Rothbauer, M.; Spitz, S.; Bachmann, B.; Jordan, C.; **Müller, B**.; Ehgartner, J.; Priglinger, E.; Mühleder, S.; Redl, H.; et al. Every Breath You Take: Non-Invasive Real-Time Oxygen Biosensing in Two- and Three-Dimensional Microfluidic Cell Models. Front. Physiol. 2018, 9. https://doi.org/10.3389/fphys.2018.00815.

Oral presentations

Müller* B. & Grengg* C, Staudinger C., Mittermayr F., Breininger J., Ungerböck B., Borisov SM., Mayr T., & Dietzel M.; Optical pH Imaging of Concrete Exposed to Chemically Corosive Environments; RILEM 253-MCI; Toulouse, France (**2018**) – Young Researcher Award

Müller B., Zirath H., Buryska T, Sulzer P., Strobl M., Ungerböck B., Rothbauer M., Borisov S.M., Ertl P. and Mayr T.; Respiration- and Acidification Rates of Mammal Cells Cultures in Microfluidic Devices utilizing Optical Sensors; 1st EUROoC – European Organ on a Chip Conference, Stuttgart, Germany; **(2018)**

Müller B., Sulzer P., Strobl M., Zirath H., Rothbauer M., Ertl P. and Mayr T.; Monitoring of metabolic parameters of mammal cells cultures in microfluidic devices using integrated optical chemical sensors; DocDays 2017 NAWI Graz; Graz, Austria; **(2017)**

8. List of Figures

Chapter 2 – Theoretical Background

Chapter 3 - Measurement of Respiration and Acidification Rates of Mammal Cells in non-PDMS-based Microfluidic Devices

Chapter 4 - High-resolution optical pH imaging of concrete exposed to chemically corrosive environments

Chapter 5 - Wide-range optical pH imaging of cementitious materials exposed to chemically corrosive environments

9. List of Tables

Chapter 2 – Theoretical Background

Chapter 3 - Measurement of Respiration and Acidification Rates of Mammal Cells in non-PDMS-based Microfluidic Devices

Chapter 4 - High-resolution optical pH imaging of concrete exposed to chemically corrosive environments

Chapter 5 - Wide-range optical pH imaging of cementitious materials exposed to chemically corrosive environments